The Effectiveness of Particle Dampers under Centrifugal Loads

by

Daniel Nicolaas Johannes Els

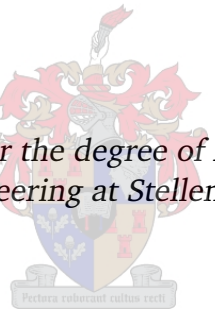

Dissertation approved for the degree of Doctor of Philosophy in Mechanical Engineering at Stellenbosch University

Department of Mechanical and Mechatronics Engineering,
University of Stellenbosch,
Private Bag X1, Matieland 7602, South Africa.

Promoter: Prof J.L. van Niekerk

March 2009

Declaration

By submitting this dissertation electronically, I declare that the entirety of the work contained therein is my own, original work, that I am the owner of the copyright thereof (unless to the extent explicitly otherwise stated) and that I have not previously in its entirety or in part submitted it for obtaining any qualification.

Signature: .....
D.N.J. Els

Date: 2009/02/19 .....

Abstract

The Effectiveness of Particle Dampers under Centrifugal Loads

D.N.J. ELS

Department of Mechanical and Mechatronics Engineering, University of Stellenbosch, Private Bag X1, Matieland 7602, South Africa.

Dissertation: PhD (Mech Eng)
March 2009

The main research objective of this dissertation was to determine the performance parameters of particle dampers (PDs) under centrifugal loads.

A test bench was developed consisting of a rotating cantilever beam with a PD at the tip. Equal mass containers with different depths, filled with a range of uniform sized steel ball bearings, were used as PDs. For all the tests, the total PD mass was identical. During operation the tip of the beam was displaced, and after release, the beam could vibrate freely. The decay in the vibratory motion of the tip of the beam was measured over a range of centrifugal loads.

The experiments were duplicated numerically with a discrete element method (DEM) model, calibrated against the experimental data. This model could then be used for a more in-depth investigation of phenomena occurring when PDs are under centrifugal loads.

From the data analysis, it can be concluded that there are two zones of damping, one with a high and one with a low damping factor. These damping zones depend on the ratio between the peak vibration acceleration and the centrifugal loading. Each zone has a limit in terms of the centrifugal loading beyond which the PD cannot function if the vibration amplitude is fixed. In the high damping zone, it was found that the excitation state of the particles was high enough for the system vibration frequency to change. In the low damping zone, there is only limited motion between the particles.

The main parameters that influence the performance of the PDs are the friction between the particles themselves and with the container, the PD length/diameter aspect ratio, and the particle size. An important finding is that a PD with less layers (increase in particle size) will still function at a higher centrifugal load compared to one with a smaller number number of layers.

Uittreksel

Die Effektiwiteit van Partikel Dempers onder Sentrifugale Laste

(The Effectiveness of Particle Dampers under Centrifugal Loads)

D.N.J. ELS

Departement Meganiese en Megatroniese Ingenieurswese, Universiteit van Stellenbosch, Privaatsak X1, Matieland 7602, Suid Afrika.

Proefskrif: PhD (Meg Ing)
Maart 2009

Die hoof navorsingsdoelwit vir hierdie proefskrif was die vasstelling van die werkverrigting van partikeldempers (PDs) onder sentrifugale belastings.

'n Toetsbank is ontwerp wat bestaan uit 'n roterende kantelbalk met 'n PD op die endpunt. Houers met dieselfde massa, maar met verskillende dieptes en gevul met staal koeëllaers is gebruik as PDs. Gedurende die bedryf van die stelsel is die punt van die balk verplaas en nadat dit losgelaat is, was dit vry om te vibreer. Die afname in verplasing van die punt van die balk is dan gemeet. Die proses is herhaal vir 'n reeks van rotasiesnelhede.

Die eksperimente is numeries gedupliseer met behulp van die diskrete element metode (DEM), waarvan die parameters gekalibreer is teen die eksperimentele data. Die numeriese modelle is dan verder gebruik om meer indiepte ondersoek in te stel na die verskynsels wat voorkom by PDs wat onder sentrifugale belastings funksioneer.

Vanaf die data-analises kan die afleiding gemaak word dat daar twee dempingsones is, een met 'n hoë dempingsfaktor en een met 'n lae dempingsfaktor. Hierdie dempingsones is afhanklik van die verhouding tussen die piek vibrasieversnelling en die sentrifugale belasting. Die werkverrigting van die PDs in die sones is beperk tot 'n grens in terme van die sentrifugale belasting. In die hoë dempingsone is bevind dat die opwekking van die partikels genoegsaam is om die stelsel se vibrasiefrekwensie te verander. In die lae dempingsone is daar slegs beperkte onderlinge beweging tussen die partikels.

Die belangrikste parameters wat die werkverrigting van die PDs beïnvloed, is die wrywing tussen die partikels onderling en tussen die partikels en die wande, die PD lengte/diameter aspekverhouding, en die partikelgrootte. 'n Belangrike bevinding was dat 'n PD met minder effektiewe partikel lae (groter partikels) steeds sal funksioneer by 'n hoër sentrifugale las in vergelyking met een met meer lae.

Acknowledgements

For helping me to complete this work and to produce this dissertation I would like to thank:

- Mr. Ockert Strydom for the many hours spent on the design and manufacturing of the test apparatus,
- The personnel of the Mechanical and Mechatronics workshop for their high quality of craftsmanship, and their assistance with the experimental work,
- Dr. Corné Coetzee for his help with the Discrete Element modelling and many fruitful discussions,
- Prof. Anton Basson, our departmental manager, for his support and for arranging as much research time as possible for me.

Dedications

Hierdie verhandeling word opgedra aan my wederhelfte Joëtte
vir al haar geloof, hoop en liefde.

Contents

Declaration i

Abstract ii

Uittreksel iii

Acknowledgements iv

Contents vi

List of Illustrations ix
Figures ix
Tables xi

Nomenclature and Abbreviations xii
List of symbols xii
Vector-tensor notation xii
Units and numbers xii
Acronyms xii

Chapter 1. Introduction 1
1.1 Background 1
1.2 Objectives and scope of research 6
1.3 Outline of the dissertation 7

Chapter 2. Literature Review 8
List of symbols for chapter 2 8
2.1 Parameters and definitions 9
2.2 Vibrated granular media 10
2.3 Particle damper characteristics 13
2.4 Data reduction and parameter extraction 15
2.5 Numerical modelling with the discrete element method 18
2.6 DEM simulations of particle dampers 22

Chapter 3. Experimental Setup and Calibration 23
List of symbols for chapter 3 23
3.1 Introduction 24
3.2 Measurement calibration 25
3.3 System characterization tests 27

Chapter 4. Experimental Analysis of Particle Dampers **33**
List of symbols for chapter 4 . . . 33
4.1 Introduction . . . 34
4.2 System parameters . . . 34
4.3 Test procedure . . . 36
4.4 General observations . . . 38
4.5 Data analysis . . . 38
4.6 Test results . . . 41

Chapter 5. DEM Analysis of Particle Dampers **43**
List of symbols for chapter 5 . . . 43
5.1 Introduction . . . 45
5.2 Container model . . . 45
5.3 Particle contact parameters . . . 47
5.4 DEM setup and simulations . . . 53
5.5 Simulation results . . . 56

Chapter 6. Data Analysis **58**
List of symbols for chapter 6 . . . 58
6.1 Introduction . . . 60
6.2 System parameters . . . 60
6.3 Parameter correlations . . . 62
6.4 Energy calculations . . . 65
6.5 The influence of vibration frequency . . . 70

Chapter 7. Conclusions and Recommendations **72**
List of symbols for appendix 7 . . . 72
7.1 Overview . . . 72
7.2 Conclusions . . . 74
7.3 Future work . . . 75

Appendix A. Experimental Test Results **76**
List of symbols for appendix A . . . 76

Appendix B. DEM Simulation Results **89**
List of symbols for appendix B . . . 89

Appendix C. Vibration Response of a Single Degree of Freedom System **102**
List of symbols for appendix C . . . 102
C.1 Introduction . . . 103
C.2 Viscously damped single degree of freedom systems . . . 103

Appendix D. Estimation of Vibration Parameters **105**
List of symbols for appendix D . . . 105
D.1 Least squares formulation . . . 106
D.2 Levenberg-Marquardt algorithm . . . 107

Appendix E. Particle contact parameters **109**
List of symbols for appendix E 109
E.1 Introduction 110
E.2 Hertz contacts 110
E.3 Linearisation of Hertz stiffness 116

Appendix F. Matrix Tensor Notation **118**
F.1 Basic vector notation 118
F.2 Vector transformations 120
F.3 Vector rotations 121

List of References **122**

List of Illustrations

Figures

1.1 Twisted mode vibrations of the Tacoma Narrows Bridge 1
1.2 Schematics of types of particle impact dampers 3
1.3 Spacecraft cryogenic structure with integrated particle dampers 3
1.4 The main tuned mass damper atop Taipei 101 4
1.5 Self tuning mass damper 4

2.1 Acceleration ratio (Γ / Γ_R) in relation to centrifugal acceleration (Γ_R) . . 16
2.2 Frequency response function of a SDOF system with a particle damper . 16
2.3 Classifications of contacts 19

3.1 Experimental equipment 24
3.2 Schematic layout of test beam assembly 24
3.3 Static strain gauge calibration 26
3.4 Correction of tip displacement in relation to rotation 26
3.5 Frequency response illustrating the excitation related to the rotation velocity 29
3.6 Beam natural frequency f_n 30
3.7 Beam damping coefficient, ζ 30
3.8 Equivalent beam mass, m_e 31
3.9 Equivalent beam stiffness, k_e 32
3.10 Equivalent beam damping factor, c_e 32

4.1 Containers 34
4.2 Ratio between particle mass and vibrating mass 36
4.3 Example data 37
4.4 Instantaneous frequency with HVD method 40
4.5 Example of test data 42

5.1 Equivalent SDOF mass-spring-damper system for a rotating beam with tip container 45
5.2 DEM normal and shear contact parameters 48
5.3 Setup and simulation procedure for DEM simulation 53
5.4 DEM particle motion 55
5.5 Peak amplitudes for a DEM simulation 55
5.6 Example of DEM test data 57

6.1 Example of fill height calculations 60
6.2 Fill height calculations for balls against sidewall 61
6.3 Parameter correlations 64
6.4 Example energy analysis 68
6.5 Example granular temperature calculation 69
6.6 Example of DEM test data comparing a beam with double the stiffness to the standard configuration 71

7.1 Particle damper performance factors 73

A.1 Test result for container A with ⌀4 mm balls 77
A.2 Test result for container A with ⌀3 mm balls 78
A.3 Test result for container A with ⌀2 mm balls 79
A.4 Test result for container B with ⌀4 mm balls 80
A.5 Test result for container B with ⌀3 mm balls 81
A.6 Test result for container B with ⌀2 mm balls 82
A.7 Test result for container C with ⌀4 mm balls 83
A.8 Test result for container C with ⌀3 mm balls 84
A.9 Test result for container C with ⌀2 mm balls 85
A.10 Test result for container D with ⌀4 mm balls 86
A.11 Test result for container D with ⌀3 mm balls 87
A.12 Test result for container D with ⌀2 mm balls 88

B.1 DEM simulation result for container A with ⌀4 mm balls 90
B.2 DEM simulation result for container A with ⌀3 mm balls 91
B.3 DEM simulation result for container A with ⌀2 mm balls 92
B.4 DEM simulation result for container B with ⌀4 mm balls 93
B.5 DEM simulation result for container B with ⌀3 mm balls 94
B.6 DEM simulation result for container B with ⌀2 mm balls 95
B.7 DEM simulation result for container C with ⌀4 mm balls 96
B.8 DEM simulation result for container C with ⌀3 mm balls 97
B.9 DEM simulation result for container C with ⌀2 mm balls 98
B.10 DEM simulation result for container D with ⌀4 mm balls 99
B.11 DEM simulation result for container D with ⌀3 mm balls 100
B.12 DEM simulation result for container D with ⌀2 mm balls 101

C.1 Schematic of a damped single SDOF system with base excitation. 103

E.1 Two curved surfaces in contact 110
E.2 Geometric coefficients for elliptic Hertz contacts 112
E.3 Correction factor c_c for ball-cylinder contacts 114
E.4 The von Mises stress coefficient c_e for a circular contact 116

F.1 Vector transformations 120

Tables

4.1 Container parameters 35
4.2 Ball parameters 35
4.3 Particle damper test matrix 36

5.1 PFC3D cylindrical container parameters 46
5.2 PFC3D Hertz contact ball parameters 49
5.3 Comparison between PFC3D and Hertz normal contact parameters . . . 49
5.4 DEM friction and damping parameters 54

6.1 Ball fill parameters 62
6.2 Container cavity aspect ratio 62

E.1 Correction factor for ball-cylinder contacts 115

Nomenclature and Abbreviations

List of symbols

The wide variety of subjects covered in this dissertation make it impractical to compile a single set of symbols covering all the parameters and variables used. Instead, every chapter has its own set of symbols applicable only to that chapter. Where a variable appears in more than one list, care was taken to reuse the same symbol for the same variable.

Vector-tensor notation

The vector-tensor notation in this dissertation is according to the Hassenpflug notation (Hassenpflug, 1993, 1995). An overview of the notation is given in appendix F.

The use of the Einstein index notation for tensors is limited and will be clear from the context where it is used.

Units and numbers

All units and numbers in this dissertation are in accordance with the SI standards as prescribed in the South African Standard SABS M33a:1992. Note that the *comma* is the only recognised decimal indicator for numbers in South Africa, but the decimal point was used throughout this dissertation because of software restriction for automated graphs and tables, etc.

The practices for formatting and usage outlined in the NIST Special Publication 811 (Thompson and Taylor, 2008) were followed.

Acronyms

DEM	discrete element method
COR	coefficient of restitution
EMD	empirical mode decomposition (Huang *et al.*, 1998)
FEM	finite element method
HHT	Hilbert-Huang transform (Huang *et al.*, 1998)
HVD	Hilbert vibration decomposition (Feldman, 2006)
PD	particle damper
PFC3D	Particle Flow Code DEM software
SDOF	single degree of freedom

Chapter

1

Introduction

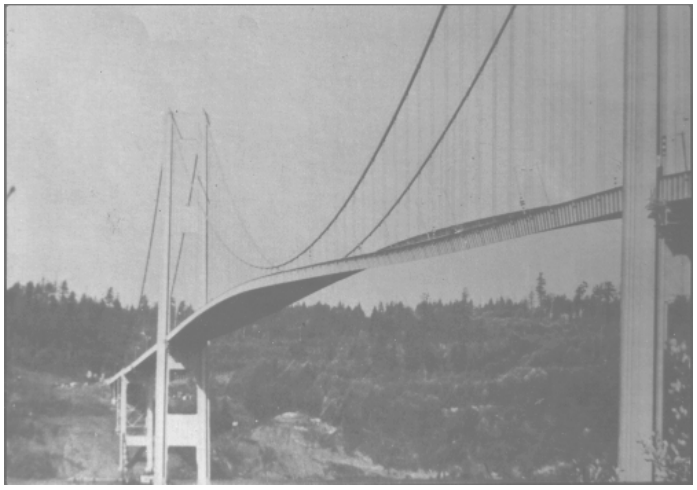

Figure 1.1. Twisted mode vibrations of the Tacoma Narrows Bridge. Photo source: Wikipedia

1.1 Background

1.1.1 Vibration and damping

Excessive stresses and strains caused by vibrations are one of the major causes for failures of mechanical systems and structures. When the vibration excitation frequency is close to the resonant frequency of a lightly damped structure it can cause a catastrophic failure, because the vibration amplitude can become very large. One of the most famous examples is the collapse of the Tacoma Narrows Bridge, also known as the "Galloping Gertie" in 1940. Figure 1.1 shows the bridge undergoing twisted mode vibrations due to aerodynamic flutter.

For unbalanced rotating machinery such as shafts, fans and turbines, many catastrophic failures have occurred when the rotation velocity is near the resonant frequency of the system. This situation often occurs during shutdown when the rotation velocity is near the system resonant frequency for a significant time. Vibrations can also significantly reduce the fatigue life of systems.

In the design of machinery and structures, detailed attention must be paid to the reduction of vibrations to reduce noise, increase fatigue life and prevent catastrophic failures. This is achieved by firstly reducing the source of vibrations through isolating the system and the dynamic balancing of rotating parts. Secondly, by increasing the damping of members subjected to vibrational load.

Damping can either be active, semi-active or passive. Active damping is when energy is removed from the system through feedback in a controlled system. Active damping is also achieved by exerting a counter force or moment in a controlled manner. An example of this is with a layer of piezoelectric material that can exert a bending moment on the structure when an electric current is applied to it.

In semi-active damped systems, the otherwise passively generated damping is modulated according to a parameter tuning policy, with only a small amount of control effort. An example is the semi-active suspensions in modern motor vehicles utilising viscous fluid dampers with variable orifices, or dampers filled with magneto rheological viscous fluids that change viscosity when subjected to a magnetic field. The damping is varied according to the road conditions. There are also fully active vehicle suspensions that monitor the road conditions and vehicle motion and change the damping in a controlled manner.

Passive or uncontrolled dampers use many different techniques to dissipate the energy of a vibrating structure. The broad categories are viscoelastic material applications, friction devices, particle and tuned mass dampers, viscous fluid dampers, and isolators. The *focus* of this dissertation is on the *performance of particle dampers*.

1.1.2 Brief overview of particle dampers

Particle dampers (PDs) are composed of a container filled with one or more particles (metals, ceramics, etc.). The devices function by dissipating energy through inelastic impacts and friction between the particles and the walls, and between the particles themselves. PDs are simple and inexpensive devices that have a wide range of application. Figure 1.2 shows the general types of particle and tuned mass dampers.[1] In the figure the spring, damper and box represent the vibrating host structure, while the contents of the box indicated the type of damper.

The main advantage of PDs over traditional damping devices is that they can function under extreme conditions such as temperatures that can exceed 600 °C and over a wide range of frequencies (Tomlinson *et al.*, 2001). Particle damping has been experimentally proven to be very effective, even if the ratio of total particle mass to the mass of the primary system is very small (Hollkamp and Gordon, 1998;

[1]There is no general consensus in the literature about the naming conventions for the different types of PDs. For the purpose of this dissertation, we will use the three types shown in Figure 1.2. Note that there are also other types of impact dampers, such as the “bean bag” dampers that encloses the particles in a secondary container (Cempel and Lotz, 1993).

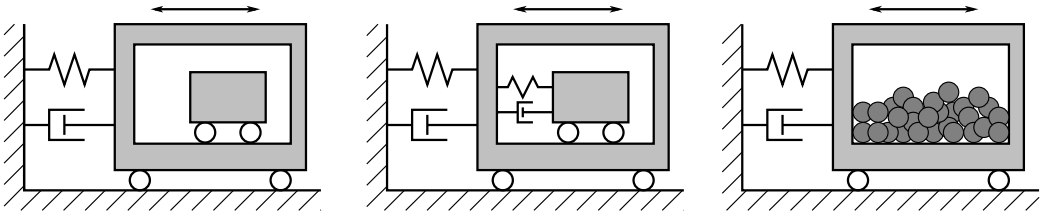

(a) Impact damper (b) Tuned mass damper (c) Particle damper

Figure 1.2. Schematics of types of particle impact dampers

Papalou and Masri, 1998; Friend and Kinra, 2000). The main disadvantage is that they are primarily high amplitude (or acceleration) damping devices. Cempel and Lotz (1993) show that for lateral vibrations PDs are not effective below the $0.3\,g_0$ acceleration level because of static friction.

For the placement of particle impact dampers on a structure, the points of highest acceleration are identified with a finite element method (FEM) analysis or with acceleration measurements. A damper is then selected for the measured parameters. Figure 1.3 is an example of a spacecraft cryogenic structure with integrated PDs (Pendleton *et al.*, 2008) that was designed following this procedure.

Impact dampers

Impact dampers are designed to damp a specific frequency. There are two basic situations when vibration response is dominated by one frequency: the response results from either a resonance or mode at that frequency, or from a strong excitation at that frequency. One of the first applications was a impact damper for controlling aircraft flutter, fatigue, and vibration by Lieber and Jensen (1945).

Despite their simple design, the dynamics of impact dampers can be very complex. An analysis of impact dampers is given by De Souza *et al.* (2005) for motion perpendicular to gravitation. Duncan *et al.* (2005) and Ramachandran and Lesieutre (2008) theoretically investigated the motion of mass dampers in the direction of

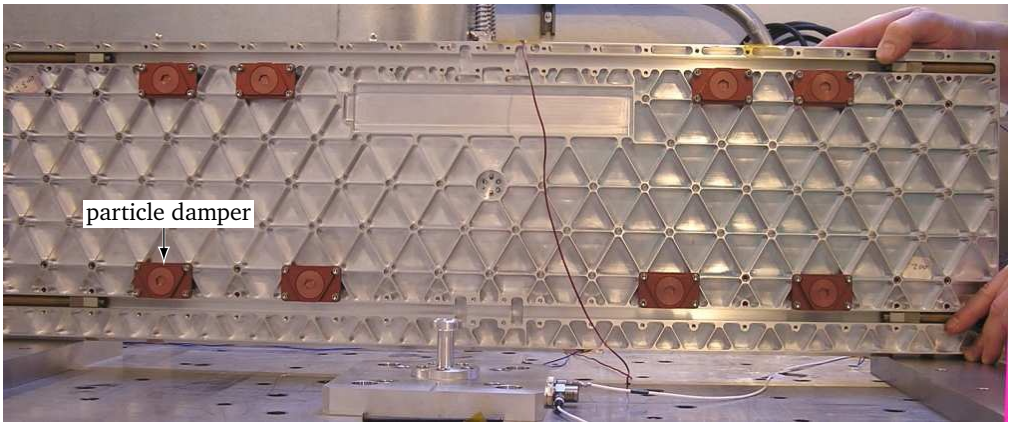

Figure 1.3. Spacecraft cryogenic structure with integrated particle dampers (Pendleton *et al.*, 2008)

gravitation, while Marhadi and Kinra (2005) conducted experiments for the same configuration.

Tuned mass dampers

Tuned mass dampers shown in figure 1.2(b) are devices that are designed to damp a specific frequency. They are used in diverse fields such as power transmission line isolators, motor vehicle suspensions, and tall buildings. An interesting example is the 508 m high Taipei 101 skyscraper, shown in figure 1.4, with its 660 t pendulum that serves as a tuned mass damper. This will enable the building to withstand winds up to 216 km / h and the strongest earthquakes that may occur in a 2500 year cycle.

Figure 1.5 illustrates an example of a self tuning mass damper for turbine blades by Duffy (2004). The damper geometry, including the radii of the ball and spherical trough and the placement of the ball, can be set such that the ball's rolling resonance frequency is equal to the frequency of excitation encountered at a specific speed.

The dynamics of tuned mass dampers can be very complex, and a detailed theoretical analysis is given by František (2003).

Particle dampers (PDs)

PDs are derivatives of single particle impact dampers, where the particles are placed in containers attached to a structure or inside voids in the structure, the so called non-obstructive particle damping (Panossian, 2002).

The range of applications of PDs is vast. Panossian (1992) drilled holes in a liquid oxygen inlet tee on the space shuttle main engine where high amplitude vibrations caused the formation of cracks. The holes where then filled with metal particles, thereby reducing the vibrations substantially. Simonian (1995) attached a PD to the tip of a satellite antenna boom to reduce vibrations. Ema and Marui (2000)

Figure 1.4. The main tuned mass damper atop Taipei 101. Graphics source: Wikipedia

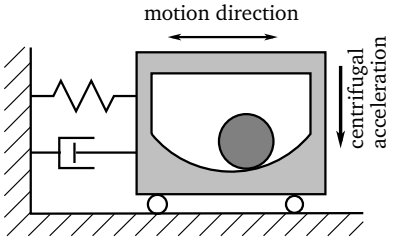

Figure 1.5. Self tuning mass damper — schematic of ball-in-trough configuration (Duffy, 2004)

improved the damping capability of boring tools and suppression of chatter vibration with PDs. Velichkovich and Velichkovich (2001) used a PD to control vibrations during deep oil and gas drilling. Simonian (2004) gives an in-depth overview of applications in diverse disciplines such as aerospace, ground transportation and high performance sporting equipment industry.

Aubert *et al.* (2003) did a comparative experimental study on the effectiveness of PDs versus tuned mass dampers for vehicle systems. It was found that tuned mass dampers and PDs of equal mass had similar performance. Particle damping is effective over a range of excitation, but poor control is seen when the excitation is too high or too low.

Another field of research is the use of low-density particles. Nayfeh *et al.* (2002) found that a low-density granular fill can provide high damping of structural vibration if the speed of sound in the fill is sufficiently low.

Of interest in this dissertation is the performance of PDs under centrifugal loads, for example in turbine or fan blades. In this area there are very few published applications. The self tuning mass damper by Duffy (2004) gave promising results. Panossian (1991) investigated the higher frequency range up to 5000 Hz. Significant decrease in structural vibrations was observed even when the holes were completely filled and subjected to a pressure of 24 MPa to simulate centrifugal loading.

1.1.3 Analytical and numerical analysis of PDs

Most engineering applications of PDs employed experimental techniques to arrive at viable solutions for specific applications. Because of the complexity of the dynamics of PDs, most of the earlier analytical methods focused on modelling them as an "equivalent single mass" impact damper (Papalou and Masri, 1998; Friend and Kinra, 2000).

In the field of granular flow and dynamics, the discrete element method (DEM) numerical tools were developed, which are now used for the analysis of PDs. With DEM the mechanical behaviour of a system of particles are simulated. The basic building blocks are finite sized particles and wall surfaces. The mechanical behaviour simulation is generally classified into two different approaches: the "hard sphere" or event-driven method and the "soft particle" method.

In the "hard sphere", event-driven method (e.g. Luding, 1994, 2004), the particles are assumed to be perfectly rigid and follow an undisturbed motion until a collision occurs. Due to the rigidity of the interaction, the collisions occur instantaneously with accompanying momentum transfer. It is mainly used for collisional, dissipative granular gases. This method is useful for analysis of single particle impact dampers, but not for multi particle dampers. As further research, it might be worthwhile to revisit some of the earlier impact damper calculations with the newest constitutive models that have been developed in this field.

The so-called "soft particle" molecular dynamics were pioneered by Cundall and Strack (1979). The particles are allowed to overlap or penetrate each other. Constrains on the physical space that a particle can occupy at a specific time is included with contact or penalty forces related to the amount of overlap and contact velocity between particles or between particles and walls. The motion of the system

is modelled by the integration of the Newton-Euler equations for motion of every individual particle. This is the approach taken in this dissertation.

The DEM simulations are particular useful to numerically duplicate physical experiments and thereby obtain information about the particle motion and system parameters that are difficult or impossible to determine experimentally. Over the past couple of years, a number of papers have been published where DEM was used to simulate PDs. As an example Mao *et al.* (2004*a*,*b*) could successfully reproduce experimental results.

1.2 Objectives and scope of research

> *The main research objective of this dissertation was to determine experimentally and numerically the performance parameters of particle dampers under centrifugal loads.*

The scope of the research was limited to the experimental and numerical investigation of the free decay of a vibrating cantilever beam under centrifugal loads with a PD at the tip. To minimise the number of variables, only one beam was used (single vibration envelope) and the PDs tested were constrained to be all of the same mass.

A test bench was developed. It consists of a rotating cantilever beam with a tip container filled with particles. The tip container functions as a PD and was placed at the position of maximum displacement while the beam vibrates. During operation the tip of the beam was displaced with a cam mechanism, and after release the beam could vibrate freely. The decay in the vibratory motion of the tip of the beam was measured over a range of centrifugal loads.

Four different tip containers with identical mass and cavity diameters, but varying depth were used. The containers were filled with uniform sized steel ball bearings of three different diameters, but again all with the same mass. This resulted in a series of twelve different PDs, all with identical total mass, but with different configuration. The objective with this selection of PDs was to investigate the influence of particle size, number of particle-particle contacts and void space inside the container on the performance of the PDs.

The experiments were duplicated numerically with a DEM model. The DEM model was calibrated against the experimental data. This model could then be used for a more in-depth investigation of phenomena occurring when PDs are under centrifugal loads.

This research is particular relevant for PDs in a “low” acceleration environment such as experienced by rockets during launch, by banking aircraft or even in cornering ground vehicles. There is very little — if any — open literature available for PDs in this operating regime and the aim of this research is to gain a better understanding in this area.

1.3 Outline of the dissertation

The outline of this dissertation is as follows. In this chapter, chapter 1, a short overview of vibration and damping is given. The different types of dampers are discussed and a more detailed overview of PDs is given. The objective and scope of this research is also defined.

In chapter 2 a detailed literature review of vibrated granular media and PDs is given. The general principals of DEM are discussed and the different applications of DEM to simulate PDs and the results obtained are investigated. The important area of signal processing of vibration data is also covered in detail.

Chapter 3 discusses the design and operation of the experimental equipment: the calibration of measurement and data gathering system, the numerical methods for data extraction and the system characterization tests. In chapter 4 the full experimental tests with data processing methods are given. The final results are in appendix A.

The DEM simulation construction is detailed in chapter 5. The experimental tests were duplicated numerically and the results are presented in appendix B.

In chapter 6 a more in-depth look at the results and parameters influencing PD performance are discussed, with the final conclusions drawn and discussed in chapter 7.

Chapter

2

Literature Review

List of symbols for chapter 2

Constants

$g_0 = 9.81\,\mathrm{m/s^2}$ standard gravitational acceleration

Variables

a_g	propagation velocity of pressure wave in granular medium	[m/s]
a	wave propagation speed in a solid	[m/s]
A	vibration amplitude	[m]
c_i	mono-component functions	
d	particle diameter	[m]
E	modulus of elasticity (Young's modulus)	[Pa]
f	driving vibration frequency	[Hz]
Fr	Froude number, $Fr{=}A\omega/\sqrt{g_0\ell}$	[−]
h_0	average particle bed height	[m]
ℓ	reference length	[m]
m	particle mass	[kg]
n_d	number of equivalent layers, $n_d{=}h_0/d$	[−]
p	pressure	[Pa]
R	rotation radius	[m]
S_Y	yield strength	[Pa]
Δt	integration time step	[s]
T_g	granular temperature (eqn. 2.5)	[J]
$\overline{\boldsymbol{v}}$	particle velocity	[m/s]
x	signal quantity	
δ	ball contact overlap	[m]

$\dot{\delta}$	ball contact velocity	[m/s]
$\dot{\delta}_{\text{in}}$	ball impact velocity	[m/s]
ϵ	coefficient of restitution (COR)	[m]
Γ	peak acceleration amplitude factor, $\Gamma = A\omega^2 / g_0$	[−]
Γ_R	centrifugal acceleration factor, $\Gamma_R = R(2\pi\Omega)^2 / g_0$	[−]
ν	Poisson's ratio for material	[−]
ρ	density	[kg/m^3]
ϱ_n	residue function	
ϑ	phase angle	[rad]
ω	driving vibration frequency, $\omega = 2\pi f$	[rad/s]
Ω	system rotation velocity	[s^{-1}]

2.1 Parameters and definitions

The following definitions and dimensionless parameters are often encountered in the literature about particle dampers (PDs) and are listed here for future reference.

Equivalent layers: The dimensionless *bed depth* or number of *equivalent layers* is defined as

$$n_d = \frac{h_0}{d} \tag{2.1}$$

with h_0 the average depth of the particle bed and d the particle diameter.

Acceleration factor: For a single degree of freedom (SDOF) vibrating system with displacement $y(t) = A\sin(\omega t)$, the acceleration amplitude is $A\omega^2$. The *peak acceleration amplitude factor* in dimensionless form is then defined as

$$\Gamma = \frac{A\omega^2}{g_0} \tag{2.2}$$

with ω the vibration frequency, A the vibration amplitude and g_0 the gravitational acceleration.

A *centrifugal acceleration factor* for centrifugal loads can be defined as

$$\Gamma_R = \frac{R(2\pi\Omega)^2}{g_0} \tag{2.3}$$

with R the system rotation radius and Ω the system rotation velocity [s^{-1}].

Froude number: The *Froude number* in fluid dynamics is given by $v/\sqrt{g_0 \ell}$ with v the velocity and ℓ a characteristic length. For a SDOF vibrating system the velocity amplitude is $A\omega$ and we can define a Froude number for PDs as

$$Fr = \frac{A\omega}{\sqrt{g_0 \ell}} \tag{2.4}$$

were ℓ can be the container length, gap between container lid and particles, etc.

Granular temperature: There exists a number of definitions for the *granular temperature*. The one used in this dissertation is the average kinetic energy fluctuation.

$$T_g = \frac{1}{N} \sum_{i=1}^{N} \tfrac{1}{2} m_i \left(\overline{\boldsymbol{v}}_i - \langle \overline{\boldsymbol{v}} \rangle \right)^2 \quad \text{with} \quad \langle \overline{\boldsymbol{v}} \rangle = \frac{1}{N} \sum_{i=1}^{N} \overline{\boldsymbol{v}}_i \tag{2.5}$$

and $\overline{\boldsymbol{v}}_i$ the velocity of particle m_i.

Wave propagation speed: Two types of elastic body waves are encountered in solid bodies. For primary or pressure waves (P-waves) the material vibrates in the direction of travel of the wave energy. The wave propagation speed for P-waves is

$$a_P^2 = \frac{K + \frac{4}{3}G}{\rho} = \left(\frac{1-\nu}{1-\nu-2\nu^2} \right) \frac{E}{\rho} \tag{2.6}$$

with K the bulk modulus, G the shear modulus, E the modulus of elasticity and ρ the density of the material. For secondary or shear waves (S-waves) the material vibrates perpendicular to the wave direction. The wave propagation speed for S-waves is

$$a_S^2 = \frac{G}{\rho}. \tag{2.7}$$

When the symbol a is used for wave propagation speed in this chapter, it can be either a_P or a_S.

In the field of earthquake engineering, two types of surface waves are also defined, but these are not relevant for loose granular matter.

2.2 Vibrated granular media

The behaviour of vibrating granular media is of great interest in a wide range of research fields. Examples are in bulk materials handling to enhance flow properties, in the geosciences and civil engineering fields for earthquakes and other man-made tremors, and in mechanical and aerospace engineering for PDs. In this section we will review general vibration phenomena observed that may be important for PDs.

Wave propagation

Goddard (1990) gives a detailed overview of wave propagation in granular materials. For Hertzian contacts between the particles, theory predicts that the elastic wave

speed a scales with $a \sim p^{1/6}$ where p is the confining pressure. Experiments have shown a scaling of $a \sim p^{1/4}$ for low confining pressures, while at high confining pressures the wave speed scales in accordance with the Hertz contact theory.

Hostler (2005) and Hostler and Brennen (2005) investigated the parameters influencing the propagation speed of a pressure waves through a particle bed. Over a wide range of experiments and simulations, the strongest influence was the wave propagation speed a of the particle material. For the confining pressure p it was confirmed that $a \sim p^{1/6}$. They also showed the influence of Poison's ratio ν on a, from which can be deducted that it was probably the speed of the P-waves that were measured.

Mouraille *et al.* (2006) simulated the propagation of elastic waves in three-dimensional regular (crystal) mono-disperse packings of spheres for both P- and S-waves. The effect of friction was also introduced to study the effect on wave propagation.

Vertical vibrations

Wassgren *et al.* (1996) and Wassgren (1997) examined the fundamental behaviour of a granular material subject to vertical vibrations with regards to the difference between shallow and deep beds, sidewall convection and surface waves. It was found that there is a fundamental difference in behaviour between shallow beds (n_d<4) and deep beds (n_d>6). For shallow beds, depending on Γ, the particles bounce around randomly in the container and little coherent motion is observed. For deep beds the particles move as a single, plastic mass. In the deep beds, again depending on Γ, phenomena such as convection cells, heaps and surface waves were observed.

The change in bulk density or solid fraction that occurs when a vessel filled with granular materials is vertically vibrated is an important industrial issue in the production, transport and packaging of granular materials. Zhang and Rosato (2006) give a good overview of the history of research in this field. Some of the important findings that may influence PDs are that the most rapid compaction occurred when 0.9<Γ<1.1, while a maximum bulk density was achieved for 1.1<Γ<1.3. The experiments of Knight *et al.* (1995), extended by Nowak *et al.* (1998) showed dependence of bulk density on the vibration history.

Brennen *et al.* (1996) experimentally investigated the expansion, $h^* = h - h_0$, of a vertically vibrating particle bed, with h the height of the bed at a particular time. They found that the bed would start to expand for $\Gamma > 1$ and that h^* would gradually increase against Γ until a sudden expansion occurs at a critical value of Γ. This critical point appears to be independent of the frequency. It was observed that the critical point is related to the inverse of the Froude number with h^* as reference length, and that $0.5 < Fr^{-1} < 1.0$ for the subcritical and $Fr^{-1} = 1.5$ for the supercritical region.

Yang and Candela (2000) used nuclear magnetic resonance to measure the density profile of a three-dimensional granular medium fluidised by vertical vibrations of the container. For $\Gamma \gg 1$ they found that the rise in centre of mass of the granular medium scale as $(A\omega)^\alpha / n_d^\beta$ with $\alpha = 1.0 \pm 0.2$ and $\beta = 0.5 \pm 0.1$. Although the

authors did not correlate their results in terms of the Froude number it is clear that *Fr* with bed depth h_0 as reference describes the scaling factor well.

Pöschel *et al.* (2000) theoretically investigated the conditions for the onset of fluidization. They derived a linearised equation for the one-dimensional motion of a stack of uniform sized particles and found the minimum amplitude for the topmost particle to separate from its neighbour,

$$A \geq \frac{g_0}{\omega^2} - \frac{5}{2}\left(\frac{h_0^5}{g_0\,\kappa^2}\right)^{1/3} \quad \text{with} \quad \kappa = \frac{2E}{\pi\rho(1-\nu^2)} \tag{2.8}$$

and h_0 the height of the particle stack.[2] Equation (2.8) shows that it is possible, depending on the particle material properties, for the material to fluidised for $\Gamma < 1$. This was confirmed experimentally by Renard *et al.* (2001). This important result is not yet properly explored for the optimization of PDs. It suggests that the operation envelope of a PD may scale with $a^{-4/3}$. In other words a material with a higher wave propagation velocity can still damp at a lower A or Γ. An interesting possibility is to select the particle damper parameters so that the particle bed resonance ($A \to 0$) is close to the frequency where damping is required.

Horizontal vibrations

An experimental investigation of a horizontally shaken particle bed was conducted by Evesque (1992). He observed convective rolls where the particles rise in the centre and dive along the side wall. Liffman *et al.* (1997) conducted a discrete element method (DEM) simulations of a horizontally shaken particle bed. They found no bulk motion for $\Gamma \leq 0.5$. For $0.5 < \Gamma \leq 1.2$ a single convective roll and in the range $1.2 < \Gamma \leq 2.2$ four rolls with a large amount of surface agitation were observed. They found the mechanism driving the convection rolls is avalanching and described it as follows: During each half cycle, particles pile up against one wall and a gap appears between the heap and the other wall. The gap allows space for particles to fall into. There are two ways for particles to fill this gap. The surface of the pile becomes sufficiently steep to cause an avalanche, or sloshing material can be thrown into the gap. During the next half cycle, the gap closes and the avalanched particles push other particles into the heap interior.

Ristow (1997) investigated the horizontal vibration of a particle bed experimentally and with DEM simulations. The transition of the bed from a solid-like behaviour to a fluid-like state was investigated. A well defined transition point was found that depends on Γ and is a strong function of the inter-particle friction. The coefficient of restitution (COR) did not have any influence. It was also shown that the granular temperature (equation (2.5)) is a function of Γ.

Tennakoon *et al.* (1999) conducted experiments with a 3-dimensional particle bed. They found hysteretic behaviour for the thickness of the liquefied material. For an increase in Γ there is well defined transition to liquefaction of the material. If the Γ is decreased below this transition point, the material stays liquefied until

[2]The units in equation (2.8) are not consistent, indicating that there may be a typing error in the original publication.

a critical point where all relative motion stops. This transition point was strongly dependant on the inter-particle friction. Metcalfe *et al.* (2002) revisited these experiments and also conducted DEM simulations. One of their findings was that if a slight overburden is added, the nature of the transition is substantially changed from backward/hysteretic to forward/nonhysteretic.

An experimental investigation of horizontal shaking by Medved *et al.* (1999) reported that the convective flow depends strongly on the boundary conditions. These include the container surface roughness and the ratio between the filling height and the container width. They also tested different particle shapes, but found no discernable effect.

Hsiau *et al.* (2002) conducted an experiment with a cylindrical container shaken horizontally in the radial direction of the cylinder. A smooth and very rough wall (glued sandpaper) were used. They found that the rough wall induced more convection and increased the granular temperature.

Simultaneous horizontal and vertical vibrations

Tennakoon and Behringer (1998) studied a particle bed that is subjected to simultaneous horizontal and vertical sinusoidal vibrations. Under certain conditions of vibration a granular system will spontaneously develop a slope, the angle of which increases with time until an equilibrium is reached. The phase difference between the components of vibration in the two directions becomes a key control parameter for the resulting motion. A simple friction model can approximately describe the steady states and the transition to convection. King *et al.* (2000) revisited these experiments and deduced values for an effective coefficient of friction for the various slope angles and the downhill and uphill movement.

2.3 Particle damper characteristics

In our experimental procedure shown in figures 3.1 and 3.2, we investigated a PD vibrating in the vertical direction while under centrifugal loads. For low centrifugal loads ($\Gamma_R < 1$) the damping characteristics can be compared to those found in the literature for vertical vibration. It is important to realise that when the centrifugal acceleration exceeds $1\,g_0$ or $\Gamma_R > 1$, the particles are no longer free to bounce up and down, but tend to move along the side wall. If the centrifugal acceleration is increased further, the particles move in a "sloshing" motion along the wall until the centrifugal forces become too high to allow any relative motion between the particles. It is therefore clear that the analysis of PDs in horizontal motion perpendicular to gravity is more appropriate to understand the damper characteristics in this case.

Large number of PD publications are for specific implementations. A few of these have already been discussed in the introduction in section §1.1.2. For the rest of this section we will focus on the general analysis and design procedures for PDs.

General PD design procedures

Papalou and Masri (1996, 1998) did a wide range of experiments with PDs under

horizontally and vertically vibrating systems with random excitations. They studied the influence of mass ratio, particle size, container box dimensions, excitation levels, and direction of excitation, and proposed design procedures based on equivalent single particle dampers. Some of the important findings were that there is an optimum length/width aspect ratio and void space inside the container. It was also found that an optimally designed single particle damper is more efficient than a multi-particle damper of equal mass.

Olson *et al.* (1999) and Fowler *et al.* (2000) derived an analytic model of a particle damper using the Hertz theory of elastic contact to model the particle-particle collisions. Their model shows that both collisions and internal friction contribute significantly to the overall energy dissipation. Extending this model further, Fowler *et al.* (2001) gave a full engineering design procedure for selection and implementation of PDs in structural systems.

Yang (2003) performed a detailed experimental analysis of PDs. It involved investigating the effects of vibration amplitude, excitation frequency, gap or void space, particle size, and mass ratio on the damping effectiveness of PDs. An important conclusion was the presence of an optimum gap clearance for maximum damping. The final outcome was master design curves for PDs.

PDs under vertical vibrations

Hollkamp and Gordon (1998) tested a cantilever beam with 8 holes along its length filled with particles. Their findings were that the effectiveness of the PDs depends strongly on excitation amplitude, particle volume fraction, particle mass and particle size. The particle material and shape had little influence. An important observation they made is that the damping increased with amplitude up to a maximum and then decreased if the amplitude was increased further.

Friend and Kinra (1999, 2000) conducted an extensive analysis of the performance of a PD and derived an analytical SDOF model. They performed a dimensional analysis and defined a range of dimensionless parameters. It was shown that the specific damping capacity has a critical or maximum value in terms of Γ and that this critical value depends heavily on the void space. Marhadi (2003) and Marhadi and Kinra (2005) extended this work by investigating the influence of particle material and size. They found that the specific damping capacity normalised for the total particle mass is independent of the total number of particles and material type.

Saeki (2001) investigated the influence of container length (void space) on the performance of PDs experimentally and numerically with DEM. He compared the results of horizontal to vertical vibrated systems and concluded that the behaviour of the particles is different but the overall system behaviour is similar.

PDs under horizontal vibration

Liu *et al.* (2005) performed a series of response-level-controlled tests on PDs with different geometries. They found for low response levels or effective system acceleration (Liu *et al.*, 2002) that the particles act as an added mass lowering the system resonance frequency. For an increase in response level, the damping increases and

the resonant frequency of the system shifts towards that of the empty PD. It was also found that the cavity aspect ratio (length/diameter) plays an important role in the performance of PDs. Rongong and Tomlinson (2005) in a follow up study, experimentally investigated a large number of parameters effecting PDs. For low damper aspect ratios, particle fluidisation occurs at higher amplitudes. Dampers fluidising at higher vibration levels have higher energy dissipation. For particle size and material type they found that it had a significant influence on the energy dissipation, contrary to vertical vibrations. The particles were also coated with an oil film to investigate the effect of friction and it was found that the oil reduces the amplitude dependance and the damping. This shows that friction is the key driver of PD effectiveness.

Witt and Kinra (2006) tested various particle damper configurations under horizontal vibrations. For a single layer of large uniform sized balls it was found that the initial clearance between the tightly packed balls and the container wall has no influence on the specific damping capacity for large clearances. They observed significant damping for $0.25<\Gamma<1$ and a significant reduction in damping around $\Gamma=1$. For $\Gamma>1$ the damping increases again. If the clearance is decreased, a maximum specific damping capacity occurs just below $\Gamma=1$. For smaller balls with the same total mass it was found that the clearance has no influence. For multiple layers of balls the damping increased with an increase in void space between the balls and the container. It was also observed that larger balls damp more effectively compared to smaller balls with the same total mass.

Particle dampers under centrifugal loading

Very few publications exist in the open literature about PDs under high centrifugal loads such as in turbine or fan blades. No literature could be found for the lower acceleration regime as for banking aircraft or rockets during launch.

Panossian (1991) simulated centrifugal loading by applying forces up to 300 N with a pressure piston to the particles inside a damper container. Unfortunately the filled particle mass is not listed, but for a container with 4 mm diameter, 50 mm high, filled with steel balls, the particle mass would be more or less 3 g. The force divided by the particle mass gives $\Gamma_R=10\times10^3$. Damping was obtained with a peak acceleration amplitude of $\Gamma=350$ or for a ratio of $\Gamma/\Gamma_R\approx0.035$. Note that the intention was to simulate the centrifugal environment of a 280 mm diameter turbine disk rotating at 35 000 min^{-1} or for $\Gamma_R=190\times10^3$.

Preliminary test conducted by Flint (1999) showed a PD functioning at high centrifugal loads ($\Gamma_R > 5000$) damping the second bending moment. Flint *et al.* (2000) compiled available data on the excitation acceleration ratios, Γ/Γ_R, from open publications (see figure 2.1). It is clear the centrifugal stiffening decreases the amplitude exponentially despite the increase of resonance frequency with centrifugal loading.

2.4 Data reduction and parameter extraction

The dynamics of particle dampers are nonlinear and non-static. The natural frequency and damping of a vibrating system with a particle damper depends on the

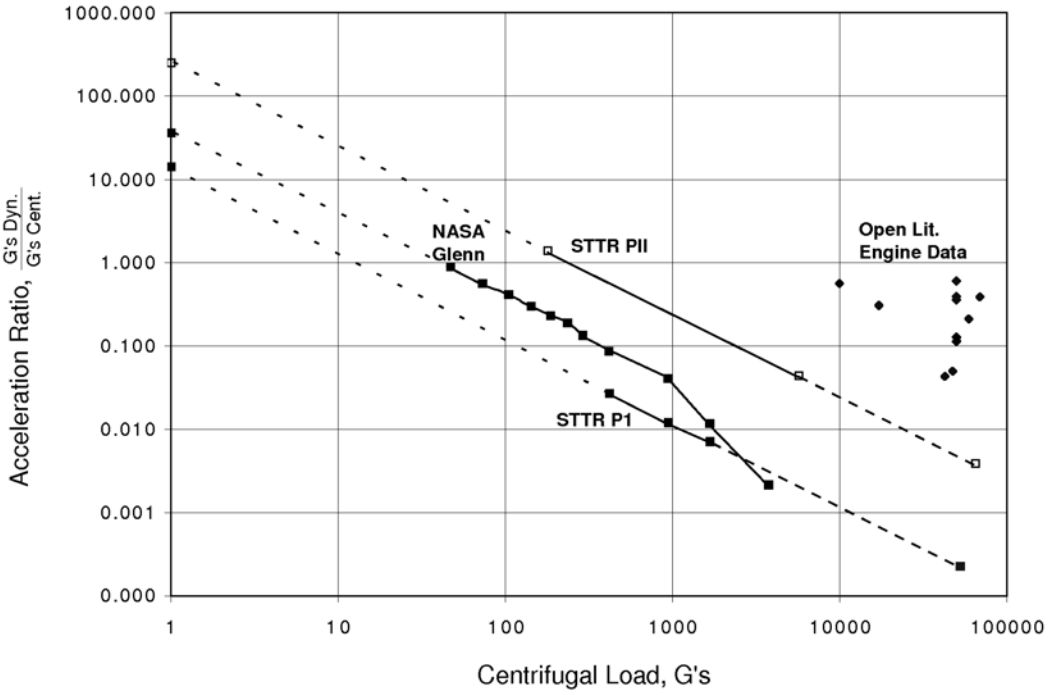

Figure 2.1. Acceleration ratio (Γ / Γ_R) in relation to centrifugal acceleration (Γ_R) (Flint *et al.*, 2000)

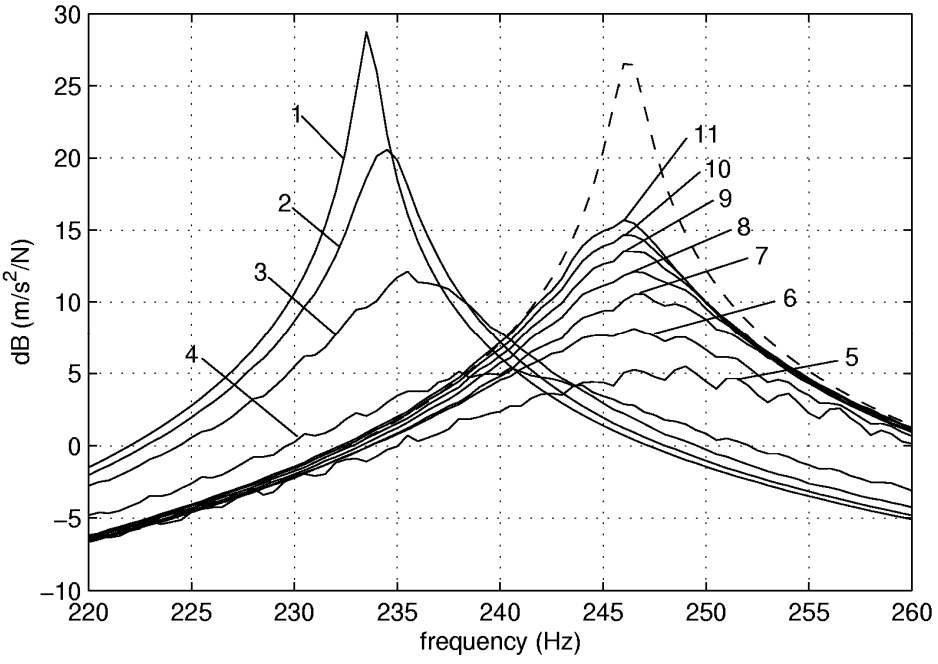

Figure 2.2. Frequency response function of a SDOF system with an empty enclosure as the vibrating mass (dashed line) and with particles filled into the vibrating mass (solid lines). Each curve is of different amplitudes (Liu *et al.*, 2005; Wong *et al.*, 2007)

excitation state of the particles as shown in figure 2.2 from Liu *et al.* (2005) and Wong *et al.* (2007). In the literature, various methods and combinations of methods are used to obtain damping parameters and damping efficiencies.

The research into the analysis of nonlinear and non-static vibration signals is still a very active field. A review of some of the non-stationary data processing methods is given by Huang *et al.* (1998).

Classic methods such as the Fourier analysis are not able to capture the change in frequency and amplitude over time of a nonlinear and non-static signal, because they are built on the assumption of an infinite repeating signal. To overcome these shortcomings, methods such as the limited time window-width Fourier spectral analysis were introduced, where, by successively sliding the window along the time axis, a time-frequency distribution can be obtained.

The wavelet approach is essentially an adjustable window Fourier spectral analysis. It allows decomposition of a signal into its time-frequency components and can be used for the analysis of PDs. An example of obtaining hysteresis damping of a structure is by Slavič *et al.* (2003).

Some of the modern analysis methods are build around the Hilbert transform, because it allows signals to be analysed in the time domain. The Hilbert transform of a function $x(t)$ is defined by the integral equation

$$H[x(t)] = \tilde{x}(t) = \frac{1}{\pi} P \int_{-\infty}^{\infty} \frac{x(\tau)}{t-\tau}\,\mathrm{d}\tau, \tag{2.9}$$

where P denotes a Cauchy principal value, because of the possible singularity at $t = \tau$. The analytical signal $X(t)$ can then be written as the complex pair

$$\begin{aligned} X(t) &= x(t) + \mathrm{i}\,\tilde{x}(t) \\ &= |X(t)|\,[\cos\vartheta(t) + \mathrm{i}\sin\vartheta(t)] = A(t)\ \mathrm{e}^{\mathrm{i}\vartheta(t)} \end{aligned} \tag{2.10}$$

with $\mathrm{i} = \sqrt{-1}$ and the instantaneous amplitude and the phase angle

$$A(t) = \sqrt{x^2(t) + \tilde{x}^2(t)}, \qquad \vartheta(t) = \arctan\left(\frac{\tilde{x}(t)}{x(t)}\right). \tag{2.11}$$

The instantaneous or time-dependent frequency $\omega(t)$ is defined as

$$\omega(t) = \frac{\mathrm{d}\vartheta(t)}{\mathrm{d}t}. \tag{2.12}$$

The Hilbert transform can be useful on its own to obtain data tendencies, as was illustrated by Fowler *et al.* (2000) in obtaining the amplitude of a signal. The main limitation in the use of equation (2.12) is that the signal must be a "mono-component function", meaning in the most fundamental sense that the signal must be mono-harmonic or $x(t) \sim \cos\vartheta(t)$. A number of methods to overcome this limitation have been developed, such as the Hilbert-Huang transform (HHT) by Huang *et al.* (1998) and the Hilbert vibration decomposition (HVD) method by Feldman (2006). A comparison of the two methods is given by Feldman (2008).

The HHT method consists of two major steps. The first step is that with the aid of the empirical mode decomposition (EMD), a time domain signal $x(t)$ is decomposed into n intrinsic mode or mono-component functions c_i corresponding to different intrinsic time scales.

$$x(t) = \sum_{i=1}^{n} c_i(t) + \varrho_n \tag{2.13}$$

with ϱ_n a residue. Every $c_i(t)$ is obtained by finding the envelope of the signal and then fitting a spline through the average between the maximum and minimum at every time t. The second step is to perform Hilbert transforms and computing the time-dependent frequency ω_i and amplitude A_i of each c_i. The EMD algorithms are still under active development and mathematical scrutiny.

Kerschen *et al.* (2007) successfully demonstrated the implementation of the HHT algorithm for the transient resonance capturing of two coupled oscillators with essential nonlinearity. Fang *et al.* (2008) also employed it to obtain the transient response of a PD.

The HVD method by Feldman (2006) requires three procedures at every iteration step. The first is the estimation of the instantaneous frequency of the largest component. This is achieved by the low-pass filtering of the signal instantaneous frequency, assuming that $x(t)$ is a composition of mono-component signals

$$x(t) = \sum_{i} A_i(t) \cos\bigl(\textstyle\int \omega_i(t)\ \mathrm{d}t\bigr). \tag{2.14}$$

The second procedure is the detection of the corresponding envelope of the largest component $x_1(t) = A_1(t) \cos\bigl(\int \omega_1(t)\ \mathrm{d}t\bigr)$ and the third the subtraction of the largest component from the composition. On each iteration step the residual contains the lower-energy components. As a result the initial composition is automatically separated into several slowly varying oscillating components. At each iteration step, after subtracting the largest component, the instantaneous frequency of the residual will be filtered again, and the components will be separated if the difference between their frequencies is greater than the cutoff frequency value. Luo *et al.* (2007) implemented the HVD method for the analysis of particle dampers.

Another data analysis tool is the Fourier based power flow method developed by Yang (2003) for forced vibrations to obtain the equivalent system mass as a function of time. This method was implemented by Wong *et al.* (2009) to analyse experimental and DEM data.

2.5 Numerical modelling with the discrete element method

The DEM simulation techniques, as introduced earlier in section §1.1.3, and in particular the “soft particle” method pioneered by Cundall and Strack (1979) has become the tool of choice for the numerical simulations of PDs. The rest of this subsection gives a short overview of the DEM technology.

2.5.1 Basic elements

Particles are traditionally spherical to simply calculations, but can be of any arbitrary shape such as ellipsoids (e.g. Vu-Quoc *et al.*, 2000), superquadrics (e.g. Williams and Pentland, 1992; Mustoe and Miyata, 2001) or polyhedral blocks (e.g. Ghaboussi and Barbosa, 1990; Williams and O'Connor, 1995). Balls can also be bonded together to form clumps or super particles (Favier *et al.*, 1999).

2.5.2 Contact detection

In large scale DEM simulations, most of the processing time is spent finding which elements are in contact. A simple search of all possible combinations scales in terms of processing time to $\mathcal{O}(N^2)$ with N the number of balls. Better results can be obtained with partitioning or neighbour-sorting algorithms. These falls into two main classes: tree-based algorithms or binary searches which scales to $\mathcal{O}(N \log N)$ (Perkins and Williams, 2001), and spatial hashing or binning non-binary search methods, which scales to $\mathcal{O}(N)$ (Vu-Quoc *et al.*, 2000; Munjiza and Andrews, 1998). Non-binary search algorithms perform well for objects of similar size but they degrade significantly when the objects vary in size. Perkins and Williams (2001) has shown that a tree-based search can outperform the non-binary search method in this case.

2.5.3 Contact constitutive models

The contact forces (see figure 2.3) during collisions between particles are approximated with a "soft component" model. The particles are allowed to overlap or penetrate each other. The contact forces are then calculated with the use of force-displacement models from the amount of overlap between the particles or the particles and walls. The motion of the system is modelled by the integration of Newton-Euler equations for motion of every individual particle.

All the forces are calculated quasi-statically, i.e., the effects of elastic stress waves are ignored. This assumption is only valid if the duration of the collision is such that the stress waves can traverse the length of the object many times.

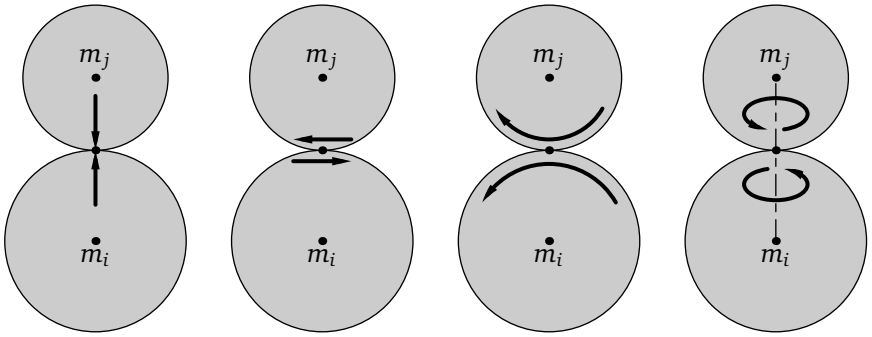

Figure 2.3. Classifications of contacts

The influence of the shear friction traction and roll on the normal pressure and contact area during a collision is generally small and can be neglected, according to Johnson (1987, p. 204). The normal and shear contact forces are therefore calculated separately and then superimposed to find the resultant force.

A good overview of the various contact models and comparisons to experimental work is given by Schäfer *et al.* (1996), Stevens and Hrenya (2005) and Kruggel-Emden *et al.* (2007, 2008)

Normal force models

The non-linear force-displacement theory of Hertz (1882) describes pure elastic impacts very well. For elastic impacts little dissipation occurs, and experiments (Falcon *et al.*, 1998*a*,*b*) showed the COR to be $\varepsilon_N \propto \dot{\delta}_{\text{in}}^{1/5}$ with $\dot{\delta}_{\text{in}}$ the impact velocity. Various researchers have introduced approximations of the Hertz theory and added dissipation with viscous or visco-elastic dampers. Kuwabara and Kono (1987) and Brilliantov *et al.* (1996) did a full rework of the Hertz theory with visco-elastic properties taken into consideration. Their results agree with the COR proportional to $\dot{\delta}_{\text{in}}^{1/5}$ that was found experimentally.

Johnson (1987, p. 363) showed for plastic collisions theory that the normal COR $\varepsilon_N \propto \dot{\delta}_{\text{in}}^{-1/4}$, which was also confirmed experimentally. It is important to note that the assumption is that yielding occurs during loading. The rebound is elastic but with an increased stiffness (increased E), because of work hardening in the material. For plastic collisions, linear force-displacement models with hysteretic damping are more appropriate. The Walton and Braun (1986) model and its derivative by Vu-Quoc and Zhang (1999*b*) are good examples for this type of contact.

The transition from elastic to plastic collisions occurs at relatively low impact velocities. For example, similar medium carbon steel balls with $S_y = 1000\,\text{MPa}$, yields when $\dot{\delta}_{\text{in}} > 0.14\,\text{m/s}$ (Johnson, 1987, p. 361). Of note here is the velocity dependent model and review by McNamara and Falcon (2005) that was conducted for vibrated granular media.

Shear force models

Mindlin (1949) expanded on the Hertz contact stress theory with the addition of oblique forces. This theory showed the concept of shear elasticity when friction is present. It also showed that when an oblique force is applied, an annulus of micro-slip develops surrounding an inner region of sticking in the contact area. If the force increases, the annulus of micro-slip grows until the whole contact area goes into a state of slip. In a subsequent publication, Mindlin and Deresiewicz (1953) showed that the stress state and the annulus of slip in the contact area are greatly dependent on the history of the loading and unloading of the applied forces. Eleven different loading cases were identified. Modelling of the full Mindlin and Deresiewicz theory in a DEM simulation is impractical and is not generally implemented. Various authors have proposed simplified Mindlin and Deresiewicz models for DEM simulations. The model by Vu-Quoc and Zhang (1999*a*,*c*) compares well with the full Mindlin and Deresiewicz theory.

A simple Coulomb friction model is often encountered in DEM publications. A combination of Coulomb friction with shear elasticity (e.g. Cundall and Strack, 1979) is the basic model used in most DEM software.

Roll models

In conventional DEM simulations, the rolling resistance between particles in contact is neglected, because rolling resistance is an order of magnitude lower than shear friction. In recent studies (Iwashita and Oda, 1998, 2000) it was clearly demonstrated that the inclusion of rolling resistance simulates shear band forming in granular material better than the traditional way of neglecting it, if compared to experimental observations. Rolling resistance also plays an important role in the development of heaps (Zhou *et al.*, 1999, 2002).

There are still many uncertainties about the loss mechanism in rolling and it is still an active field of investigation in granular materials and many other fields. Iwashita and Oda (1998) introduced rolling elasticity analogues to shear elasticity, but there are no physical grounds for this assumption. Brilliantov and Pöschel (1998, 1999) performed a detailed analytical solution for a soft sphere on a hard plane for a Hertz contact with visco-elastic dissipation. This analysis shows that the rolling resistance is directly proportional to the rolling velocity when the effect of relaxation is negligible. Yung and Xu (2003) showed that when the material relaxes slowly (e.g.: soft rubber ball) that the resistance become non-linear with respect to velocity. For the case of a hard cylinder on a soft surface, where the contact surface is not flat any more, Pöschel *et al.* (1999) showed that the rolling resistance is still related to the rolling velocity, although highly non-linear. Various experiments (Painter and Behringer, 2000; Tan *et al.*, 2006) confirmed this relationship.

A major problem with roll contacts is that there is no unambiguous definition for rolling between two moving particles. Of note is the work by Bagi and Kuhn (2004), and Kuhn and Bagi (2004) who decomposed the degrees of freedom of the two particles into rigid body motion and objective motion that is independent of the reference frame. The rolling can then be defined in terms of the objective motion.

Twist models

The influence of twisting motion between particles is normally neglected in conventional DEM simulations. A theoretical model with experimental verification is given by Dintwa *et al.* (2005).

2.5.4 Integration schemes

The selection of a time integration scheme for the equations of motion of the particles in a DEM simulations depends on the nature of the contact forces and the stability and energy conservations of the numerical methods. The contact forces are non-linear and discontinuous while friction and damping forces are also hysteretic. This forces the use of explicit single step integration methods. The alternative is to find the moment of contact accurately which is impractical for large systems. The

second order "leap-frog" central difference discretisation scheme with backward Euler approximation at time t=0 (Zhang and Rosato, 2006) is most often used in DEM simulations, among others PFC3D used in this dissertation.

Tokoro *et al.* (2005) and Rougier *et al.* (2004) analysed numerical integration methods commonly employed in DEM simulations in terms of stability and energy conservation. This analysis shows that the second order "leap-frog" scheme is good with energy conservation and conditionally stable if the time step $\Delta t \leq \Delta t_{\text{crit}}$. The critical time step is $\Delta t_{\text{crit}} = \sqrt{m/k}$ with m the minimum particle mass and k the maximum contact stiffness. O'Sullivan and Bray (2004) recommended $\Delta t < 0.17 \Delta t_{\text{crit}}$ for three-dimensional DEM simulations.

2.6 DEM simulations of particle dampers

Salueña *et al.* (1998) used DEM to model the three "phases", or regimes of damping (solid, liquid, and gas) that appear when a large number of small particles are excited in a container. The solid regime occurs when the particles move together with no relative motion between particles. The fluid regime is characterised by the formation of convection patterns and the gas regime is characterised by the independent, unpredictable motion of individual particles. The largest damping occurs at the fluidisation point (around Γ=1). It is less in the liquid regime and increases again in the gas regime.

Matchett *et al.* (2000) did a DEM validation of a vibrating bed by comparing experimental results with a simulation, using energy dissipation as a means of comparison. The DEM simulation was able to qualitatively reproduce features found in the experimental data.

Chen *et al.* (2001) used DEM to investigate the relative importance of friction. They report that for very small particles, the majority of the energy is dissipated through friction, but as the particle size increases, energy dissipation through impacts becomes more important.

Saeki (2002) Investigated the damping efficiency of a particle damper in a horizontally vibrating system experimentally and by means of DEM. The validity of DEM results is examined by a comparison of the experimental results. It is shown that the mass ratio, particle size and cavity dimensions influence the damping performance. It is also shown that the cavity dimensions and the particle radius affect the behaviour of the granular materials

Chapter

3

Experimental Setup and Calibration

List of symbols for chapter 3

c	damping factor	[N·s / m]
c_e	equivalent beam damping factor	[N·s / m]
C_κ	strain gauge correction factor	[−]
E	beam material modulus of elasticity	[Pa]
f_n	natural frequency, $f_n = \omega_n / (2\pi)$	[Hz]
h	beam thickness	[m]
i, j	indices	
I_x	beam moment of inertia, $I_x = \frac{1}{12} w h^3$	[m^4]
k	spring stiffness	[N / m]
k_e	equivalent beam stiffness	[N / m]
L	beam length	[m]
m	mass	[kg]
m_c	tip container mass	[kg]
m_e	equivalent beam mass	[kg]
R	tip container rotation radius	[m]
t	time	[s]
w	beam width	[m]
y	beam tip displacement	[m]
y_0	beam tip displacement at time $t = 0$	[m]
ε	strain gauge measurement	[µm / m]
κ	strain gauge static constant, $\kappa = \Delta y / \Delta\varepsilon$	[m^2 / µm]
ω_n	natural frequency, $\omega_n = \sqrt{k/m}$	[rad / s]
ρ	beam material density	[kg / m^3]
Ω	system rotation velocity	[s^{-1}]
ζ	viscous damping factor, $\zeta = c / (2m\omega_n)$	[−]

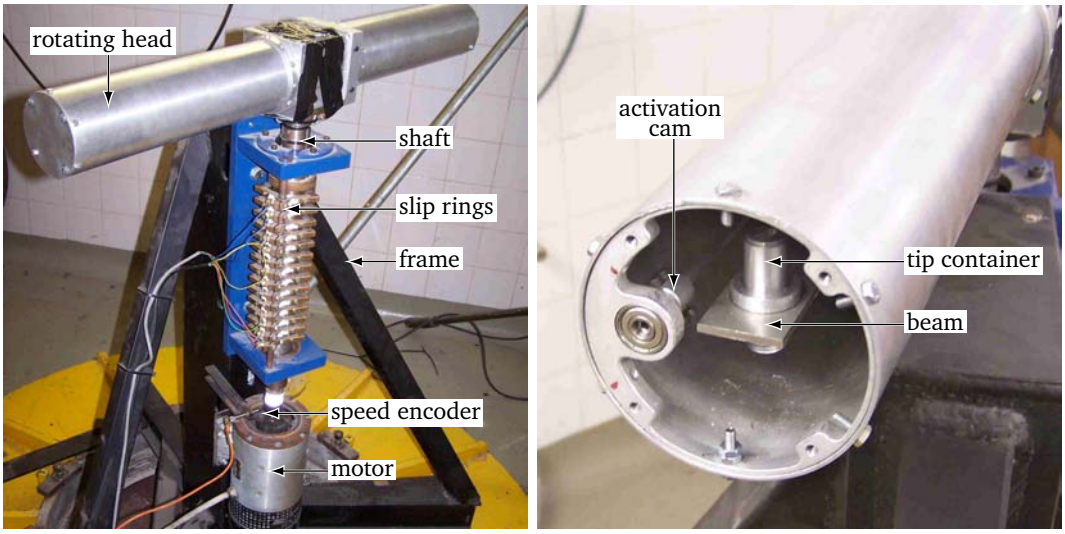

(a) Main experimental apparatus (b) Detail of internal parts and activation mechanism

Figure 3.1. Experimental equipment

3.1 Introduction

The test bench shown in figure 3.1 was developed to determine the behaviour of particle dampers under centrifugal loads up to 5000 m/s^2 (500 g_0's). The main component of the apparatus is a flexible stainless steel beam with an aluminium container at the tip that can be filled with steel balls. The system is symmetric with an identical passive side for balancing purposes. The test beam depicted in figure 3.2 was laser cut from a 3 mm AISI 304 stainless steel sheet to the dimensions shown.

h	= 3 mm	beam thickness
w	= 30 mm	beam width
L	= 360 mm	beam length
R	= 400 mm	container rotation radius

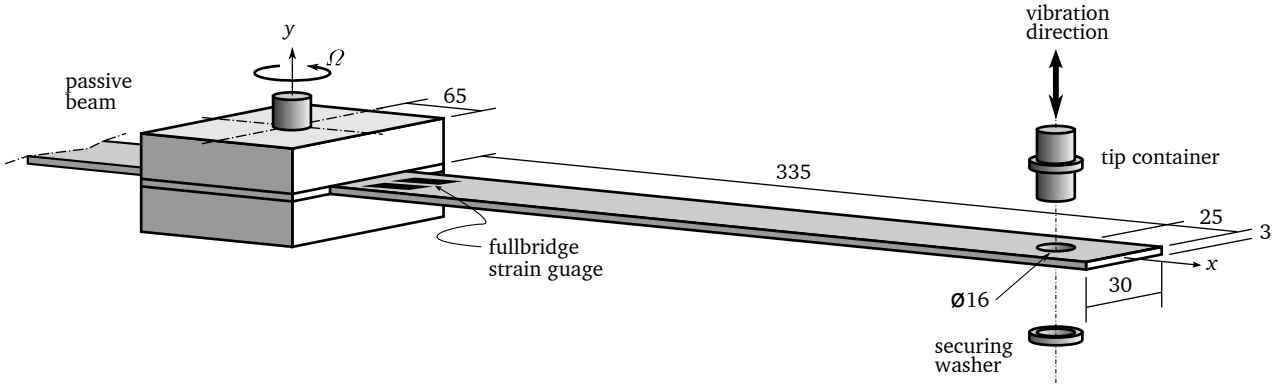

Figure 3.2. Schematic layout of test beam assembly

The material properties of the stainless steel are (Budynas and Nisbett, 2008)

ρ = 7800 kg/m^3 density
E = 193 GPa modulus of elasticity

The tip of the beam is remotely activated with a cam as shown in figure 3.1(b). The cam rotates slowly, displacing the tip of the beam. At the point of maximum displacement the beam slips of the cam and is then free to vibrate thereafter. The vibration decay is measured with a full-bridge strain gauge at the root of the beam as shown in figure 3.2. The strain signal is transferred from the rotating part across slip rings and captured with data acquisition hardware and software. The rotation of the beam and shaft is remotely controlled and rotation velocity is also measured.

The following design considerations were taken into account during the development of the test bench:

(a) The frame and shaft were made rigid and heavy to ensure a natural frequency an order of magnitude higher than that of the test beam.
(b) High tolerance pre-tensioned bearings were used and all the rotating parts were dynamically balanced.
(c) The beam was enclosed in a tube to eliminate aerodynamic flow effects during rotation.
(d) The symmetric passive beam has a natural frequency close to that of the test beam. It was therefore tied down to prevent transfer of vibrations and excitation of the test side of the apparatus.

3.2 Measurement calibration

3.2.1 Static calibration

The first calibration test that was performed was to determine the relationship between the beam tip displacement y and the strain gauge measurement ε under static conditions. The test procedure was as follows:

(a) Initialise the data acquisition system by balancing the Wheatstone bridge and zeroing the output signal.
(b) Insert calibrated measurement blocks under the tip container and measure the output strain signal, ε.
(c) Repeat the procedure for a range of tip displacements.

The result is given in figure 3.3. A linear fit of the test data in figure 3.3 gives the static calibration constant

$$\kappa = \frac{\Delta y}{\Delta \varepsilon} = 25.684 \times 10^{-6}\,\mathrm{m}^2/\mu\mathrm{m}. \tag{3.1}$$

The working range for the tip displacement is $-6.5\,\mathrm{mm} \leq y_0 \leq 6.5\,\mathrm{mm}$. It is clear that the relationship between the tip displacement and the measured strain can be assumed to be linear.

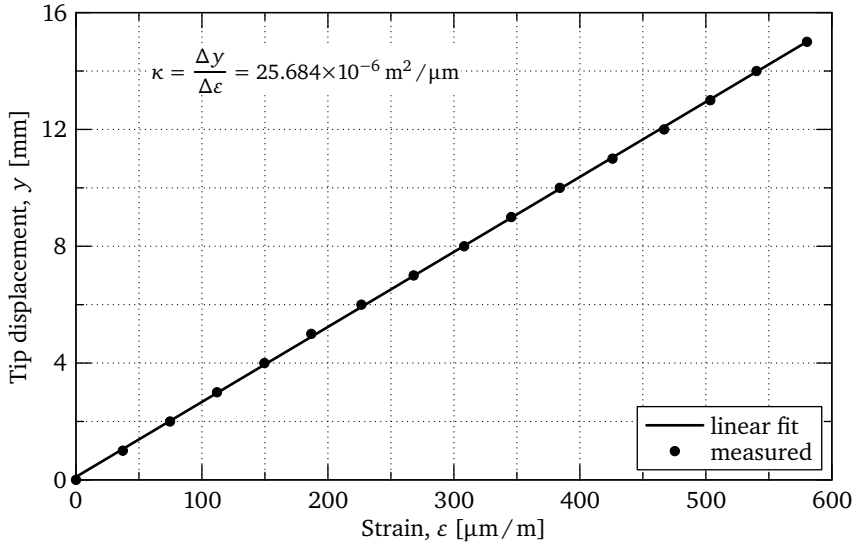

Figure 3.3. Static strain gauge calibration

3.2.2 Dynamic calibration

The full-bridge strain gauge configuration, shown in figure 3.2, measures the difference in strain between the upper and lower surfaces of the beam, in other words the strain due to the bending moment on the beam, while the strain from axial loads is ignored.

When the beam is centrifugally loaded, the centrifugal force on curved section of the beam increases bending moment at the root of the beam, resulting in the overestimation of the initial displacement, as depicted by the raw uncorrected values in figure 3.4. This was confirmed with a non-linear large strain finite element method (FEM) analysis.

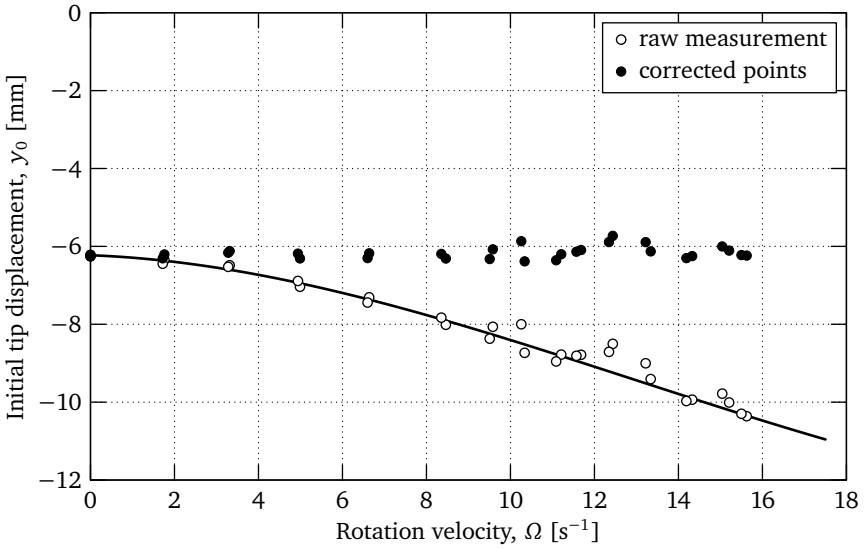

Figure 3.4. Correction of tip displacement in relation to rotation for a reference tip container with mass of 28.34×10^{-3} kg

If the assumption is made that the initial tip displacement of $\Delta y_0 \approx -6.2\,\text{mm}$ from the cam action is constant for all conditions, then the measured data can be corrected after fitting a function through the raw data as shown in figure 3.4. The correction factor is

$$C_\kappa \approx -9.910\times10^{-5}\Omega^3 + 3.850\times10^{-3}\Omega^2 + 6.372\times10^{-3}\Omega + 1\ . \tag{3.2}$$

The transformation function for measured strain data ε to tip displacement y is then given by

$$y(\varepsilon) = \frac{\kappa\,\varepsilon}{C_\kappa} \quad [\,\text{m}\,]. \tag{3.3}$$

It is important to note that equation (3.3) is only valid for the reference tip container with total mass of 28.34 g with which all the damping experiments were performed. The same procedure was followed for the other container masses used in section §3.3, but the equations are not shown here.

For the displacement measurement under dynamic conditions, while the beam is vibrating, it is assumed that the static loaded beam shape is close to the first vibration mode shape at the maximum deflection point. It is therefor assumed the resulting error in calculation of the maximum deflection is small. It is an open question if κ in equation (3.1) remains linear with centrifugal loading.

The issue of what exactly is measured with the strain gauges under dynamic conditions, may be resolved by attaching accelerometers to the beam tip to correlate the measurements, or by performing a 3-dimensional, large strain dynamic FEM simulation to verify the results. Such a study is outside the scope of this research and the approximations discussed here will be used instead, due to the sole interest in the frequency and the peak displacement values.

3.3 System characterization tests

From classical elasticity theory, it can be shown that the displacement of the tip of a cantilever beam is directly proportional to the magnitude of a static force applied to it. If a point mass is attached to the tip of an undamped cantilever beam and the mass is displaced and then released to vibrate freely, it will move with a sinusoidal motion. Andrews and Shillor (2002) provided a formal analytical proof that if the tip of the beam is viciously damped, then the vibration decay would be exponential. A non-rotating vibrating cantilever beam can therefore be approximated as a single degree of freedom (SDOF) mass-spring-damper system where the beam contributes to the total mass of the system. For the rotating beam in our experimental setup, we make the assumption that it can still be approximated as a SDOF system, but with increased stiffness and total added mass because of centrifugal effects. It is also assumed that the force-displacement relationship stays linear.

For the system characterisation we need to find an equivalent SDOF mass-spring-damper system (see figure 5.1 on page 45) that will behave the same as the beam-mass system under dynamic situations. This also simplifies the discrete element method (DEM) simulations of the system in chapter 5, because we can use the equivalent mass-spring-damper model in place of a very complex beam model (simulation wise).

3.3.1 Test procedure

A series of tests were conducted over a range of rotation velocities from $0\,\mathrm{s}^{-1}$ to $17\,\mathrm{s}^{-1}$ ($0\,\mathrm{min}^{-1}$ to $1000\,\mathrm{min}^{-1}$) with three different tip masses,

$$\begin{aligned} m_0 &= 0.00\times10^{-3}\,\mathrm{kg} - m_{\mathrm{hole}} = -4.77\times10^{-3}\,\mathrm{kg},\\ m_1 &= 13.65\times10^{-3}\,\mathrm{kg} - m_{\mathrm{hole}} = 8.88\times10^{-3}\,\mathrm{kg},\\ m_2 &= 28.34\times10^{-3}\,\mathrm{kg} - m_{\mathrm{hole}} = 23.57\times10^{-3}\,\mathrm{kg}. \end{aligned} \tag{3.4}$$

For every test, the test bench was spun up to the desired velocity and after the speed and strain gauge readout stabilised, the beam was activated. The strain gauge and velocity output were then recorded at a resolution of 2.4 kHz for 20 s or more. The recorded data was then appropriately labeled and saved. At least two readings were taken at each rotational speed setting.

3.3.2 Data analysis

Although great care was taken to balance the equipment and pre-tension the bearings, it was found during physical vibration measurements that the rotation of the equipment did induce a forced vibration on the beam as shown in figure 3.5. Furthermore is the tip of the beam released from as slow rotating off-centred cam, resulting in the excitation of higher bending and torsion vibration modes. These higher order modes have an order of magnitude higher frequency and small amplitudes compared to the first bending mode and are therefore ignored in this analysis.

To analyse the test data, the SDOF mass-spring-damper system with base excitation in appendix C was used. The Levenberg-Marquardt data fit algorithm in appendix D was used to extract the natural frequency f_n of the first vibration mode, and the viscous damping coefficient ζ from the test data. The results are given in figures 3.6 and 3.7.

Equivalent mass determination

Third order polynomials were fitted to the three data sets in figure 3.6 and are shown as the continues lines in the figure. Let $f_{n_i} = f_{n_i}(\Omega)$ for $i = 0, 1, 2$, then

$$\begin{aligned} f_{n_0} &\approx -6.549\,958\times10^{-4}\Omega^3 + 4.242\,124\times10^{-2}\Omega^2 - 1.038\,91\times10^{-2}\Omega + 19.056\,84\\ f_{n_1} &\approx -8.501\,543\times10^{-4}\Omega^3 + 4.763\,546\times10^{-2}\Omega^2 - 1.918\,06\times10^{-2}\Omega + 17.502\,18\\ f_{n_2} &\approx -8.805\,505\times10^{-4}\Omega^3 + 4.917\,415\times10^{-2}\Omega^2 - 9.400\,16\times10^{-3}\Omega + 16.176\,99 \end{aligned} \tag{3.5}$$

The equivalent beam mass m_e is the mass contribution of the beam in an equivalent SDOF mass-spring-damper system. The equivalent stiffness k_e of the beam in terms of m_e is given by

$$k_e = \omega_{n_i}^2\left(m_e + m_i\right) = 4\pi^2 f_{n_i}^2\left(m_e + m_i\right), \qquad i = 0, 1, 2 \tag{3.6}$$

Note that the assumption is made that the centrifugal load on the tip mass does no contribute toward the overall stiffness of the total system, or that k_e and m_e are independent of the added tip mass. This assumption is justified later in figure 3.9 where the k_e values for all three tip mass load cases fall on the same curve.

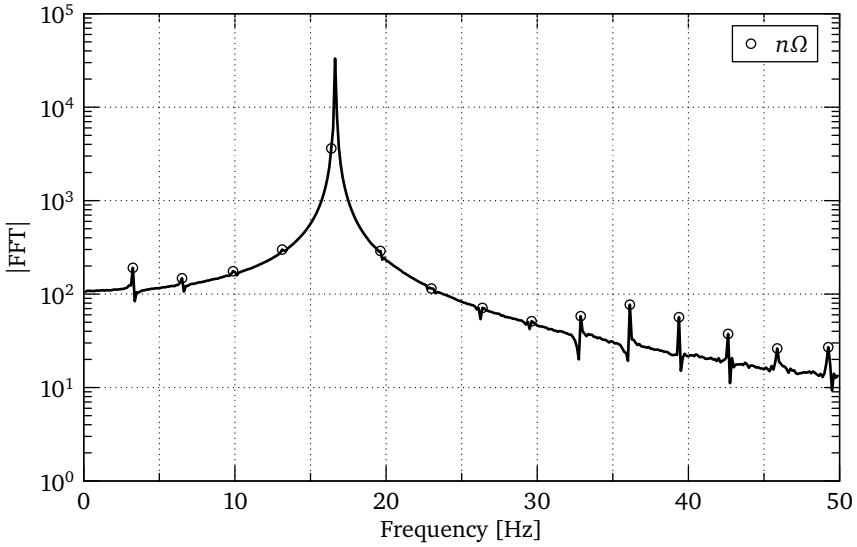

Figure 3.5. Frequency response for a test with m_2 and $\Omega = 3.28\,\mathrm{s}^{-1}$ ($196.8\,\mathrm{min}^{-1}$) illustrating the excitation related to the rotation velocity

Equation (3.6) can be written in matrix format

$$\begin{bmatrix} 1 & -4\pi^2 f_{n_0}^2 \\ 1 & -4\pi^2 f_{n_1}^2 \\ 1 & -4\pi^2 f_{n_2}^2 \end{bmatrix} \cdot \begin{bmatrix} k_e \\ m_e \end{bmatrix} = \begin{bmatrix} 4\pi^2 f_{n_0}^2 m_0 \\ 4\pi^2 f_{n_1}^2 m_1 \\ 4\pi^2 f_{n_2}^2 m_2 \end{bmatrix}. \tag{3.7}$$

This can be solved in a least-squares fashion by pre-multiplying the left and right sides of the equation with the transpose of the first matrix.

$$\begin{bmatrix} 3 & -4\pi^2 \Sigma f_{n_i}^2 \\ -4\pi^2 \Sigma f_{n_i} & 16\pi^4 \Sigma f_{n_i}^4 \end{bmatrix} \cdot \begin{bmatrix} k_e \\ m_e \end{bmatrix} = \begin{bmatrix} 4\pi^2 \Sigma f_{n_i}^2 m_j \\ -16\pi^4 \Sigma f_{n_i}^4 m_j \end{bmatrix} \tag{3.8}$$

Solving for m_e

$$m_e = \frac{(\Sigma f_{n_i}^2 m_i)(\Sigma f_{n_i}^2) - 3\Sigma f_{n_i}^4 m_i}{3\Sigma f_{n_i}^4 - (\Sigma f_{n_i}^2)^2} \tag{3.9}$$

The numerical values of $m_e = m_e(\Omega)$ in equation (3.9) were calculated at discrete values of $f_{n_i}(\Omega)$ and the result is depicted in figure 3.8. For numerical purposes equation (3.9) can be approximated with a polynomial.

$$\begin{aligned} m_e(\Omega) \approx {} & -7.587\,16\times10^{-7}\Omega^4 + 1.863\,02\times10^{-5}\Omega^3 \\ & + 2.228\,30\times10^{-4}\Omega^2 + 4.858\,02\times10^{-4}\Omega + 0.077\,526 \quad [\mathrm{kg}] \end{aligned} \tag{3.10}$$

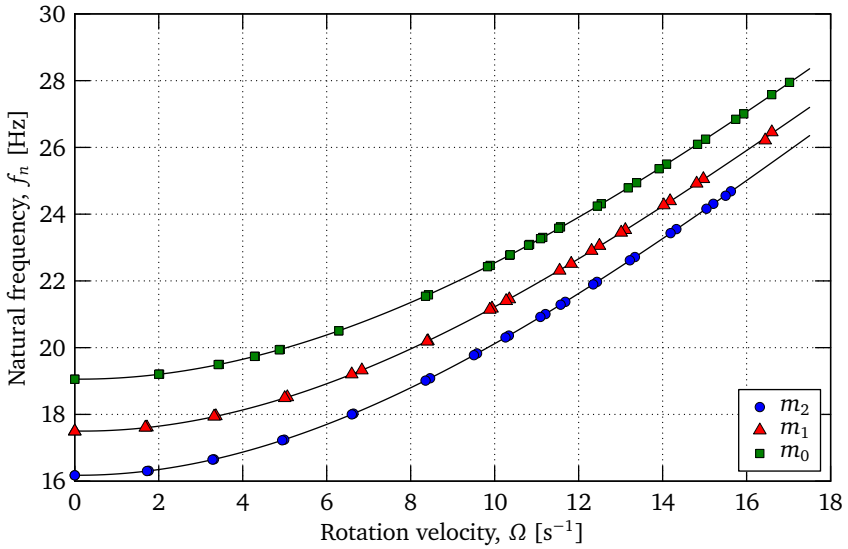

Figure 3.6. The natural frequency f_n of the first vibration mode of the beam in relation to the rotation velocity for different tip masses.

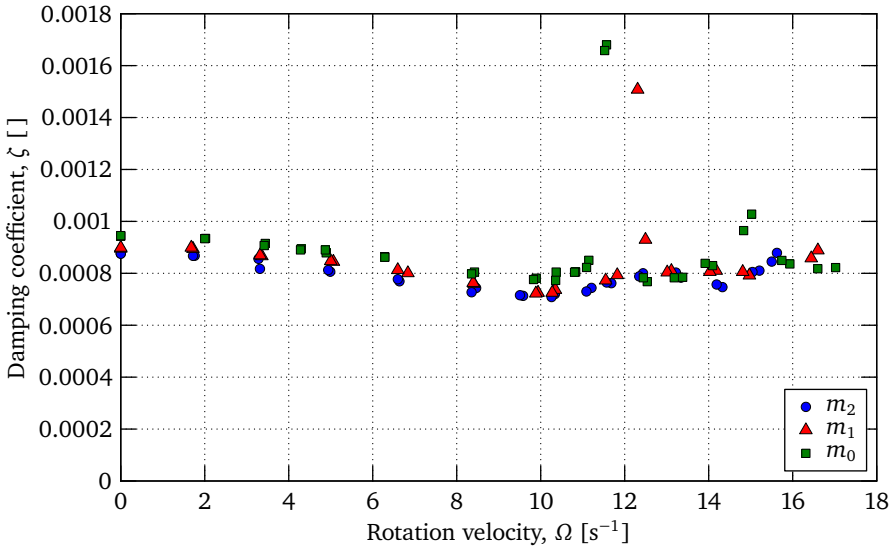

Figure 3.7. Damping coefficient, ζ of the beam in relation to rotation velocity for different tip masses.

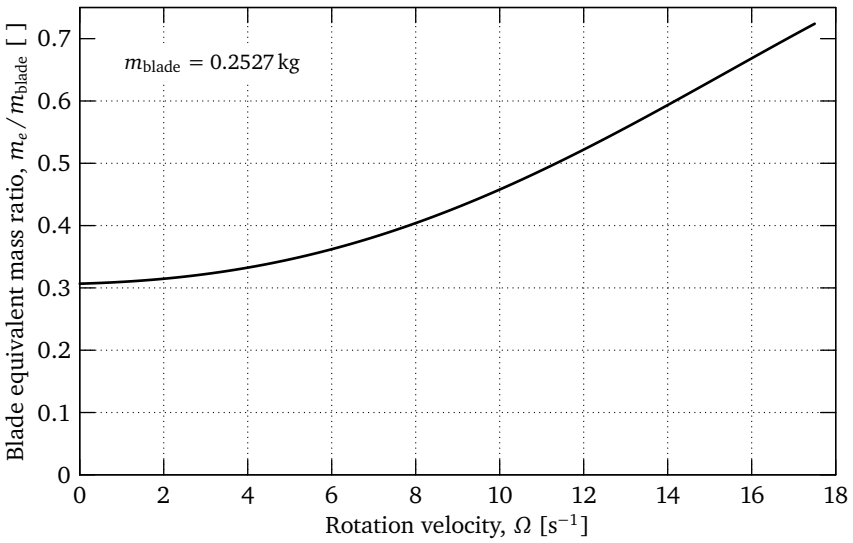

Figure 3.8. Equivalent beam mass ratio in relation to rotation velocity.

Equivalent stiffness and damping determination

We can now return to the test data and calculate the stiffness k_e and damping factor c_e. This is calculated at every measured data point j at rotation velocity Ω_j for the different tip masses m_i. The natural frequency $f_{n_{ij}}$, damping coefficient ζ_{ij} in figures 3.6 and 3.7 then give

$$k_{e_{ij}} = 4\pi^2 f_{n_{ij}}^2 \left[m_e(\Omega_j) + m_i \right], \tag{3.11}$$

$$c_{e_{ij}} = 4\pi \zeta_{ij} f_{n_{ij}} \left[m_e(\Omega_j) + m_i \right], \tag{3.12}$$

for $i = 0, 1, 2$ and $j = 0, \cdots, N$.

The results are depicted in figures 3.9 and 3.10 and can be approximated with the following polynomials

$$k_e(\Omega) \approx \quad 0.480\,77\Omega^3 + 6.283\,9\Omega^2 - 7.207\,1\Omega + 1\,046.1 \qquad [\text{N/m}] \tag{3.13}$$

$$\begin{aligned} c_e(\Omega) \approx & -9.173\,5\times10^{-7}\Omega^4 + 3.226\,3\times10^{-5}\Omega^3 \\ & - 1.886\,4\times10^{-4}\Omega^2 + 3.166\,2\times10^{-4}\Omega + 0.018\,0 \qquad [\text{N·s/m}] \end{aligned} \tag{3.14}$$

To verify the stiffness we can calculate the k for $\Omega = 0\,\text{s}^{-1}$ from simple cantilever beam equations. From figure 3.2

$$I_x = \tfrac{1}{2} w h^3 = 6.75\times10^{-11}\,\text{m}^4, \tag{3.15}$$

$$k = \frac{3EI_x}{L^3} = 1040\,\text{N/m}. \tag{3.16}$$

This value corresponds very well with equation (3.13) at $\Omega = 0\,\text{s}^{-1}$.

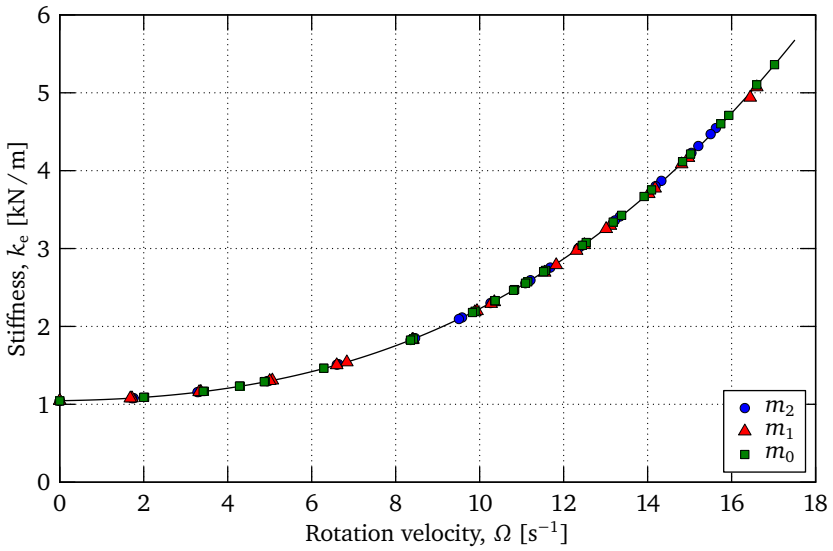

Figure 3.9. Equivalent beam stiffness, k_e, in relation to rotation velocity for different tip masses.

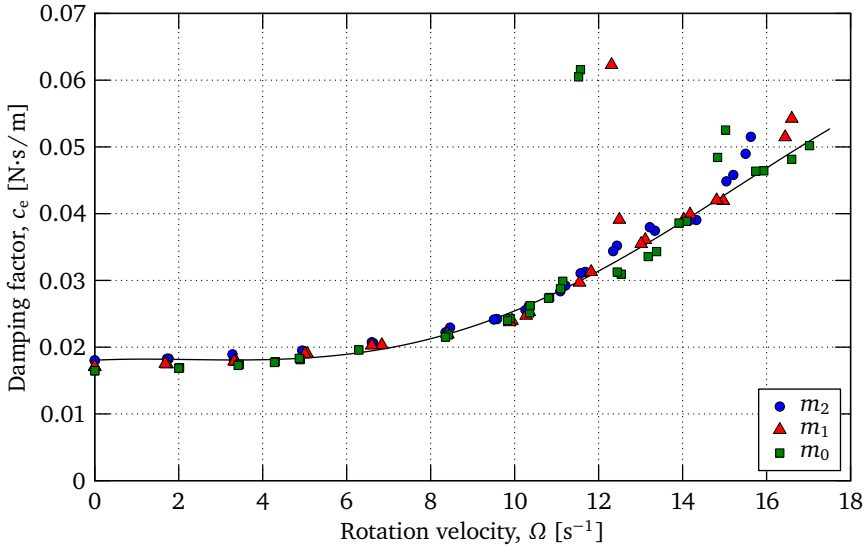

Figure 3.10. Equivalent beam damping factor, c_e, in relation to rotation velocity for different tip masses.

Chapter

4

Experimental Analysis of Particle Dampers

List of symbols for chapter 4

Constants

$g_0 = 9.81\,\mathrm{m/s^2}$	standard gravitational acceleration
$R = 0.4\,\mathrm{m}$	rotation radius

Variables

A	amplitude of oscillations	[m]
d_c	tip container cavity diameter	[m]
f_n	natural frequency, $f_n = \omega_n / (2\pi)$	[Hz]
h_c	tip container cavity height	[m]
i, j, ℓ	indices	
k	spring stiffness	[N/m]
m_c	container mass	[kg]
m_e	equivalent beam mass (eqn. 3.10)	[kg]
m_p	average total particle mass	[kg]
M_e	equivalent tip container mass (eqn. 4.2)	[kg]
r_m	mass ratio, $r_m = m_p / M_e$	[kg]
t	time	[s]
T	period of the damped motion	[s]
y	beam tip displacement	[m]
y^*	envelope of displacement	[m]
α	fraction of the particle contributing towards the total mass	[−]
δ_A	logarithmic decrement	[−]

δ_A^*	the linear slope of the exponential decay function in log space	$[\,s^{-1}\,]$
Γ	peak acceleration amplitude factor, $\Gamma{=}A\omega^2/g_0$	$[\,-\,]$
Γ_R	centrifugal acceleration factor, $\Gamma_R{=}R(2\pi\Omega)^2/g_0$	$[\,-\,]$
ϕ	oscillation phase angle (eqn. C.13)	[rad]
τ_i	times a zero crossings where $y(\tau_i)=0$	[s]
ω_n	natural frequency, $\omega_n=\sqrt{k/m}$	[rad/s]
Ω	system rotation velocity	$[\,s^{-1}\,]$
ζ	viscous damping factor, $\zeta=c/(2m\omega_n)$	$[\,-\,]$

4.1 Introduction

The main purpose of the experimental analysis of the particle dampers was to determine the effect of centrifugal loading on their performance. The damping performance constitutes two parameters, namely the damping coefficient and the minimum excitation acceleration where the damper is still active.

4.2 System parameters

The experiments were designed to eliminate as many system variations as possible. This was achieved by keeping the total tip mass as constant as possible for all the tests. The following configurations were used:

(a) Four tip containers with identical masses, but with different cavity heights were manufactured, see figure 4.1 and table 4.1.
(b) Three sizes of steel ball bearings, ⌀2 mm, ⌀3 mm and ⌀4 mm were used, see table 4.2. The number of balls selected were to give the same total tip mass (tip container mass plus ball mass) for all the tests. The total tip mass also corresponds with the tip mass used for calibration in section §3.2.

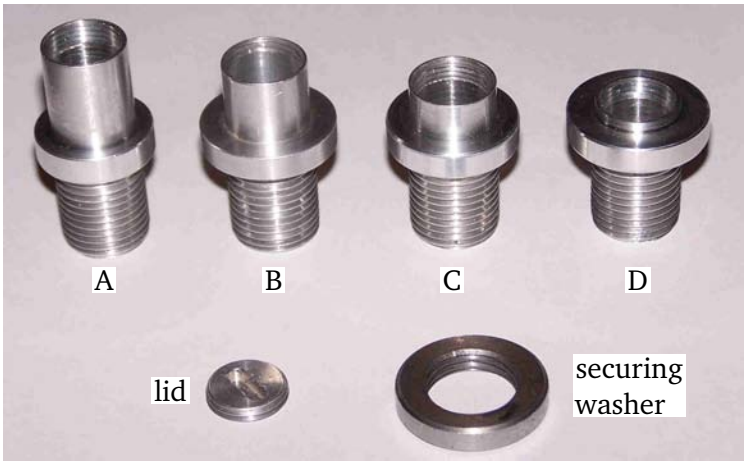

Figure 4.1. Set of four different containers used during damper tests

Table 4.1. Container parameters

Container	Cavity height h_c [mm]	Cavity diameter d_c [mm]	Empty mass[a] [kg]
A	37.0	12.5	21.52×10^{-3}
B	31.0	12.5	21.57×10^{-3}
C	25.3	12.5	21.54×10^{-3}
D	21.8	12.5	21.51×10^{-3}
		Average:	21.54×10^{-3}

[a] Includes mass of securing washer and lid, see figure 4.1.

Table 4.2. Ball parameters

Ball size[a]	Number of balls	Total mass [kg]
⌀2 mm	207	6.75×10^{-3}
⌀3 mm	62	6.73×10^{-3}
⌀4 mm	26	6.74×10^{-3}

[a] Standard stainless steel ball bearings.

The equivalent single degree of freedom (SDOF) properties of the beam were determined in section §3.3. The equivalent beam mass m_e in terms of the rotation velocity Ω (unit is s^{-1}) is

$$m_e = -7.587\,16\times10^{-7}\Omega^4 + 1.863\,02\times10^{-5}\Omega^3 + 2.228\,30\times10^{-4}\Omega^2 + 4.858\,02\times10^{-4}\Omega + 0.077\,526 \quad [\text{kg}] \quad (3.10)^*$$

The equivalent empty container mass M_e is the sum of the equivalent beam mass m_e and the average empty container mass m_c minus the mass of the hole in the beam. From equation (3.10), table 4.1 and figure 3.2

$$m_c = 0.021\,54\,\text{kg}, \quad (4.1)$$

$$M_e = m_e + m_c - 0.004\,77\,\text{kg} = m_e + 0.016\,77\,\text{kg}. \quad (4.2)$$

The average total particle mass from table 4.2 is $m_p = 6.74\times10^{-3}$ kg. The ratio r_m between the total particle mass and the equivalent SDOF container vibrating mass is defined as

$$r_m = m_p / M_e. \quad (4.3)$$

Figure 4.2 shows the numerical value of r_m.

The centrifugal load on the particles can be given in dimensionless form by the centrifugal acceleration factor

$$\Gamma_R = R(2\pi\Omega)^2 / g_0 \quad (4.4)$$

with $R = 0.4$ m the system rotation radius and Ω the system rotation velocity [s^{-1}].

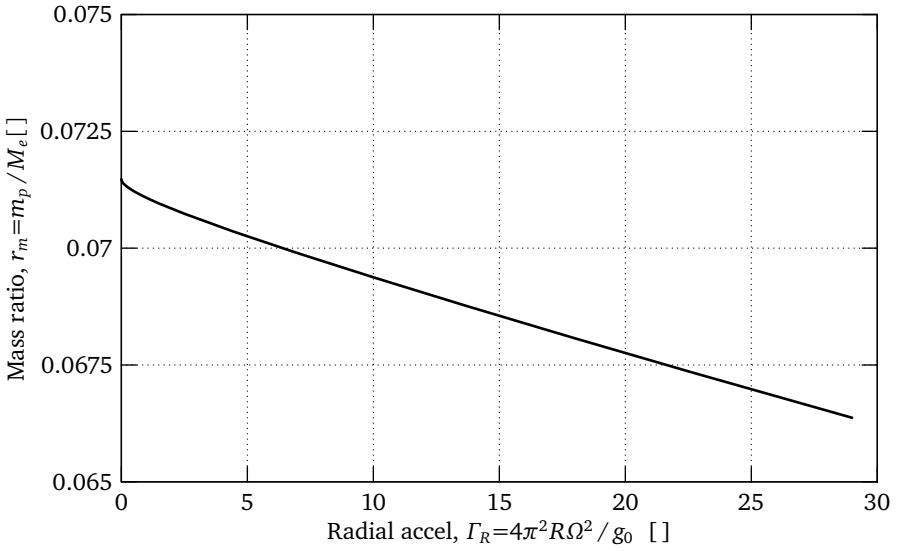

Figure 4.2. Ratio between particle mass and vibrating mass

4.3 Test procedure

A series of 12 tests, given in table 4.3, were conducted with four containers and three different ball sizes for each container. For each container/ball test, a range of tests were done with rotation velocities Ω between $0\,\mathrm{min}^{-1}$ and $1100\,\mathrm{min}^{-1}$. It was found that for $\Omega > 350\,\mathrm{min}^{-1}$ the particle damper has no influence.
During each test the following procedure were followed:

(a) The Wheatstone bridge for the strain gauges was zeroed.
(b) The test bench was spun up to the desired rotation velocity.
(c) After the velocity had stabilised and the vibration in the beam had damped out, the beam was activated.
(d) The strain gauge and velocity encoder outputs were recorded and stored.
(e) Two tests were conducted for every rotation velocity.

Table 4.3. Particle damper test matrix

	Containers			
	A	B	C	D
⌀2 mm	A2	B2	C2	D2
⌀3 mm	A3	B3	C3	D3
⌀4 mm	A4	B4	C4	D4

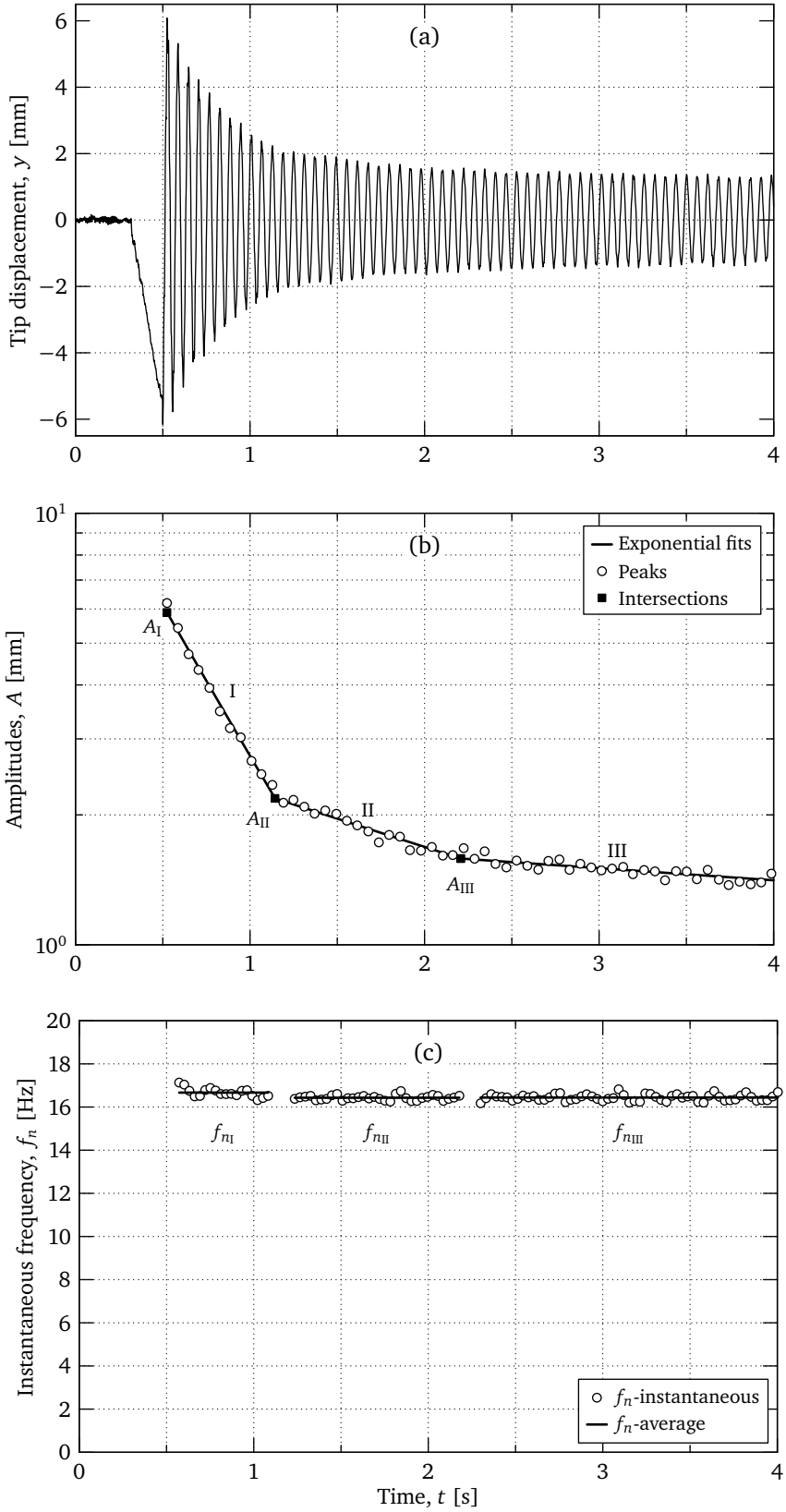

Figure 4.3. Example data for container A with ⌀4 mm balls and rotation velocity of $\Omega = 2.3\,\mathrm{s}^{-1}$. (a) Raw tip displacement data. (b) Peak amplitudes. (c) Instantaneous frequencies.

4.4 General observations

The tip displacement data was calculated from the strain gauge output using the same procedure as outlined in section §3.2. In figure 4.3(a) a typical output of the raw displacement data is shown.

Insight into the test data can be gained if we plot the vibration peaks on a log-scale graph as depicted in figure 4.3(b). It is clear that there are zones of exponential decay or viscous damping present. Zone I is the region of high damping. In zone II the damping is an order lower and in zone III we see no damping but the inherent damping of the beam itself. Amplitudes A_{I}, A_{II} and A_{III} give the displacement range of each zone. The initial displacement is $A_0 = A_{\mathrm{I}}$ and A_{III} is the minimum amplitude above which the particle damper (PD) still functions

One or both of zones I and II were present in all but a few of the tests. For no rotation ($\Omega = 0\,\mathrm{min}^{-1}$) we observed a few instances where the decay was not exponential but linear, suggesting friction damping. The results of those tests are not included in the overall analysis.

4.5 Data analysis

Based on the fact that the decay in motion is exponential we approximated the system as a SDOF mass-spring-damper system. The equation of motion for the free decay of an under damped system, $0 < \zeta < 1$, is given by

$$y(t) = A\,\mathrm{e}^{-\zeta\omega_n t}\cos\big(\sqrt{1-\zeta^2}\,\omega_n t - \phi\big). \tag{4.5}$$

The period T of the damped motion is

$$T = \frac{2\pi}{\omega_n\sqrt{1-\zeta^2}}. \tag{4.6}$$

Instantaneous frequency

Consider the i-th peak of the vibration displacement at time t_i at the local maximum, $\cos(\sqrt{1-\zeta^2}\,\omega_n t_i - \phi) = 1$, then

$$A_i = y(t_i) = A\,\mathrm{e}^{-\zeta\omega_n t_i}\,. \tag{4.7}$$

The ratio between two successive peaks is

$$\frac{A_i}{A_{i+1}} = \frac{y(t_i)}{y(t_i+T)} = \mathrm{e}^{2\pi\zeta/\sqrt{1-\zeta^2}} \tag{4.8}$$

or

$$\ln\frac{A_i}{A_{i+1}} = \ln A_i - \ln A_{i+1} = \frac{2\pi\zeta}{\sqrt{1-\zeta^2}} = \delta_A \tag{4.9}$$

with δ_A the logarithmic decrement of the peaks. The damping coefficient can be obtained from equation (4.9) in terms of the logarithmic decrement δ_A with

$$\zeta = \frac{\delta_A}{\sqrt{4\pi^2+\delta_A^2}}. \tag{4.10}$$

We can now return to figure 4.3(b). The time varying envelope of motion of equation (4.5) modulating the cosine function is given by

$$y^*(t) = A\,\mathrm{e}^{-\zeta\omega_n t}\,. \tag{4.11}$$

Equation (4.11) can be written in logarithmic format

$$\ln y^*(t) = \ln A - \zeta\omega_n t = \ln A - \delta_A^* t \tag{4.12}$$

with δ_A^* the linear slope of the exponential decay function in log space. The numerical value of δ_A^* can be obtained with a linear regression curve fit on the peak data against time in figure 4.3(b) for zones I, II or III.

For t_i the time at the i-th peak, is the decrement in peak values

$$\ln y^*(t_i) - \ln y^*(t_i + T) = \ln A_i - \ln A_{i+1} = \delta_A^* T. \tag{4.13}$$

It is clear from equations (4.9) and (4.13) that $\delta_A = \delta_A^* T = \omega_n \zeta T$. If we insert this result into equation (4.10) we obtain the frequency

$$\omega_n = \sqrt{\frac{4\pi^2}{T^2} - \delta_A^{*\,2}}. \tag{4.14}$$

From figure 4.3(a) we can search for the $N+1$ points where the signal crosses zero. Through interpolation we can obtain the times $t = \tau_j$ where $y(\tau_j) = 0$ for $j = 0, 1, \ldots, N$. The instantaneous period of the signal at time τ_ℓ is then defined as

$$T_\ell = \tau_{\ell+1} - \tau_{\ell-1}, \qquad \ell = 1, 2, \ldots, N-1 \tag{4.15}$$

The instantaneous vibration frequency at time τ_ℓ is then given by

$$\omega_n(\tau_\ell) = 2\pi f_n(\tau_\ell) = \sqrt{\frac{4\pi^2}{T_\ell^2} - \delta_A^{*\,2}}. \tag{4.16}$$

The result of the application of equation (4.16) on our example is shown in figure 4.3(c). It can be seen that the average frequency is about 1.4 % higher in zone I compared to zones II and III.

As an alternative, an analysis of the instantaneous vibration frequency of our example was conducted with the Hilbert vibration decomposition (HVD) method[3] (Feldman, 2006). The result of the first mono-component signals (see section §2.4 for a detailed discussion of terminology) is depicted in figure 4.4. The mono-component signal c_1 is the largest displacement and describes the overall motion of the system with the highest energy. The lower energy mono-component signals c_2, c_3, etc. (not shown in graph) have much smaller amplitudes; maximum amplitude of c_2 is 0.2 mm and for c_3 it is 0.02 mm and can be attributed to measurement noise.

It is clear from figure 4.4 that the instantaneous vibration frequency is higher in zone I, confirming our previous observation. Note that the frequency decreases

[3]The Hilbert vibration decomposition software was obtained in binary format from the authors web page: `http://hitech.technion.ac.il/~feldman` (2008-11-05). The software and its internal algorithms are undocumented. It is only used here for comparative purposes.

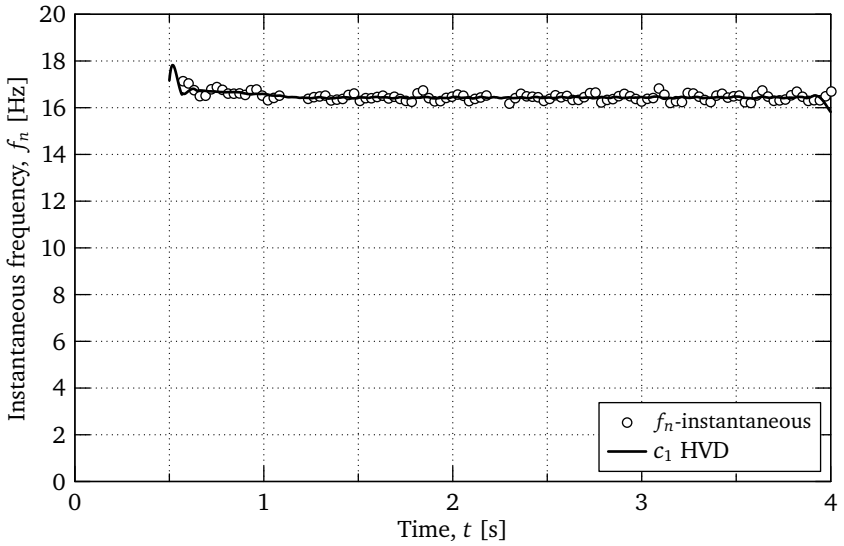

Figure 4.4. Instantaneous frequency for container A with ∅4 mm balls and rotation velocity of $\Omega = 2.3\,\mathrm{s}^{-1}$ calculated with the HVD method from Feldman (2006).

throughout zone I and that the average frequency we use later on in equation (4.17) is an approximation.

Viscous damping coefficient

The average frequency in zones I, II or III is defined as

$$\bar{\omega}_n = \frac{1}{N-1} \sum_{k=1}^{N-1} \omega_n(\tau_k). \tag{4.17}$$

The result is shown by the solid lines in figure 4.3(c) for our example. The viscous damping coefficient ζ for each zone can then be calculated from

$$\zeta = \frac{\delta_A^*}{\bar{\omega}_n} \tag{4.18}$$

with δ_A^* the linear slope of the exponential decay function in log space.

Effective mass

The natural frequency of a SDOF mass-spring system is $\omega_n^2 = k/m$ with k the stiffness of the spring and m the mass of the system.

$$\omega_n^2 = \frac{k}{M_e + \alpha m_p} \tag{4.19}$$

with M_e the effective mass of the beam and container, m_p the mass of the particles and α the fraction of the particles contributing towards the total mass of the system in zone I, II or III.

If we assume that the stiffness of the spring and the effective mass are constant, then for the frequency to change, the contribution of the particle towards the mass

of the vibrating system must be variable. In zone III there is no particle damping and can we assume that the full mass of particles is part of the total mass of the vibrating system.

$$\left(\frac{\bar{\omega}_{n_{\mathrm{III}}}}{\bar{\omega}_{n_{\mathrm{I}}}}\right)^2 = \frac{M_e + \alpha_{\mathrm{I}} m_p}{M_e + m_p} = \frac{1 + \alpha_{\mathrm{I}} r_m}{1 + r_m} \tag{4.20}$$

or

$$\alpha_{\mathrm{I}} = \frac{1}{r_m}\left[\left(\frac{\bar{\omega}_{n_{\mathrm{I}}}}{\bar{\omega}_{n_{\mathrm{III}}}}\right)^2 (1 + r_m) - 1\right] \tag{4.21}$$

The range of the effective mass factor α_{I} is $0 \leq \alpha_{\mathrm{I}} \leq 1$. When $\alpha_{\mathrm{I}} \to 0$ it means that the system is highly excited and that the particles contribute very little towards the system mass (see figure 2.2 on page 16). If α_{I}=1 then the particles move as a solid unit together with the container.

4.6 Test results

The test data have been analysed as discussed in the preceding sections and an example is shown in figure 4.5 for the results of one test series. The full set of results is given in figures A.1 to A.12 on pages 77–88. For every test series we show the following results:

(a) The change in the operational envelope of the particle damper in terms of the peak vibration acceleration amplitude in relation to the centrifugal acceleration factor Γ_R. The peak acceleration amplitude factor in dimensionless form is defined as

$$\Gamma = \frac{A\omega_n^2}{g_0} \tag{4.22}$$

with ω_n the vibration frequency, A the vibration amplitude and $g_0 = 9.81\,\mathrm{m/s^2}$ the gravitational acceleration.

(b) The change of the damping coefficient ζ for zones I and II in relation to the centrifugal acceleration factor Γ_R.

(c) The change in the effective mass factor α_{I} in relation to the centrifugal acceleration factor Γ_R. This is an indication of the excitation state of the particles or the relative motion between the particles and the container.

Further data analysis and an in depth look at the data is conducted in chapter 6.

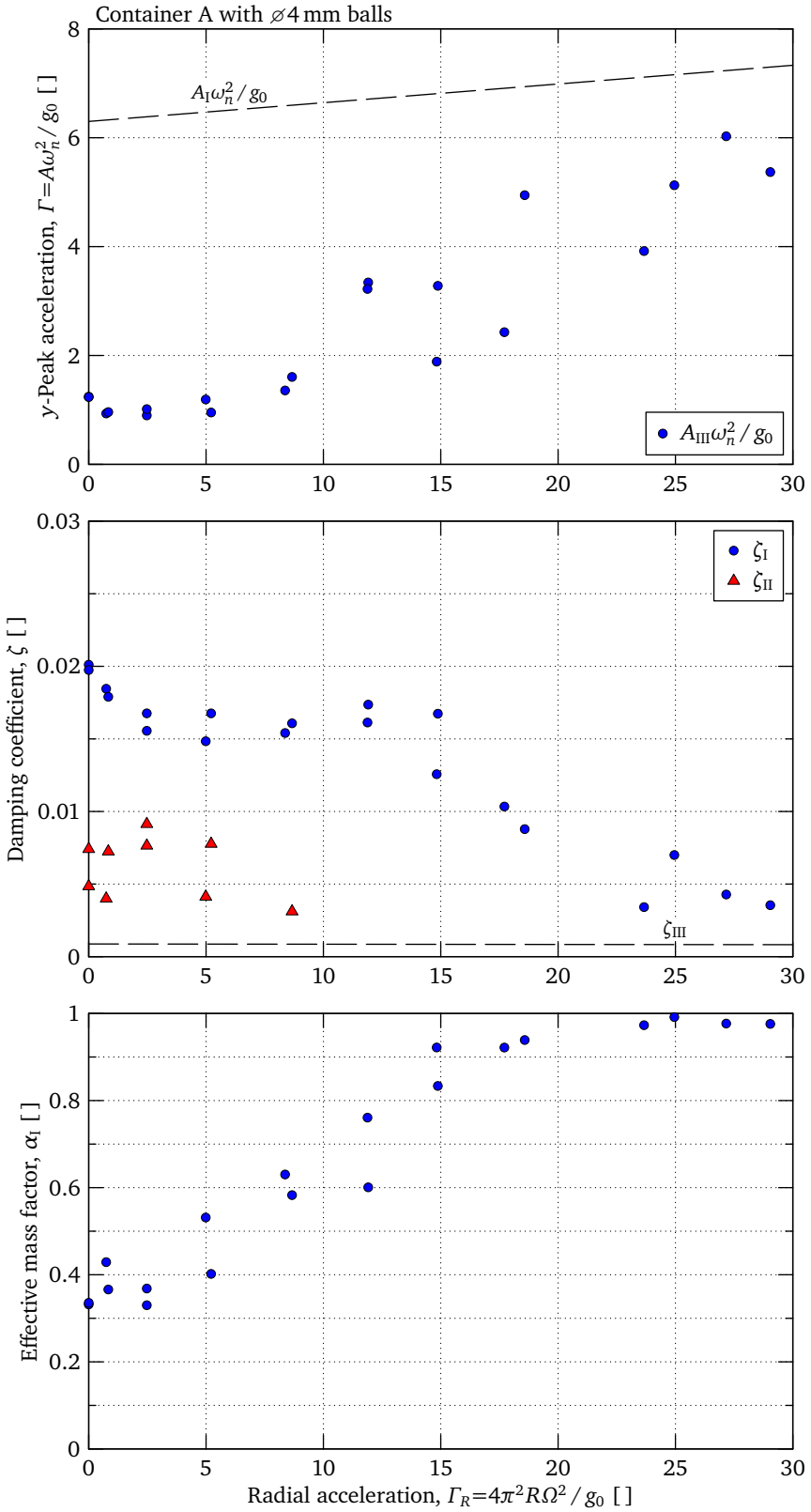

Figure 4.5. Example of test data (container A with ⌀4 mm balls)

Chapter

5

DEM Analysis of Particle Dampers

List of symbols for chapter 5

Constants

$g_0 = 9.81\,\mathrm{m/s^2}$	standard gravitational acceleration
$R = 0.4\,\mathrm{m}$	rotation radius

Variables

A	amplitude of oscillations	[m]
c	damping coefficient	[N·s / m]
c_{crit}	PFC3D critical damping coefficient (eqn. 5.18)	[N·s / m]
c_e	equivalent beam damping coefficient (eqn. 3.14)	[N·s / m]
E	modulus of elasticity (Young's modulus)	[Pa]
F_y	ball-container contact force in y-direction	[N]
F_n	normal contact force, $F_n = F_{nk} + F_{nc}$	[N]
F_{nk}	normal contact elastic force (eqn. 5.5)	[N]
F_{nc}	normal contact damping force	[N]
g_x	centrifugal acceleration, $g_x = 4\pi^2 R\Omega^2$ (eqn. 5.1a)	[$\mathrm{m/s^2}$]
g_y	gravitational acceleration, $g_y = -g_0$ (eqn. 5.1b)	[$\mathrm{m/s^2}$]
G	modulus of rigidity (shear modulus)	[Pa]
$\bar{G}$	PFC3D average modulus of rigidity (eqn. 5.8)	[Pa]
h_c	container height (tab. 5.1)	[m]
i, j	indices	
k_e	equivalent beam stiffness (eqn. 3.13)	[N / m]
$\tilde{k}_{\mathrm{H}}$	Hertz normal stiffness coefficient (eqn. E.17)	[$\mathrm{N/m^{3/2}}$]
k_n'	PFC3D contact tangential stiffness, (eqn. 5.19)	[N / m]
$\bar{k}_n$	PFC3D Hertz normal stiffness coefficient (eqn. 5.5)	[$\mathrm{N/m^{3/2}}$]

$\bar{k}_s$	PFC3D Hertz shear stiffness coefficient (eqn. 5.10)	$[\,\mathrm{N/m^{3/2}}\,]$
m_c	container mass	$[\,\mathrm{kg}\,]$
m_e	equivalent beam mass (eqn. 3.10)	$[\,\mathrm{kg}\,]$
m_p	average total particle mass	$[\,\mathrm{kg}\,]$
M_e	equivalent tip container mass (eqn. 4.2)	$[\,\mathrm{kg}\,]$
r_m	mass ratio, $r_m = m_p / M_e$	$[\,\mathrm{kg}\,]$
r	ball radius	$[\,\mathrm{m}\,]$
$\bar{R}$	PFC3D average radius (eqn. 5.7)	$[\,\mathrm{m}\,]$
R_c	container radius (tab. 5.1)	$[\,\mathrm{m}\,]$
t	time	$[\,\mathrm{s}\,]$
Δt	integration time step	$[\,\mathrm{s}\,]$
x, y	coordinate	$[\,\mathrm{m}\,]$
y_c	container y-coordinate	$[\,\mathrm{m}\,]$
$\dot{y}_c$	container y-velocity	$[\,\mathrm{m/s}\,]$
$\ddot{y}_c$	container y-acceleration	$[\,\mathrm{m/s^2}\,]$
Δy_{c0}	beam tip initial displacement	$[\,\mathrm{m}\,]$
α	fraction of the particle contributing towards the total mass	$[\,-\,]$
α_m	particle mass ration, $\alpha_m = m_j / m_i$	$[\,-\,]$
δ	ball contact overlap	$[\,\mathrm{m}\,]$
$\dot{\delta}$	ball contact velocity	$[\,\mathrm{m/s}\,]$
$\dot{\delta}_{\mathrm{in}}$	ball impact velocity	$[\,\mathrm{m/s}\,]$
δ_s	shear displacement	$[\,\mathrm{m}\,]$
ϵ	coefficient of restitution	$[\,\mathrm{m}\,]$
γ	real number characterising viscoelastic forces (eqn. 5.11)	$[\,-\,]$
Γ	peak acceleration amplitude factor, $\Gamma = A\omega^2 / g_0$	$[\,-\,]$
Γ_R	centrifugal acceleration factor, $\Gamma_R = R(2\pi\Omega)^2 / g_0$	$[\,-\,]$
μ	friction coefficient	$[\,-\,]$
ν	Poison's ratio	$[\,-\,]$
$\bar{\nu}$	PFC3D average Poison's ratio (eqn. 5.9)	$[\,-\,]$
ρ	ball density (tab. 5.2)	$[\,\mathrm{kg/m^3}\,]$
ω_n	natural frequency, $\omega_n = \sqrt{k/m}$	$[\,\mathrm{rad/s}\,]$
Ω	system rotation velocity	$[\,\mathrm{s^{-1}}\,]$
ζ	viscous damping factor, $\zeta = c / (2m\omega_n)$	$[\,-\,]$

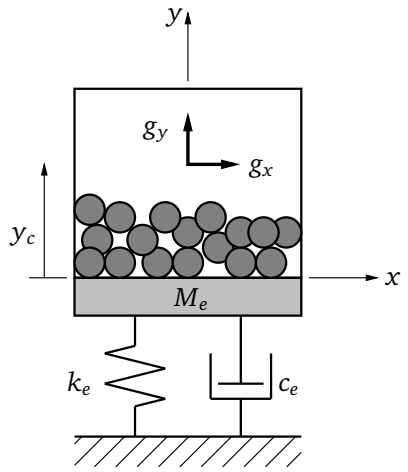

Figure 5.1. Equivalent SDOF mass-spring-damper system for a rotating beam with tip container

5.1 Introduction

The discrete element method (DEM) simulations of the particle damper (PD) were performed, firstly to investigate the ability of the simulation models to duplicate the physical experiments in chapter 4, and secondly to extrapolate the experimental results for more detailed investigations of the PD performance. The DEM simulations also makes it possible to conduct numerical experiments that are difficult or impossible to do with physical experiments, such as the effect of inter particle friction or the effect of energy dissipation between particles. The specific software used for the simulations was the commercial DEM program PFC3D version 3.0 (see PFC3D User's Guide).

5.2 Container model

For the DEM modelling of the rotating beam with a PD, we simplify the beam-container system as a single degree of freedom (SDOF) mass-spring damper system to a container filled with spherical balls. Figure 5.1 is a schematic depiction of the DEM model.

The container itself was modelled as a cylinder (a build-in type in PFC3D) with flat planes at both ends. The dimensions of the cylinders are listed in table 5.1. The container material is aluminium with elastic properties from Budynas and Nisbett (2008), table A-5:

Modulus of elasticity: $E = 72\,\text{GPa}$,
Poison's ratio: $\nu = 0.3333$

Note that these values are not used in PFC3D for Hertz contacts, but are listed for the calculations in table 5.3.

Table 5.1. PFC3D cylindrical container parameters

Container	Cylinder height h_c [mm]	Cylinder radius R_c [mm]
A	37.0	6.25
B	31.0	6.25
C	25.3	6.25
D	21.8	6.25

5.2.1 Equivalent beam parameters

The equivalent SDOF properties of the rotating beam were determined in section §3.3. The equivalent beam mass m_e, stiffness k_e and damping coefficient c_e in terms of the rotation velocity Ω (unit in s^{-1}) are

$$m_e = -7.587\,16\times10^{-7}\Omega^4 + 1.863\,02\times10^{-5}\Omega^3 + 2.228\,30\times10^{-4}\Omega^2 + 4.858\,02\times10^{-4}\Omega + 0.077\,526 \quad [\text{kg}] \quad (3.10)^*$$

$$k_e = 0.480\,77\Omega^3 + 6.2839\Omega^2 - 7.2071\Omega + 1046.1 \quad [\text{N/m}] \quad (3.13)^*$$

$$c_e = -9.1735\times10^{-7}\Omega^4 + 3.2263\times10^{-5}\Omega^3 - 1.8864\times10^{-4}\Omega^2 + 3.1662\times10^{-4}\Omega + 0.0180 \quad [\text{N·s/m}] \quad (3.14)^*$$

The equivalent empty container mass M_e is the sum of the equivalent beam mass m_e and the average empty container mass m_c minus the mass of the hole in the beam

$$m_c = 0.021\,54\,\text{kg}, \quad (4.1)^*$$

$$M_e = m_e + m_c - 0.004\,77\,\text{kg} = m_e + 0.016\,77\,\text{kg}. \quad (4.2)^*$$

5.2.2 Container equations of motion

The body forces on the balls inside the tip container due to gravitational and centrifugal forces are

$$g_x = 4\pi^2 R\Omega^2, \quad (5.1a)$$

$$g_y = -g_0, \quad (5.1b)$$

with R the tip container rotation radius and Ω the rotation velocity.

The x-position of the container is fixed. The equation of motion of the tip container in the y-direction is

$$\ddot{y}_c = -\frac{k_e}{M_e}y_c - \frac{c_e}{M_e}\dot{y}_c + \frac{\Sigma F_y}{M_e} + g_y. \quad (5.2)$$

with ΣF_y the total sum of all the contact forces in the y-direction between the balls and the container. Equation (5.2) was implemented in the DEM software by

adjusting the container velocity after each system integration step. The increment in container velocity is

$$\Delta \dot{y}_c = \ddot{y}_c \, \Delta t \tag{5.3}$$

with Δt the current integration time step. Note that the updated container position y_c is automatically calculated as part of the normal DEM integration step.

5.3 Particle contact parameters

In PFC3D we have a choice between a linear approximated contact model and the non-linear Hertz contact model. If we assume that there is no plastic deformation between the balls and between the balls and the walls then the Hertz contact model describes experimental observations the best.

The Hertz contact model was selected for our DEM simulations. The next sections give an overview of the PFC3D implementations of the contact model. The PFC3D version 3.0 User's Guide does not give all the implementation details and some of the formulations were obtained through numerical tests. These were later confirmed by Itasca's technical personnel (Emam, 2008).

5.3.1 Hertz normal elastic contact model

The Hertz normal contact force model employed in PFC3D is a nonlinear formulation based on the theory described in appendix E. For ball-ball contact PFC3D uses a simplified version of the material properties. For ball-wall contacts the wall is replaced, for numerical purposes, with an identical ball positioned symmetrically about the wall position. The overlap δ is set equal to twice the physical ball-wall overlap. A wall is also assumed to be rigid with infinite stiffness. A ball-cylinder contact is treated the same as a ball-wall contact.

The normal contact force, shown in figure 5.2(a), consists of an elastic and a damping component

$$F_n = F_{nk} + F_{nc}. \tag{5.4}$$

The non-linear Hertz elastic force component is given by

$$F_{nk} = \begin{cases} \bar{k}_n \, \delta^{3/2} & \text{ball-ball contact} \\ \bar{k}_n \, (2\delta)^{3/2} & \text{ball-wall contact} \end{cases} \tag{5.5}$$

with the PFC3D approximated Hertz normal coefficient

$$\bar{k}_n = \frac{2\bar{G}}{3(1-\bar{\nu})} \sqrt{2\bar{R}}. \tag{5.6}$$

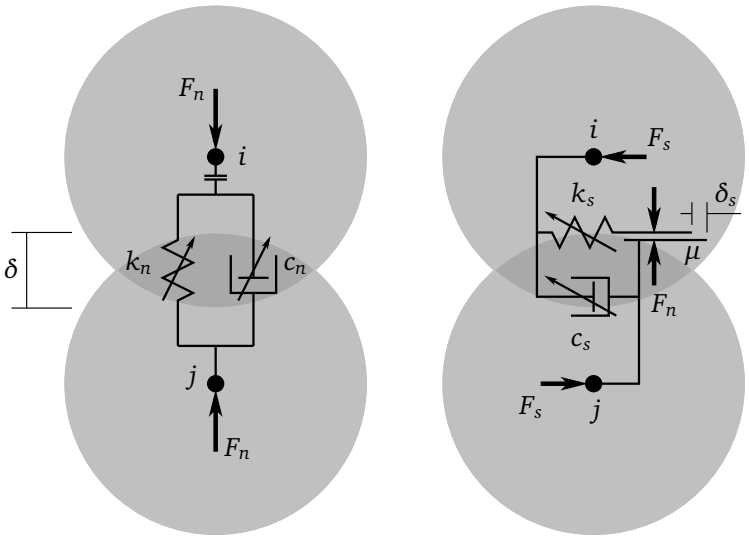

Figure 5.2. DEM normal and shear contact parameters

The geometric and material parameters are

$$\bar{R} = \begin{cases} \dfrac{2r_i r_j}{r_i + r_j} & \text{ball-ball contact} \\ r_i & \text{ball-wall contact} \end{cases} \tag{5.7}$$

$$\bar{G} = \begin{cases} \frac{1}{2}(G_i + G_j) & \text{ball-ball contact} \\ G_i & \text{ball-wall contact} \end{cases} \tag{5.8}$$

$$\bar{\nu} = \begin{cases} \frac{1}{2}(\nu_i + \nu_j) & \text{ball-ball contact} \\ \nu_i & \text{ball-wall contact} \end{cases} \tag{5.9}$$

with G_i, G_j the modulus of rigidity, ν_i, ν_j Poison's ratio of the two bodies in contact and r_i, r_j the respective contact radii. The modulus of elasticity in terms of the modulus of rigidity is $E = 2(1 + \nu)G$. The list of input parameters for the PFC3D simulations are given in table 5.2.

In table 5.3 we investigate the difference between the PFC3D approximation of Hertz contacts and the theoretically correct values from appendix E. The PFC3D average materials property $\bar{G}$ gives identical values to the Hertz parameter $\tilde{E}$ from equation (E.12) for ball-ball contacts with similar properties, but makes a substantial error with the assumption of a rigid wall for ball-wall and ball-cylinder contacts. For ball-ball contact between balls with identical material properties, $\bar{k}_n = \tilde{k}_{\mathrm{H}}$ with $\tilde{k}_{\mathrm{H}}$ the Hertz contact coefficient given by equation (E.17). For ball-wall and ball-cylinder contact the error is between 15 % and 27 %.

Table 5.2. PFC3D Hertz contact ball parameters

Ball size	Ball radii r_i [m]	Modulus of rigidity[a] G [Pa]	Poison's ratio[a] ν [−]	Ball density[b] ρ [kg / m^3]	Number of balls
⌀2 mm	1.0×10^{-3}	73.1×10^{9}	0.305	7779	207
⌀3 mm	1.5×10^{-3}	73.1×10^{9}	0.305	7676	62
⌀4 mm	2.0×10^{-3}	73.1×10^{9}	0.305	7734	26

NOTE: Standard stainless steel ball bearings.

[a] Properties from Budynas and Nisbett (2008).

[b] Calculated from table 4.2 on page 35.

Table 5.3. Comparison between the PFC3D and theoretically correct Hertz normal contact parameters

		PFC3D[a]		Hertz[b]		
		$\frac{\bar{G}}{1-\bar{\nu}}$	$\frac{F_{nk}}{\sqrt{r_i}\,\delta^{3/2}}$	$\tilde{E}$	$\frac{\tilde{k}_{\mathrm{H}}}{\sqrt{r_i}}$	
		[GPa]	[GPa]	[GPa]	[GPa]	Error
Ball-ball[c]		104.7	98.8	104.7	98.8	0 %
Ball-wall		104.7	98.8	58.4	77.9	27 %
Ball-cylinder[d]	⌀2 mm	104.7	98.8	58.4	81.4	21 %
	⌀3 mm	104.7	98.8	58.4	83.5	18 %
	⌀4 mm	104.7	98.8	58.4	86.0	15 %

[a] Formulae for PFC3D from equations (5.5) to (5.9).

[b] Formulae for Hertz contacts from equations (E.18) to (E.23).

[c] Ball-ball calculations for uniform sized balls ($\bar{R} = r_i$ and $\tilde{R} = r_i/2$).

[d] Cylindrical contact corrections from table E.1.

5.3.2 Mindlin shear contacts

In PFC3D a non-linear incremental friction model by Cundall and Strack (1979) is used. The model is based on an approximation of the Mindlin and Deresiewicz (1953) theory. The basic mechanism is shown in figure 5.2(b). It consists of a non-linear spring, with stiffness $\bar{k}_s$, and a slip surface, with friction coefficient μ. The forces are displacement driven and depend on the history of the shear displacement δ_s, the distance that the spring is compressed or extended, and the normal force F_n at that moment. It is zeroed every time contact is established or lost.

The approximated Mindlin non-linear shear stiffness in PFC3D is given by

$$\bar{k}_s = \frac{2\left[3\bar{G}^2(1-\bar{\nu}\bar{R})\right]^{1/3}}{2-\bar{\nu}} F_n^{1/3}. \tag{5.10}$$

The friction coefficient μ between the balls and between the ball and walls were obtained through model calibration and are listed in section §5.4.2.

5.3.3 Hertz contacts with viscoelastic damping

General coefficient of restitution

The general Hertz equation of damped motion of a ball with mass m in contact with a massive body in the absence of gravity is given by

$$m\,\ddot{\delta} = -\tilde{k}_{\mathrm{H}}\,\delta^{3/2} - c\,\dot{\delta}\,\delta^{\gamma}. \tag{5.11}$$

where γ is a real number characterising the linear ($\gamma = 0$) or nonlinear ($\gamma \neq 0$) nature of the viscoelastic force, and c is a damping dissipation coefficient. Falcon (1997) presented an analytic approximation for the normal coefficient of restitution (COR)

$$\epsilon = \left|\frac{\dot{\delta}_{\mathrm{out}}}{\dot{\delta}_{\mathrm{in}}}\right| = \sqrt{1 - \frac{8}{5}\,\mathcal{B}\Big(\frac{3}{2},\,\frac{2\gamma+2}{5}\Big)\beta} \tag{5.12}$$

with $\dot{\delta}_{\mathrm{in}} = \dot{\delta}|_{\delta=0}$ the impact velocity, $\dot{\delta}_{\mathrm{out}}$ the rebound velocity. The Beta function $\mathcal{B}(m,n)$ is given by

$$\mathcal{B}(m,n) = \int_0^1 \tau^{m-1}(1-\tau)^{n-1}\,d\tau = \frac{\Gamma(m)\,\Gamma(n)}{\Gamma(m+n)} \qquad m>0, \quad n>0 \tag{5.13}$$

and

$$\beta = \frac{c}{m}\left(\frac{5m}{4\tilde{k}_{\mathrm{H}}}\right)^{(2\gamma+2)/5} \dot{\delta}_{\mathrm{in}}^{(4\gamma-1)/5} \tag{5.14}$$

Equation (5.12) can be approximated with the first terms of a binomial series

$$\epsilon \approx 1 - \frac{4}{5}\,\mathcal{B}\Big(\frac{3}{2},\,\frac{2\gamma+2}{5}\Big)\beta. \tag{5.15}$$

Various values for γ are found in the literature. Detailed overviews of the different models are given by Schäfer *et al.* (1996) and Stevens and Hrenya (2005).

A linear dashpot is obtained when γ=0. This model does not correspond with any experimental observations, but is nevertheless frequently used.

$$\gamma = 0 \qquad \epsilon \approx 1 - 1.635\,\frac{c}{m}\left(\frac{5m}{4\tilde{k}_{\mathrm{H}}}\right)^{2/5}\dot{\delta}_{\mathrm{in}}^{-1/5} \tag{5.16a}$$

If the material dissipates energy internally in a viscous fashion then $\gamma=\frac{1}{2}$ (Kuwabara and Kono, 1987; Brilliantov *et al.*, 1996). Various experimental results indicate that this model describes impacts with elastic deformation

$$very well.\gamma = 1/2 \quad \epsilon \approx 1 - 1.009\,\frac{c}{m}\left(\frac{5m}{4\tilde{k}_{\mathrm{H}}}\right)^{3/5}\dot{\delta}_{\mathrm{in}}^{1/5} \tag{5.16b}$$

Another popular model is the semi-viscoelastic model with $\gamma=\frac{1}{4}$ that results in a constant coefficient of restitution that can be used for low dissipation elastic impacts.

$$\gamma = 1/4 \quad \epsilon \approx 1 - \frac{2\pi}{5}\,\frac{c}{m}\left(\frac{5m}{4\tilde{k}_{\mathrm{H}}}\right)^{1/2}\dot{\delta}_{\mathrm{in}}^{0} = 1 - \frac{\pi c}{\sqrt{5m\tilde{k}_{\mathrm{H}}}} \tag{5.16c}$$

PFC3D damping implementation

In PFC3D the viscous damping force in the normal direction is given by

$$F_{nc} = -\zeta\, c_{\mathrm{crit}}\dot{\delta} \tag{5.17}$$

with ζ the critical damping ratio. The critical damping constant is defined as

$$c_{\mathrm{crit}} = 2\sqrt{\bar{m}k_n'}. \tag{5.18}$$

The contact tangential stiffness is defined as[4]

$$k_n' = \frac{\mathrm{d}F_{nk}}{\mathrm{d}\delta} = \frac{3}{2}\bar{k}_n\,\delta^{1/2} \tag{5.19}$$

and the mass factor

$$\bar{m} = \begin{cases} \dfrac{m_i m_j}{m_i + m_j} & \text{ball-ball contact} \\ m_i & \text{ball-wall contact} \end{cases} \tag{5.20}$$

Ball-ball contacts: Let $m_j = \alpha_m m_i$ then

$$\bar{m} = \frac{\alpha_m}{1+\alpha_m}\,m_i \quad \text{and} \quad \alpha_m = m_j/m_i. \tag{5.21}$$

[4]In PFC3D the force equation for ball-ball contacts is used and not the more general formulation of equation (5.5).

If we fix m_j, the equation of motion of particle m_i is

$$\begin{aligned} m_i\ddot{\delta} &= -\bar{k}_n\delta^{3/2} - \zeta\, c_{\text{crit}}\,\dot{\delta}, \\ &= -\bar{k}_n\delta^{3/2} - \zeta\sqrt{\frac{6\alpha_m}{1+\alpha_m}\, m_i\bar{k}_n}\;\dot{\delta}\;\delta^{1/4}. \end{aligned} \tag{5.22}$$

Comparing equation (5.22) to (5.11) indicates that the PFC3D viscous damping model for Hertz contacts is in fact a semi-viscoelastic model with $\gamma = \frac{1}{4}$ and $c = c_{\text{BB}}$ with

$$c_{\text{BB}} = \zeta\sqrt{\frac{6\alpha_m}{1+\alpha_m}\, m_i\bar{k}_n}. \tag{5.23}$$

The COR for ball-ball contacts from equation (5.16c) is then given by

$$\epsilon_{\text{BB}} \approx 1 - \pi\zeta\sqrt{\frac{6\alpha_m}{5(1+\alpha_m)}}. \tag{5.24}$$

Equation (5.24) is useful if we consider uniform sized particles with $\alpha_m = 1$. The COR is then $\epsilon_{\text{BB}}{\approx}1 - \pi\zeta\sqrt{3/5}$ and the critical damping factor can be determined from

$$\zeta_{\text{BB}} \approx \frac{1-\epsilon_{\text{BB}}}{\pi}\sqrt{\frac{5}{3}}\,. \tag{5.25}$$

Ball-wall contacts: For ball-wall contacts $\bar{m} = m_i$. If we fix the wall, the equation of motion of particle m_i is

$$\begin{aligned} m_i\ddot{\delta} &= -\bar{k}_n(2\delta)^{3/2} - \zeta\, c_{\text{crit}}\,\dot{\delta}, \\ &= -\bar{k}_n(2\delta)^{3/2} - 2\zeta\sqrt{\frac{3}{2}\, m_i\bar{k}_n(2\delta)^{1/2}}\;\dot{\delta} \\ &= -2^{3/2}\,\bar{k}_n\delta^{3/2} - \zeta\sqrt{3\,(2^{3/2})\, m_i\bar{k}_n}\;\dot{\delta}\;\delta^{1/4}. \end{aligned} \tag{5.26}$$

The COR for ball-wall contacts from equation (5.16c) is then given by

$$\epsilon_{\text{BW}} \approx 1 - \pi\zeta\sqrt{\frac{3}{5}}. \tag{5.27}$$

and the critical damping factor for ball-wall contacts

$$\zeta_{\text{BW}} \approx \frac{1-\epsilon_{\text{BW}}}{\pi}\sqrt{\frac{5}{3}}\,. \tag{5.28}$$

Equations (5.25) and (5.28) were tested[5] in PFC3D by impacting a single particle on a fixed particle or wall and it was found that the impact velocity does not influence the COR, and that both equations describe the COR very well. It must be kept in mind that this approximation is only valid for impacts against static objects, but it is still a reasonable approximation for dynamic situations. The final values of ϵ_{BB} and ϵ_{BW} were obtained through model calibration and are listed in section §5.4.2.

[5]There is a serious programming error in PFC3D 3.0 requiring $\zeta_{\text{BB}} = \frac{1}{\pi}(1-\epsilon_{\text{BB}})\sqrt{5/6}$ and not equation (5.25) for the correct COR for uniform sized ball-ball contacts.

PFC3D shear damping implementation

There is limited information on the implementation of damping in the shear direction. The PFC3D manual only states that the viscous force is set to zero if sliding occurs between bodies. In our implementation, the shear damping coefficient was taken as identical to the normal damping coefficient.

5.4 DEM setup and simulations

5.4.1 Model generation

For every simulation we select:

Container A, B, C, or D,
ball size $\varnothing 2$ mm, $\varnothing 3$ mm or $\varnothing 4$ mm,
rotation speed Ω.

The steps for setting up the DEM model and the simulation procedure are illustrated in figure 5.3. They are:

(a) Select the container and ball parameters:

h_c, R_c from table 5.1,
r_i, G, ν, ρ from table 5.2.

Generate the required number of balls in random positions and let them settle under gravitation. The friction and contact damping is set to zero and mass damping is employed to bring the system to equilibrium. The time step safety factor is set to 0.2.

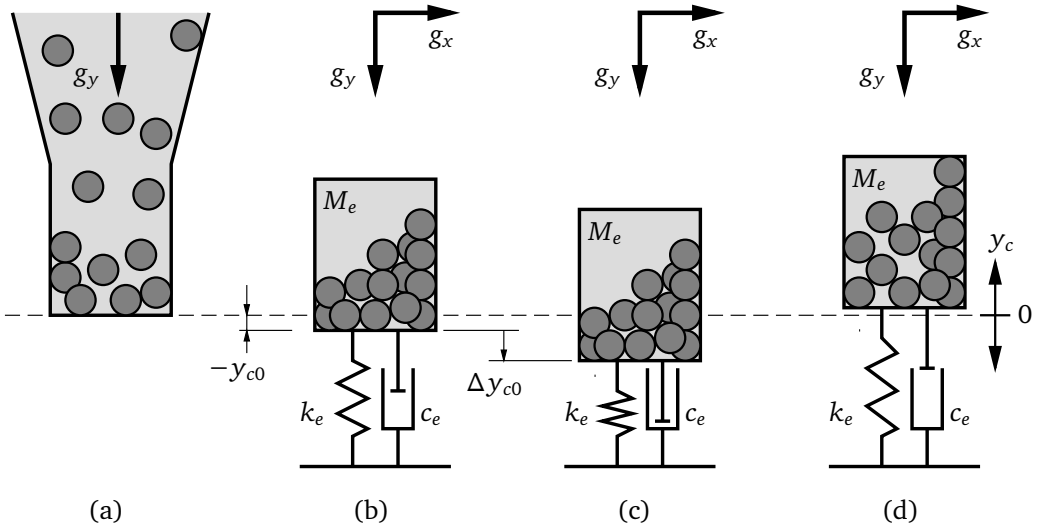

Figure 5.3. Setup and simulation procedure for DEM simulation

(b) Initialise the container equation of motion by calculating:

g_x radial acceleration from equation (5.1a),
M_e equivalent mass from equation (4.2),
k_e equivalent stiffness from equation (3.13),
c_e equivalent damping coefficient from equation (3.14).

Set the simulation variables:

μ_{BB}, μ_{BW} friction coefficients,
ζ_{BB}, ζ_{BW} critical damping from equations (5.25) and (5.28).

Cycle the system until equilibrium is reached.

(c) Set the initial displacement Δy_{c0} and initialise time to $t = 0$.

(d) Start the simulation and record y_c against time for 4 s.

5.4.2 DEM model calibration

With the DEM model described in this chapter we can only change the damping and the friction coefficients. Experiments with similar stainless steel ball bearings were conducted by Wong *et al.* (2009) and it was used as a starting point for iterations.

A series of DEM simulations with different damping and friction coefficients were conducted. The results were compared to the results obtained in chapter 4 in terms of the parameters shown in figure 4.5. The simulation results were analysed with the same methods and procedures used for the experimental data as given in section §4.5. It was found that the damping had only a minor influence. The friction was the main driver in the performance of the PD. The final parameters are given in table 5.4.

The friction coefficient $\mu = 0.3$ for the friction between the balls and the COR of 95 % correspond well with the experimental values obtained by Wong *et al.* (2009). Mark's handbook (Avallone and Baumeister, 1996, p. 3-23) gives $\mu = 0.47$ to 0.61 for steel on aluminium. Our final value is also in this range.

5.4.3 DEM simulations

Snapshots of the particle positions during a DEM simulation are shown in figure 5.4. The peak amplitudes over time of the PD motion, for the same simulation, are given in figure 5.5.

Table 5.4. DEM friction and damping parameters

		Ball-ball contacts[a]	Ball-wall contacts[b]
Coef. of restitution	ϵ	0.95	0.95
Damping factor	ζ	0.015	0.021
Shear damping factor	ζ_s	0.015	0.021
Friction coefficient	μ	0.3	0.5

[a] Stainless steel on stainless steel contacts.

[b] Stainless steel on aluminium contacts.

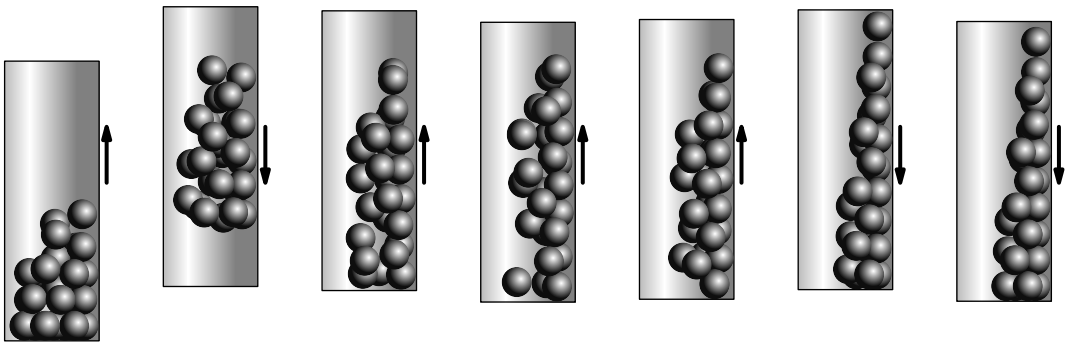

(a) 0.000 s (b) 0.043 s (c) 0.076 s (d) 0.133 s (e) 0.254 s (f) 0.947 s (g) 2.000 s

Figure 5.4. DEM particle motion for container A with ⌀4 mm balls and rotation velocity of $\Omega = 116\,\mathrm{min}^{-1}$.

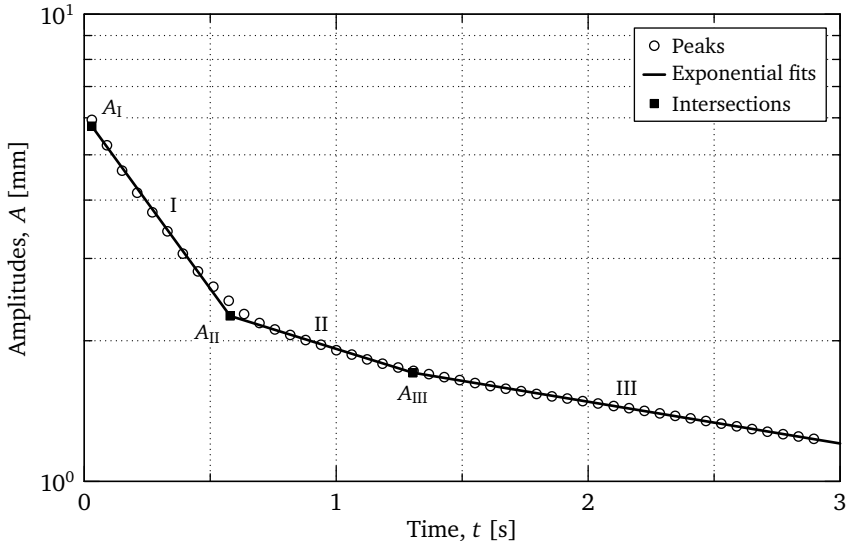

Figure 5.5. Peak amplitudes for a DEM simulation for container A with ⌀4 mm balls and rotation velocity of $\Omega = 116\,\mathrm{min}^{-1}$.

For zone I, it was observed during the DEM simulations, that the particles sloshed around inside the container and that physical gaps appear at the top and the bottom during the vibration cycles. The particles also slide/roll in layers across each other.

In zone II there was very little relative motion between the container and the particles. Only small gaps appear at the top and the bottom of the cycles. In zone III the particles move as a unit with the container.

5.5 Simulation results

After the model was calibrated, the same series of tests, as described in section §4.3 for the physical experiments, were duplicated with DEM simulations. Again the simulation results were analysed with the same methods and procedures used for the experimental data as given in section §4.5. An example of a series of results is shown in figure 5.6. The full set of results is given in figures B.1 to B.12 on pages 90–101.

It is clear that the DEM model of the rotating beam with a PD on the tip, captures the performance of the PD very well over a wide range of tests with different configurations and rotation velocities.

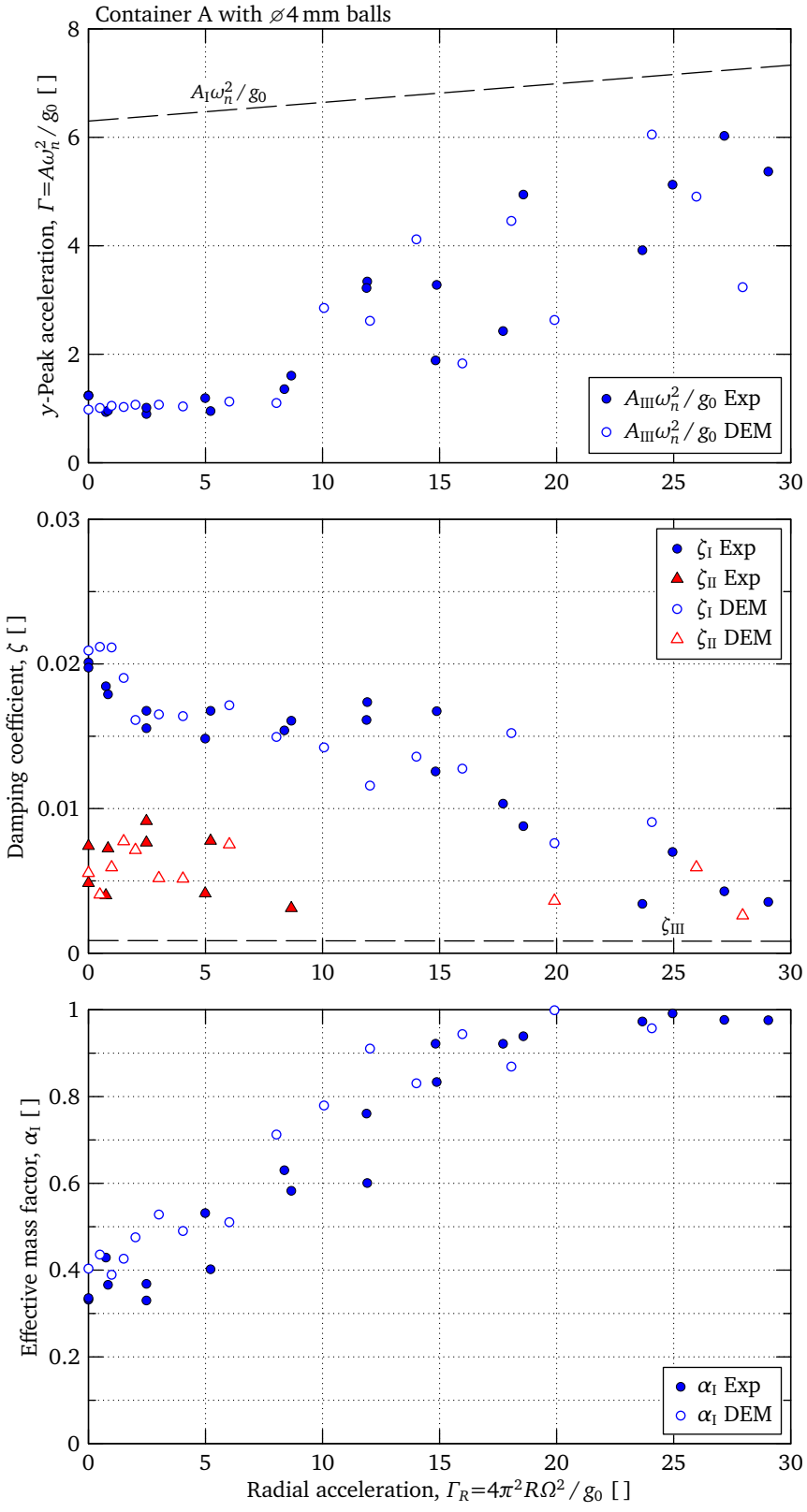

Figure 5.6. Example of DEM test data (container A with ⌀4 mm balls)

Chapter

6

Data Analysis

List of symbols for chapter 6

Constants

$g_0 = 9.81\,\mathrm{m/s^2}$	standard gravitational acceleration
$R = 0.4\,\mathrm{m}$	rotation radius

Variables

A	amplitude of oscillations	[m]
A'	effective area under centrifugal loads	[$\mathrm{m^2}$]
c_e	equivalent beam damping coefficient (eqn. 3.14)	[N·s / m]
C	number of contacts	
d_c	container diameter (tab. 5.1)	[m]
E_b	ball kinetic and potential energy (eqn. 6.15)	[J]
E_c	container kinetic and potential energy (eqn. 6.12)	[J]
F_{nk}	normal contact elastic force (eqn. 5.5)	[N]
h_0	average fill height (eqn. 6.1)	[m]
h'_0	average effective fill height (fig. 6.2)	[m]
h_c	container height (tab. 5.1)	[m]
i, j, ℓ	indices	
J	ball moment of inertia, $J = \frac{2}{5} m R^2$	[kg·$\mathrm{m^2}$]
k_e	equivalent beam stiffness (eqn. 3.13)	[N / m]
$\bar{k}_n$	PFC3D Hertz normal stiffness coefficient (eqn. 5.5)	[$\mathrm{N/m^{3/2}}$]
$\bar{k}_s$	PFC3D Hertz shear stiffness coefficient (eqn. 5.10)	[$\mathrm{N/m^{3/2}}$]
m	ball mass, $m = \frac{4}{3}\pi\,\rho\,R^3$	[kg]
m_e	equivalent beam mass (eqn. 3.10)	[kg]
M_e	equivalent tip container mass (eqn. 4.2)	[kg]

n_0	number of balls in contact with base	
n_d	number of equivalent layers, $n_d = h_0 / (2r_i)$	[−]
n'_d	number of effective layers, $n'_d = h'_0 / (2r_i) = n_d / \lambda$	[−]
N	number of balls	
P	number of time steps, $t = \sum_{i=1}^{P} \Delta t_i$	
r	ball radius	[m]
t	time	[s]
Δt	integration time step	[s]
T_g	granular temperature (eqn. 6.27)	[J]
$\overline{\boldsymbol{v}}$	ball velocity vector	[m / s]
W_c	container damper loss (eqn. 6.24)	[J]
W_δ	strain work performed (eqn. 6.21)	[J]
W_μ	friction work performed (eqn. 6.26)	[J]
x, y, z	Cartesian coordinates	[m]
$\overline{\boldsymbol{x}}$	ball position vector	[m]
y_c	container vertical displacement	[m]
$\dot{y}_c$	container vertical velocity	[m / s]
$\ddot{y}_c$	container vertical acceleration	[m / s^2]
Δy_{c0}	beam tip initial displacement	[m]
α	fraction of the particle contributing towards the total mass	[−]
δ	ball contact overlap	[m]
$\dot{\delta}$	ball contact velocity	[m / s]
γ	gap height, $\gamma = h_c - h_0$	[m]
Γ	peak acceleration amplitude factor, $\Gamma = A\omega^2 / g_0$	[−]
Γ_R	centrifugal acceleration factor, $\Gamma_R = R(2\pi\Omega)^2 / g_0$	[−]
λ	container cavity aspect ratio, $\lambda = h_c / d_c$	[−]
μ	friction coefficient	[−]
θ	angular parameter (fig. 6.2)	[rad]
ω	frequency	[rad / s]
$\overline{\boldsymbol{\omega}}$	ball angular velocity vector	[rad / s]
Ω	system rotation velocity	[s^{-1}]
ρ	ball density	[kg / m^3]
ζ	viscous damping factor	[−]

6.1 Introduction

The previous chapters have described in detail the experimental procedures to test particle dampers (PDs) under centrifugal loads. A discrete element method (DEM) model was constructed that numerically duplicated the physical experiments. In this chapter, a more detailed analysis of the results are presented. The correlations among the performance parameters are also analysed.

Another important aspect is how the energy inside the PD is dissipated. It is not possible to physically measure the different dissipation mechanisms, but with the aid of the DEM model developed in chapter 5, the internal energy and dissipation mechanisms of the PDs can be investigated. Finally the effect of the system vibration frequency on the performance of PDs is investigated with a DEM extrapolation.

6.2 System parameters

Fill height and equivalent layers

The true fill height of the balls inside the PD container cannot be measured directly, because the top layer is generally incomplete. In this section the fill height is calculated indirectly, with DEM simulations of the balls inside the container.

Fifteen different, randomly generated fills for each ball size were generated. The balls were left so settle under gravity and afterwards the coordinates of the centres of each ball was saved to a file for data processing. The procedure followed to obtain the fill height is illustrated in figure 6.1. The y-coordinates (vertical coordinates) for each set were sorted from small to large. The number of balls in contact with the base of the container was counted and denoted by n_0. The assumption was made that this is the effective number of balls in a layer. If N is the total number of balls, then the average height of the n_0 highest balls is the average effective fill height.

$$h_0 = r_i + \bar{y} \quad \text{with} \quad \bar{y} = \frac{1}{n_0} \sum_{i=N-n_0}^{N} y_i \tag{6.1}$$

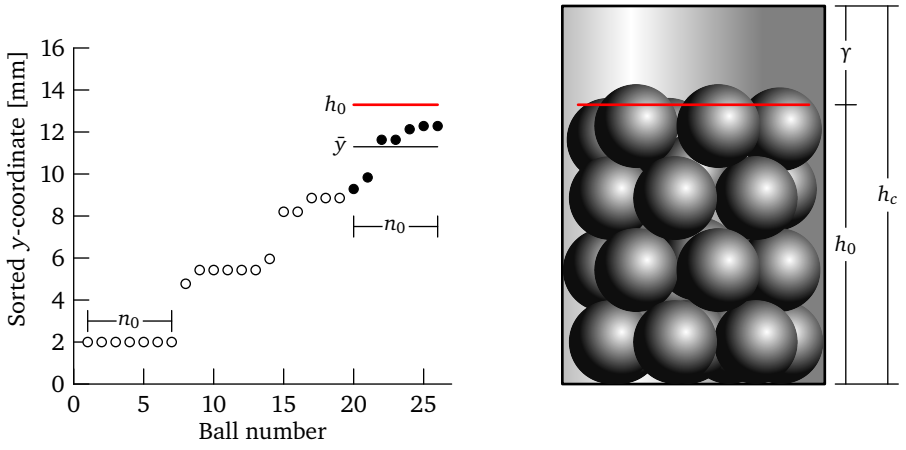

Figure 6.1. Example of fill height calculations for ⌀4 mm balls

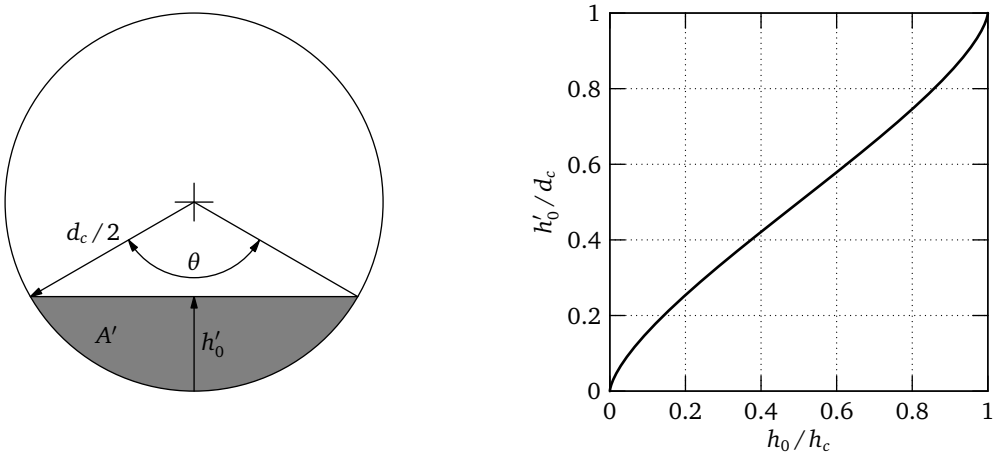

Figure 6.2. Fill height calculations for balls against sidewall

The number of equivalent layers is defined as

$$n_d = \frac{h_0}{2r_i}. \tag{6.2}$$

The calculated average effective fill heights and number of equivalent layers are listed in table 6.1. The tolerance of h_0 is one standard deviation.

With reference to figure 5.4 on page 55 is it clear that under centrifugal loads the particles move againt the side of the container. The fill volume of the particles under centrifugal load can be calculated as

$$\frac{\pi d_c^2 h_0}{4} = A' h_c = \frac{d_c^2 h_c}{8}\big(\theta - \sin\theta\big) \tag{6.3}$$

with A' the area of the sector as shown in figure 6.2. Rewrite equation (6.3) as

$$\frac{h_0}{h_c} = \frac{1}{2\pi}\big(\theta - \sin\theta\big). \tag{6.4}$$

From the geometry in figure 6.2, the height h'_0 of the sector area A' is

$$\frac{h'_0}{d_c} = \frac{1}{2}\big(1 - \cos\tfrac{1}{2}\theta\big). \tag{6.5}$$

From the parametric plot of h_0/h_c and h'_0/d_c as functions of θ in figure 6.2 is it clear that we can approximate the relation ship between the parameters as

$$\frac{h'_0}{d_c} \approx \frac{h_0}{h_c} \quad \text{or} \quad h'_0 \approx h_0 \frac{d_c}{h_c} = \frac{h_0}{\lambda} \tag{6.6}$$

with λ the container cavity aspect ratio (length/diameter) given in equation (6.9) on the following page.

The number of effective layers under centrifugal load can then be defined as

$$n'_d = \frac{h'_0}{2r_i} \approx \frac{n_d}{\lambda}. \tag{6.7}$$

Table 6.1. Ball fill parameters

Ball size	Ball radius r_i [mm]	Number of balls N	Fill height h_0 [mm]	Equivalent layers n_d [−]	Gap height γ_A [mm]	γ_B [mm]	γ_C [mm]	γ_D [mm]
⌀2 mm	1.0	207	12.8±0.1	6.3	24.2	18.2	12.5	9.0
⌀3 mm	1.5	64	13.6±0.3	4.5	23.4	17.4	11.7	8.2
⌀4 mm	2.0	26	13.4±0.4	3.3	23.6	17.6	11.9	8.4

Gap height

The clearance or gap height or free space between the balls and the top lid of the container is

$$\gamma = h_c - h_0 \tag{6.8}$$

Table 4.2 on page 35 lists the container heights h_c and table 6.1 the gap heights.

Container aspect ratio

The container cavity aspect ratio (length/diameter),

$$\lambda = \frac{h_c}{d_c}, \tag{6.9}$$

is identified in the literature as one of the significant parameters influencing the performance of PDs vibrating perpendicular to gravity (Liu *et al.*, 2005). Note that the fill height h_0 is more or less constant in table 6.1. It is therefore not possible to distinguish between the effects of the gap height and the cavity aspect ratio, because they are directly related for this experimental setup. The cavity aspect ratios are listed in table 6.2.

Table 6.2. Container cavity aspect ratio

Container	Aspect ratio λ
A	2.96
B	2.84
C	2.02
D	1.74

6.3 Parameter correlations

6.3.1 Definitions

In the design of the experimental apparatus the decision was taken to use a constant tip or PD mass. The parameters that vary for each PD configuration are listed in

tables 6.1 and 6.2. The fill height h_0 can be taken as constant. The number of equivalent layers n_d varies with ball size but is independent of the container type. The gap height γ on the other hand varies with container type but is independent of the ball size for all practical purposes and the cavity aspect ratio λ varies only with container type. We will only consider the aspect ratio and not the fill height, because they are directly related.

The next step is to investigate the influence of n_d and λ on the performance of PDs under centrifugal loads by scaling the parameters in the performance graphs, figures A.1 to A.12. To compare the different configurations, define the following scaling parameters

$$n^*_{d_i} = n_{d_i} / n_{d_{\text{ref}}} \qquad \text{with} \quad i = \varnothing 2\,\text{mm},\ \varnothing 3\,\text{mm},\ \varnothing 4\,\text{mm}, \tag{6.10}$$

and

$$\lambda^*_j = \lambda_j / \lambda_{\text{ref}} \qquad \text{with} \quad j = \text{A, B, C, D.} \tag{6.11}$$

Container A with $\varnothing 2$ mm balls was taken as reference and $n_{d_{\text{ref}}}$=6.3 and λ_{ref}=2.96 the reference values.

6.3.2 Comments on the parameter scaling results

The objective with the parameter comparisons was to obtain general tendencies and not accurate curve fits for all the data. Of interest are the regions with a significant centrifugal acceleration (Γ_R>1). The procedure followed was first to compare a single container filled with different ball sizes (see test matrix, table 4.3 on page 36). In this way the influence of the number of equivalent layers n_d could be established. The second step was to compare a single ball size in different containers for an indication of the influence of the cavity aspect ratio λ. Figure 6.3 shows the final results of the effects of parameter scalings.

The important observation from this figure is that all the PD performance parameters scale as a function of the centrifugal acceleration $\Gamma_R\, n^*_d / \lambda^* = \Gamma_R\, n'^*_d$. This implies that a PD will function at higher centrifugal loads if the number of effective layers (n'_d) is decreased.

For the performance parameters individually it were found that the damping envelope, or the minimum peak vibration acceleration where the PD still functions, scale as $\Gamma / \sqrt{n^*_d}$. This indicates that a decrease number of layers (larger balls) will result in a lower peak vibration acceleration Γ where damping still occurs.

The damping factor in zone I scales as $\zeta_I \sqrt{\lambda^*}$. This indicates that an increase in the cavity aspect ratio decreases the damping factor. The relationship between the cavity aspect ratio and the damping factor corresponds with the general tendencies found in the literature.

The effective mass factor scales as $\alpha_I \sqrt{\lambda^*}$. An increase in λ will reduce α_I, which can be interpreted as more energetic motion of the balls.

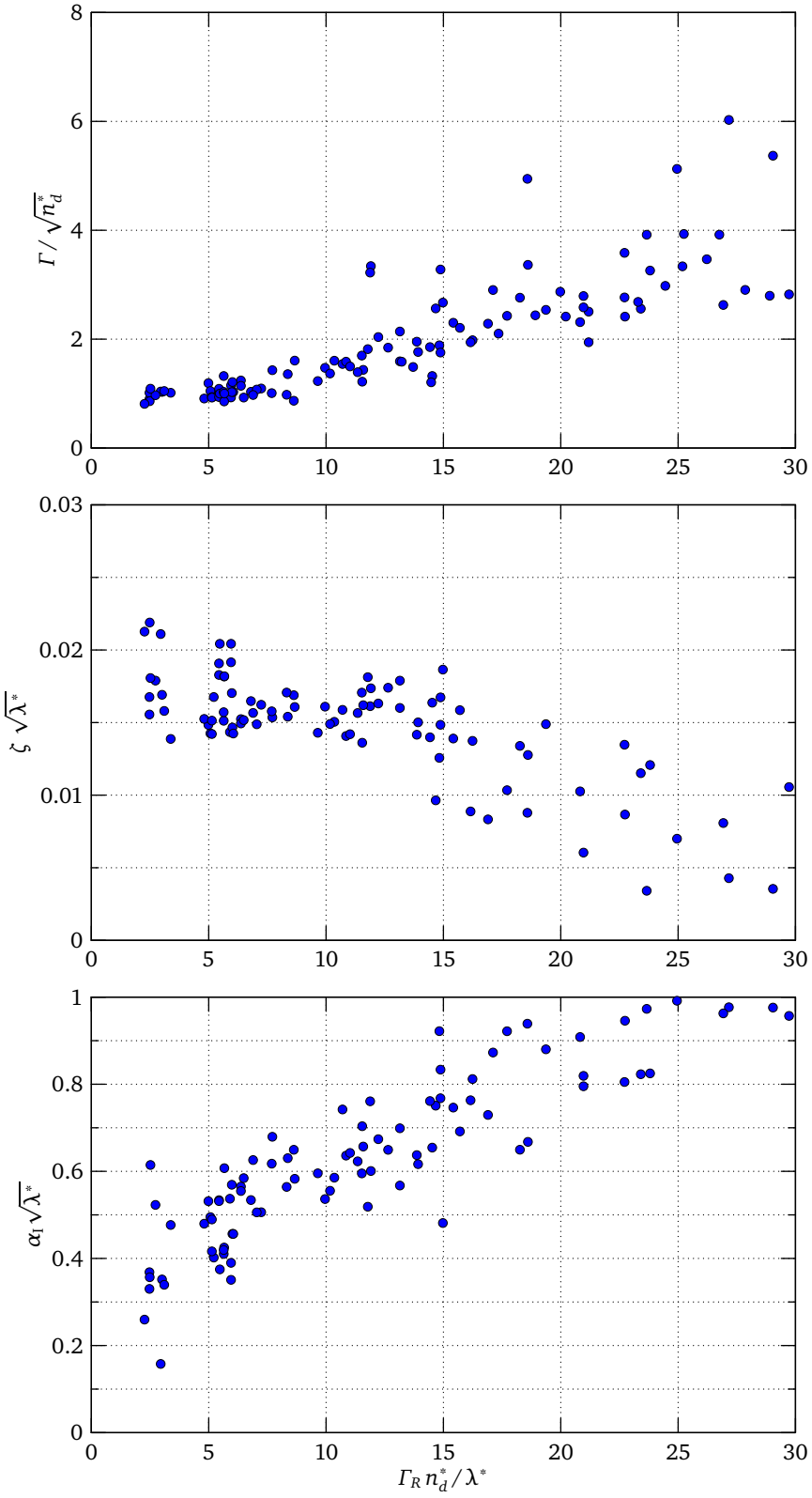

Figure 6.3. Parameter correlations for all the test data

6.4 Energy calculations

In order to trace the energy inside a functioning PD, an extended DEM model was constructed, where a number of energy parameters can be traced. During a simulation PFC3D makes a number of parameters available at every time step that can be used directly or manipulated further. In the following sections the methods used to extract the energy data are explained.

6.4.1 Internal energy

The definition of internal energy here is the energy resulting from conservative forces (forces without dissipation) such as kinetic, potential and elastic energy. It can be converted from one form to another, for example kinetic to potential energy and vice versa.

Container kinetic and potential energy

The equivalent single degree of freedom (SDOF) properties of the rotating beam were determined in section §3.3. The equivalent beam mass m_e, stiffness k_e and damping coefficient c_e in terms of the rotation velocity Ω (unit in s^{-1}) are

$$m_e = -7.587\,16\times10^{-7}\Omega^4 + 1.863\,02\times10^{-5}\Omega^3 + 2.228\,30\times10^{-4}\Omega^2 + 4.858\,02\times10^{-4}\Omega + 0.077\,526 \quad [\mathrm{kg}] \quad (3.10)^*$$

$$k_e = 0.480\,77\Omega^3 + 6.2839\Omega^2 - 7.2071\Omega + 1046.1 \quad [\mathrm{N/m}] \quad (3.13)^*$$

$$c_e = -9.1735\times10^{-7}\Omega^4 + 3.2263\times10^{-5}\Omega^3 - 1.8864\times10^{-4}\Omega^2 + 3.1662\times10^{-4}\Omega + 0.0180 \quad [\mathrm{N{\cdot}s/m}] \quad (3.14)^*$$

and the equivalent empty container mass

$$M_e = m_e + 0.016\,77\,\mathrm{kg}. \quad (4.2)^*$$

The total instantaneous kinetic and potential energy of the equivalent container at time t is

$$E_c = \tfrac{1}{2} M_e \dot{y}_c^2 + \tfrac{1}{2} k_e\, y_c^2 + M_e\, g_0\, (y_c - \Delta y_{c0}). \quad (6.12)$$

Ball kinetic and potential energy

For a ball with radius r_i and density ρ_i the mass is

$$m_i = \tfrac{4}{3}\pi\, \rho_i\, r_i^3, \quad (6.13)$$

and the moment of inertia

$$J_i = \tfrac{2}{5} m_i\, r_i^2. \quad (6.14)$$

Let $\overline{\boldsymbol{x}}_i = [x_i, y_i, z_i]^\mathsf{T}$ be the position, $\overline{\boldsymbol{v}}_i = [\dot{x}_i, \dot{y}_i, \dot{z}_i]^\mathsf{T}$ the velocity, and $\overline{\boldsymbol{\omega}}_i$ the angular velocity of the ball. The total instantaneous kinetic and potential energy summed over all the balls at time t is then

$$\Sigma E_b = \sum_{i=1}^{N} \left[\tfrac{1}{2} m_i \|\overline{\boldsymbol{v}}_i\|^2 + \tfrac{1}{2} J_i\, \|\overline{\boldsymbol{\omega}}_i\|^2 + m_i\, g_0\, (y_i - \Delta y_{c0}) \right]. \quad (6.15)$$

Note that in PFC3D the kinetic energy terms in equation (6.15) are one of the output parameters and the ball y-position can be obtained at every time step for the calculation of the potential energy.

Ball elastic energy

Energy is stored internally in elastic contacts. For the calculation of the stored elastic energy we can extract or calculate from PFC3D, for every contact, the nonlinear stiffness coefficients, $\bar{k}_n$ and $\bar{k}_s$, the overlap δ and the total normal and shear forces F_n and F_s.

The normal contact elastic force F_{nk} is given by

$$F_{nk} = \begin{cases} \bar{k}_n \, \delta^{3/2} & \text{ball-ball contact} \\ \bar{k}_n \, (2\delta)^{3/2} & \text{ball-wall contact} \end{cases} \tag{5.5}^*$$

The incremental work done to compress the balls in the normal direction a distance $\mathrm{d}\delta$, is

$$\mathrm{d}W_{\delta n} = F_{nk} \, \mathrm{d}\delta = \begin{cases} \bar{k}_n \, \delta^{3/2} \, \mathrm{d}\delta & \text{ball-ball contact} \\ \bar{k}_n \, (2\delta)^{3/2} \, \mathrm{d}\delta & \text{ball-wall contact} \end{cases} \tag{6.16}$$

If we integrate equation (6.16) for a total compression from 0 to δ, the total normal elastic work at every contact is

$$W_{\delta n} = \begin{cases} \frac{2}{5} \bar{k}_n \, \delta^{5/2} & \text{ball-ball contact} \\ \frac{2\sqrt{2}}{5} \bar{k}_n \, \delta^{5/2} & \text{ball-wall contact} \end{cases} \tag{6.17}$$

For the shear elastic force we assume it to be linear with respect to the shear displacement δ_s. The shear force is then

$$F_s = \bar{k}_s \, \delta_s \tag{6.18}$$

with the approximated Mindlin non-linear shear stiffness

$$\bar{k}_s = \frac{2\left[3\bar{G}^2(1-\bar{\nu}\bar{R})\right]^{1/3}}{2-\bar{\nu}} \, F_n^{1/3}, \tag{5.10}^*$$

and F_n the total normal force given by equation (5.4). The incremental work done to displace the balls in the shear direction a distance $\mathrm{d}\delta_s$ is

$$\mathrm{d}W_{\delta s} = F_s \, \mathrm{d}\delta_s = \bar{k}_s \, \delta_s \, \mathrm{d}\delta_s. \tag{6.19}$$

If we integrate equation (6.19) for a total compression from 0 to δ_s, the total shear elastic work at every contact is

$$W_{\delta s} = \tfrac{1}{2} \bar{k}_s \, \delta_s^2 = \tfrac{1}{2} F_s^2 / \bar{k}_s. \tag{6.20}$$

The total elastic energy stored in all the contacts at time t is then

$$\Sigma W_\delta = \sum_{i=1}^{C} (W_{\delta n_i} + W_{\delta s_i}), \tag{6.21}$$

with C the total number of contacts.

6.4.2 Energy dissipation

The dissipation or energy loss mechanisms in a PD are friction between the balls, contact damping between the balls and, for our simulation purposes, the external viscous damper of the beam. The main purpose of a PD is to dissipate energy from a structure or mechanism and a detailed analysis of where the energy is lost is the core of our analysis.

Beam damping

The increment in work losses by the beam damping over an incremental displacement $\mathrm{d}y_c$ is

$$\mathrm{d}W_c = c_e\,\dot{y}_c\,\mathrm{d}y_c = c_e\,\dot{y}_c^2\,\mathrm{d}t. \tag{6.22}$$

It can be approximated for a discrete time step Δt as

$$\Delta W_c = c_e\,\dot{y}_c^2\,\Delta t, \tag{6.23}$$

if we assume that $\dot{y}_c$ is the average container velocity during the time step. The increment in damping losses ΔW_c can then be summed throughout the simulation to obtain the total loss at time $t = \sum_{i=1}^{P} \Delta t_i$.

$$W_c = \sum_{i=1}^{P} \Delta W_{c_i} = \sum_{i=1}^{P} c_e\,\dot{y}_{c_i}^2\,\Delta t_i \tag{6.24}$$

with P the number of time steps.

Friction

The PFC3D friction model shown in figure 5.2 on page 48 allows for slippage to occur if $F_s \geq \mu F_n$. The amount of incremental slip work during each time step is

$$\Delta W_\mu = \mu\,F_n\,\Delta s_\mu, \tag{6.25}$$

with Δs_μ the friction slip distance. The numerical value of ΔW_μ is available as an output variable in PFC3D and can be summed over all the time steps

$$W_\mu = \sum_{i=1}^{P} \Delta W_{\mu_i} \tag{6.26}$$

with P the number of time steps.

Internal particle damping

There is no way to obtain the internal damping losses directly. If it is assumed that the total system energy is constant (internal energy plus losses), and that the amount of artificial energy added as result of numerical integration accuracy is negligible, then the internal damping is the difference between the total system energy at time $t = 0$ and the sum of all the other energy components at time t.

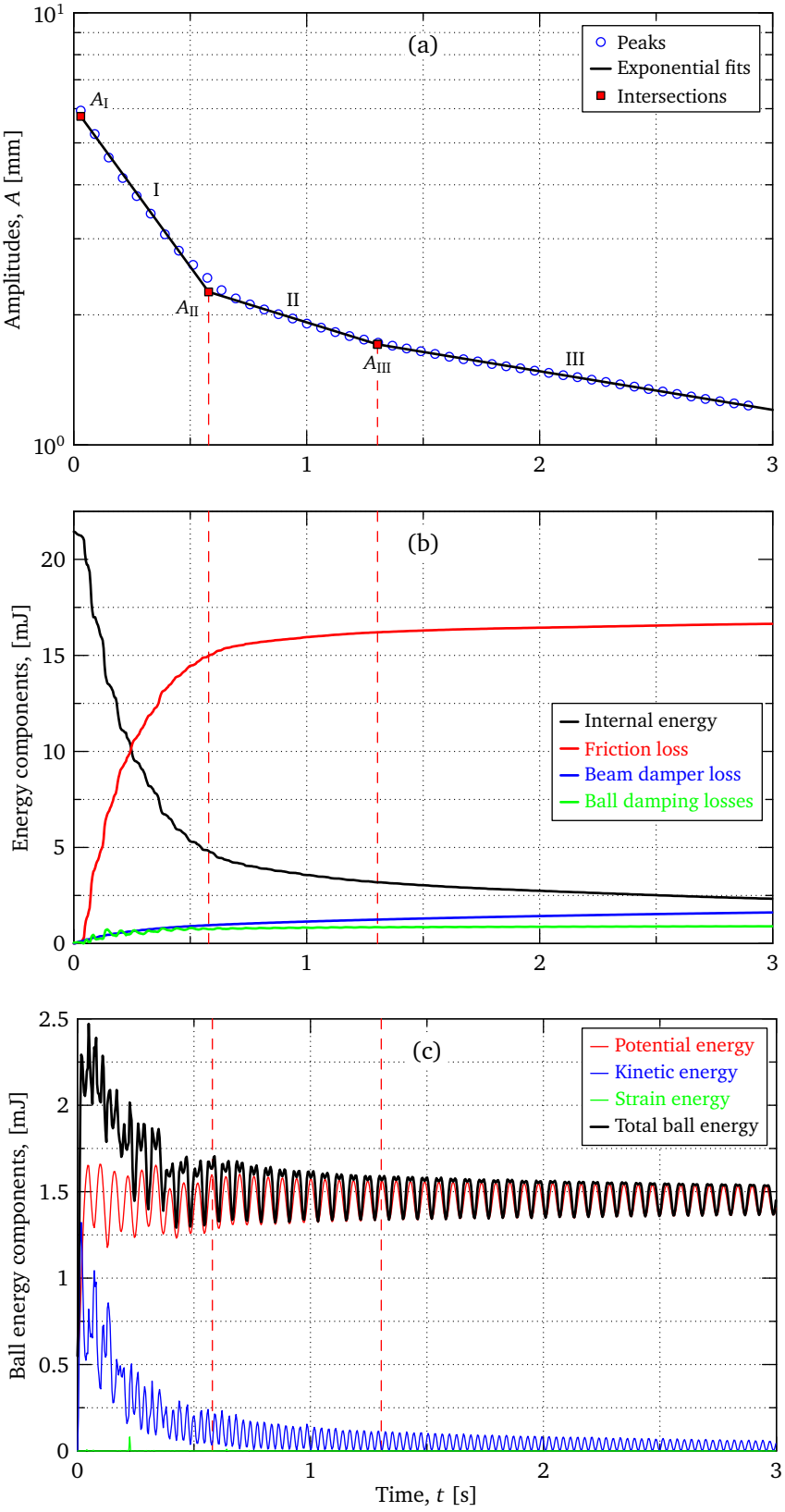

Figure 6.4. Example energy analysis for container A with ⌀4 mm balls and rotation velocity of $\Omega = 116\,\mathrm{min}^{-1}$. (a) Peak amplitudes. (b) Energy components. (c) Ball energy components.

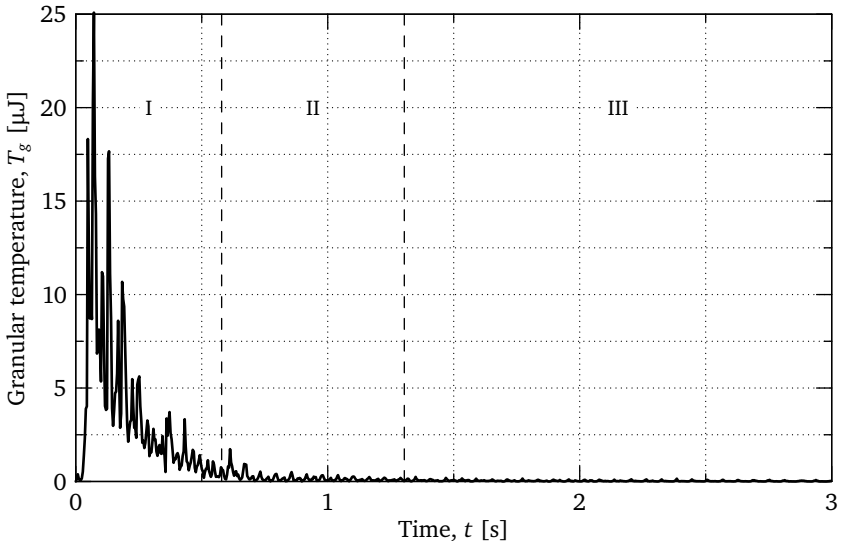

Figure 6.5. Example granular temperature calculation for container A with ⌀4 mm balls and rotation velocity of $\Omega = 116\,\mathrm{min}^{-1}$

6.4.3 Granular temperature

There exists a number of definitions for the granular temperature. The one used in this dissertation is the average kinetic energy fluctuation.

$$T_g = \frac{1}{N}\sum_{i=1}^{N} \tfrac{1}{2} m_i \left(\overline{\boldsymbol{v}}_i - \langle \overline{\boldsymbol{v}} \rangle \right)^2 \quad \text{with} \quad \langle \overline{\boldsymbol{v}} \rangle = \frac{1}{N}\sum_{i=1}^{N} \overline{\boldsymbol{v}}_i \tag{6.27}$$

with N the number of balls and $\overline{\boldsymbol{v}}_i$ the velocity of ball m_i.

6.4.4 Comments on energy analysis results

In figures 6.4(b) and (c) the results of a DEM simulation of a PD are shown with the different energy and dissipations terms. The internal energy is the sum of the kinetic and potential energy remaining in this system. The loss terms are cumulative and adds up to the reduction in internal energy. It is clear that the major loss mechanism is friction. It was found that the contributions of ball-ball friction and the ball-wall friction to the total loss is approximately equal.

The internal damping losses are small compared to the friction and this correlates with the observations during the DEM calibration (see section §5.4.2) that the damping had very little influence on the PD performance. Please note that the oscillation in the accumulated internal damping in figure 6.4(b) is because of the calculation method and is not a physical phenomenon.

The granular temperature is an indication of the excitation level of the balls and figure 6.5 shows the value for our example calculation. It can be seen that there is a threshold for T_g and, below this value, we do not see zone I damping any more. It is therefore clear that the high damping in zone I is a result of the excitation state of the balls.

For zone I, it was observed during the DEM simulations with full graphical animation, that the particles sloshed around inside the container and that physical gaps appear at the top and the bottom of the cycles. In zone II there was very little relative motion which was confirmed by the granular temperature analysis in figure 6.5.

6.5 The influence of vibration frequency

The question can be posed: what will the effect of a stiffer beam with a higher natural frequency be on the PD performance? To investigate this question, a DEM simulation was constructed with double the effective beam stiffness and all the other parameters identical to the standard configuration simulations of chapter 5. Doubling the stiffness results in an increase in natural frequency ω_n by a factor $\sqrt{2}$, and in the peak amplitude acceleration Γ, by a factor of two.

It must emphasised that this simulation is outside the calibration regime of the DEM model and that assumptions such as elastic impacts may no longer be valid. The results must be seen as an indication of tendencies and not exact values. Figure 6.6 shows the comparison between the beam with stiffness $2k_e$ and the DEM simulations of the standard configuration. The following observations can be made:

(a) For the damping envelope, the ratio Γ/Γ_R follows the same tendency as obtained for the standard configuration. This indicates that the ratio Γ/Γ_R is a fundamental property of PDs under centrifugal loads. In terms of the vibration amplitude it means that if the stiffness is doubled, it results in the halving of the amplitude above which damping occurs.

(b) The magnitude of the damping factor ζ in zones I and II is unchanged for low values of Γ_R. For Γ_R>15 the damper is still active and the the range of Γ_R where damping occurs is approximately doubled compared to the standard configuration.

(c) The slope of α_{I} versus Γ_R approximately halves. This corresponds with the extended range of Γ_R where damping still occurs.

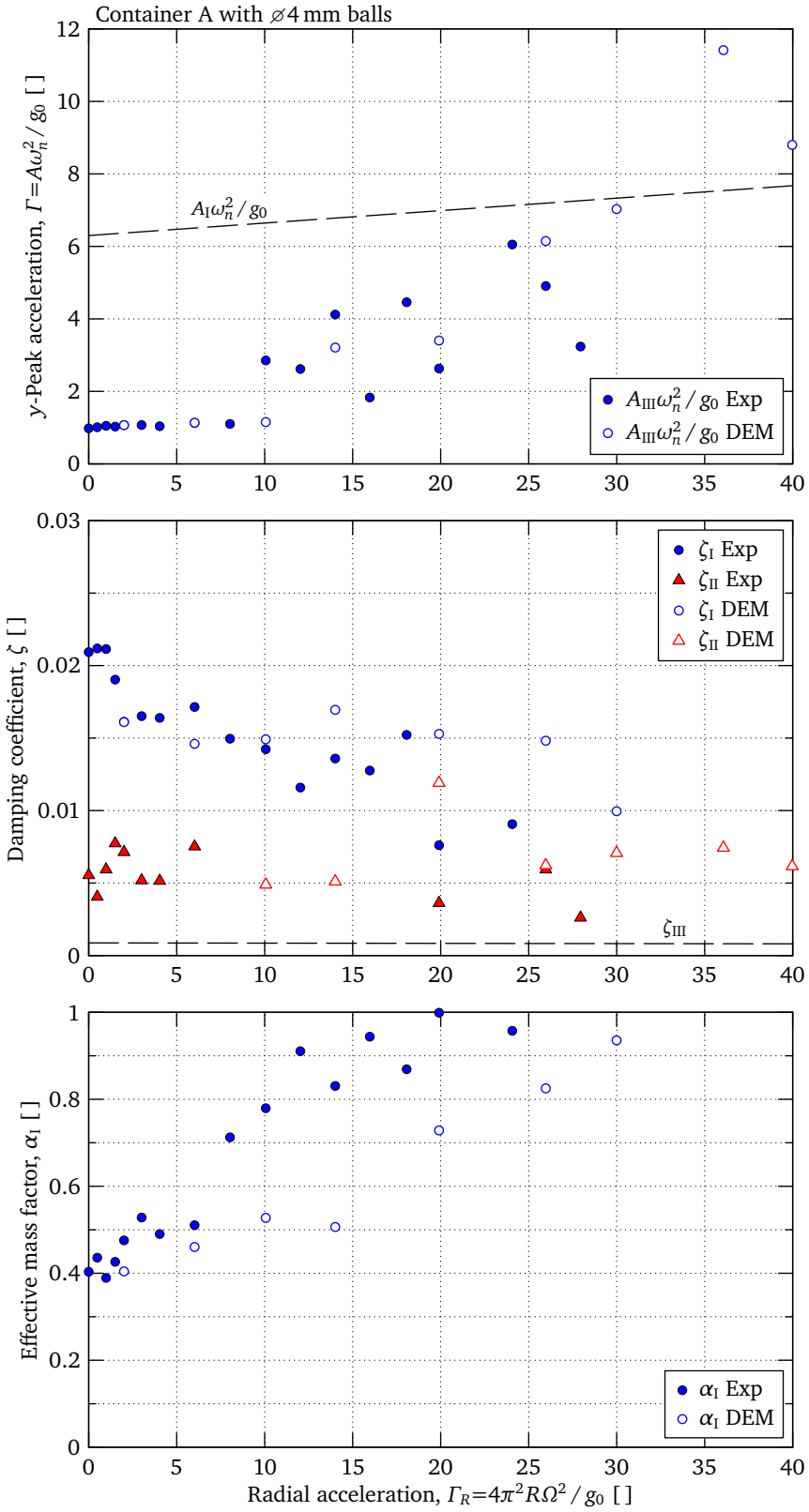

Figure 6.6. Example of DEM test data comparing a beam with double the stiffness to the standard configuration for container A with ⌀4 mm balls

Chapter

7

Conclusions and Recommendations

Constants

$g_0 = 9.81\,\mathrm{m/s^2}$	standard gravitational acceleration
$R = 0.4\,\mathrm{m}$	rotation radius

Variables

A	amplitude of oscillations	$[\,\mathrm{m}\,]$
Γ	peak acceleration amplitude factor, $\Gamma = A\omega^2 / g_0$	$[\,-\,]$
Γ_R	centrifugal acceleration factor, $\Gamma_R = R(2\pi\Omega)^2 / g_0$	$[\,-\,]$
ω	frequency	$[\,\mathrm{rad/s}\,]$
Ω	system rotation velocity	$[\,\mathrm{s^{-1}}\,]$
ζ	viscous damping factor	$[\,-\,]$

7.1 Overview

This dissertation describes the work that was done to investigate the effectiveness of particle dampers (PDs) under centrifugal loads. This can be seen as a PD under any acceleration load while vibrating in a direction perpendicular to the load. This research can be applied to the damping of rotating structures, accelerating rockets, and turning aircraft or ground vehicles.

An experimental apparatus was manufactured to measure the damping effect of a PD on a rotating beam. A series of PD containers were manufactured and filled with different uniform sized steel balls. All the PDs had the same mass. These PDs were tested over a range of centrifugal loads, while the beam was in a free decay vibration mode. Standard algorithms and self developed methods were used to extract the vibration and damping parameters from the test data.

A discrete element method (DEM) model was developed to numerically duplicate the experiment as accurately as possible. The model was calibrated against the experimental results. Good correlations between the experimental and numerical results were obtained with input parameters such, as inter-particle friction and damping corresponding well with published calibration data. With the DEM model, further investigations into the behaviour of PDs were conducted.

The main purpose of this dissertation was to determine the effect of centrifugal loading on the damping performance of PDs. The damping performance constitutes two parameters:

- The damping coefficient, ζ.
- The minimum excitation acceleration where the damper is still active (damping envelope).

Figure 7.1 gives a summation of the general trends observed in the test data from figures A.1 to A.12 on pages 77–88.

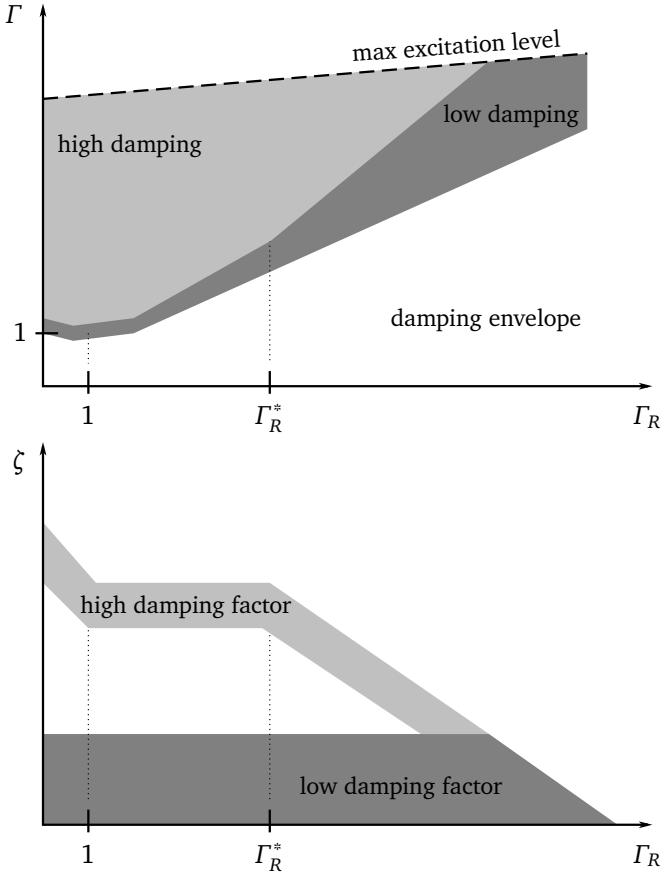

Figure 7.1. Particle damper performance factors

7.2 Conclusions

There are two distinct damping zones.

From the data analysis in chapter 4 it can be concluded that there are two zones of damping, one with a high and one with a low damping factor. These damping zones depend on the ratio between the peak vibration acceleration and the centrifugal loading. Each zone has a limit in terms of the centrifugal loading beyond which the PD cannot function if the vibration amplitude is fixed. In the high damping zone, it was found that the excitation state of the particles was high enough to move relative to the container thereby causing the system vibration frequency to change. In the low damping zone, there is only limited motion between the particles.

It is also noticeable that the damping factor in the high damping zone (see figure 4.5 on page 42) is approximately constant for centrifugal loads of more than 1 g_0 up to the load point where the high excitation state of the particles disappears (Γ_R^* in figure 7.1). This constant region is highly dependant on the PD container depth and can be increased with a container with a larger depth (or aspect ratio).

Friction, the container length/diameter aspect ratio, and the particle size are the main performance drivers.

In the extended analysis of chapter 6, it was found that the main parameters that influence the performance of the PDs are the friction between the particles themselves and with the container, the PD cavity length/diameter aspect ratio, and the particle size.

- The major energy dissipation mechanism is friction.
- An increase in the cavity aspect ratio or the number of layers decreases the damping factor in the high damping zone.
- An increase in particle size (decrease in number of layers) increase the damping factor in the high damping zone.
- An important finding is that a PD with less layers (increase in particle size) will still function at a higher centrifugal load compared to one with a smaller number number of layers.

The ratio Γ / Γ_R is a fundamental property of PDs under centrifugal loading.

The final analysis in chapter 6 concluded that the ratio between the peak vibration acceleration and the centrifugal loading is a fundamental property of PDs under centrifugal loads and can be used to effectively describe the envelope of functioning of the PD. In terms of the vibration amplitude it means that if the stiffness is doubled, it results in the halving of the amplitude above which damping occurs

7.3 Future work

In this dissertation some shortcomings were identified that need further investigation. The research was limited to a very small subset of parameters for PDs under centrifugal loads. In the rest of this section, a number of future recommended tasks are listed.

Experimental apparatus

The scope of this research was restricted by the capabilities of the experimental apparatus. Further refinements are necessary to handle a range of different beams and to reduce secondary vibration noise. This will enable the testing of PDs over a wider operating range and expand the current research to more generalised environment.

In section §3.2.2 it was found that the dynamic calibration of the strain gauges is a problem, because of the centrifugal effects on the shape and possible bending moments at the point of measurement. This needs further investigation or a different displacement measurement system.

Range of particle damper properties

There are various opportunities to extend this research for different PD configurations. Most urgent is an investigation into containers with different diameters while the depth is kept constant. This will enable a closer look at the effect of aspect ratio on the performance in general. Other properties that need investigation are friction and particle shape.

Non-static frequency

In section §4.5 it was shown that it is possible to extract the instantaneous frequency with a method derived from first principles. The assumption was then made that the damping and frequency are constant for the different damping zones. With more advanced methods such as the Hilbert vibration decomposition (HVD) method (Feldman, 2006) the non-linear damping properties can be determined.

DEM simulations and calibration

The commercial DEM software (PFC3D) used for this research is limited as a research tool. A DEM software dedicated for PD simulations where the constitutive and other numerical models such as particle shape can be user defined, would be of great benefit to research in this field.

One of the main problems in general for DEM simulations is obtaining calibrated parameters for the particles. A lot of work in this area is needed.

Appendix

A

Experimental Test Results

List of symbols for appendix A

Constants

$g_0 = 9.81\,\mathrm{m/s^2}$	standard gravitational acceleration
$R = 0.4\,\mathrm{m}$	rotation radius

Variables

A	amplitude of oscillations	[m]
m_e	equivalent beam mass (eqn. 3.10)	[kg]
m_p	average total particle mass	[kg]
M_e	equivalent tip container mass (eqn. 4.2)	[kg]
r_m	mass ratio, $r_m = m_p / M_e$	[kg]
t	time	[s]
α	fraction of the particle contributing towards the total mass	[−]
Γ	peak acceleration amplitude factor, $\Gamma = A\omega^2 / g_0$	[−]
Γ_R	centrifugal acceleration factor, $\Gamma_R = R(2\pi\Omega)^2 / g_0$	[−]
ω_n	natural frequency, $\omega_n = \sqrt{k/m}$	[rad/s]
Ω	system rotation velocity	[$\mathrm{s^{-1}}$]
ζ	viscous damping factor, $\zeta = c/(2m\omega_n)$	[−]

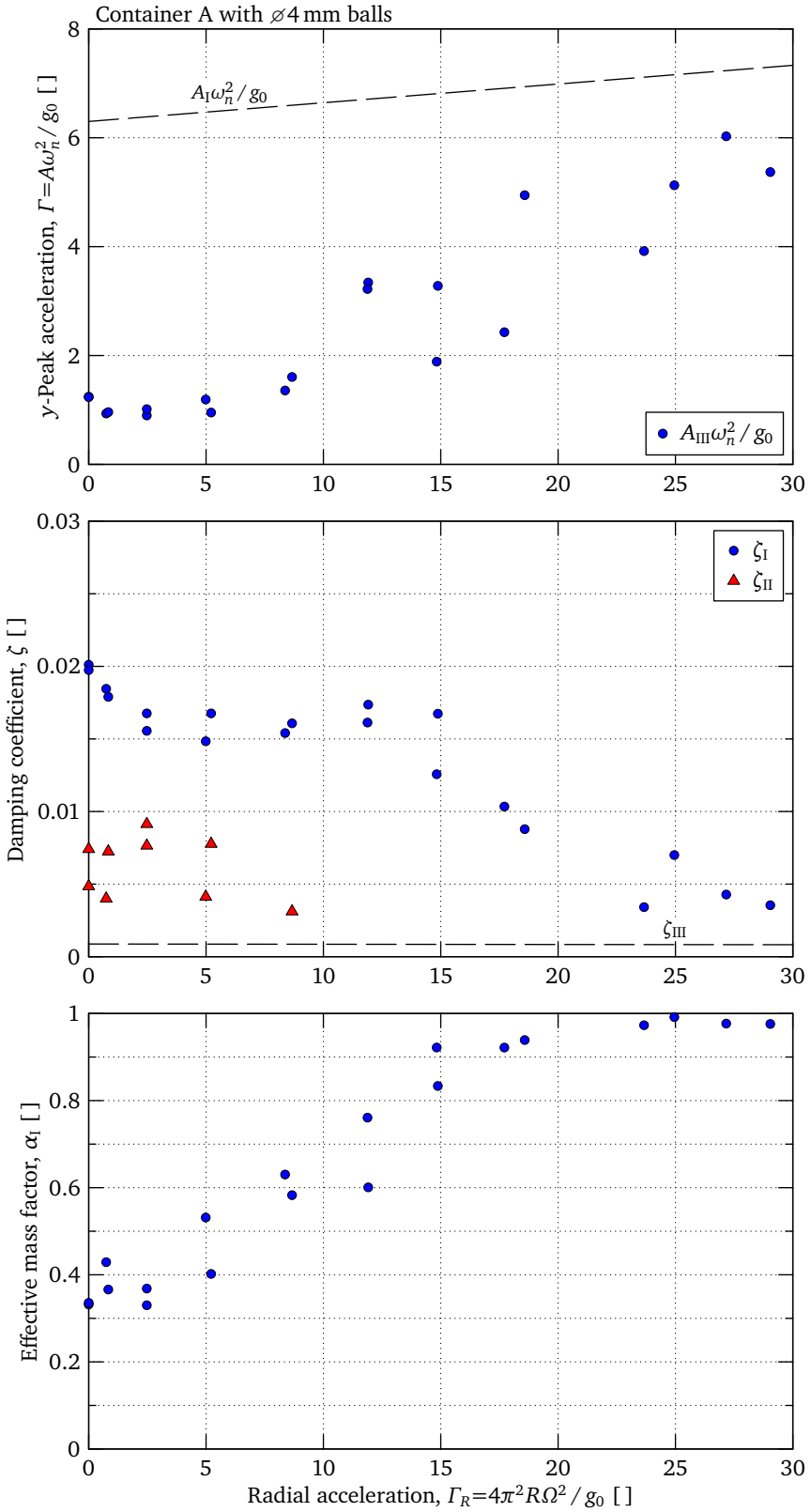

Figure A.1. Test result for container A with ⌀4 mm balls

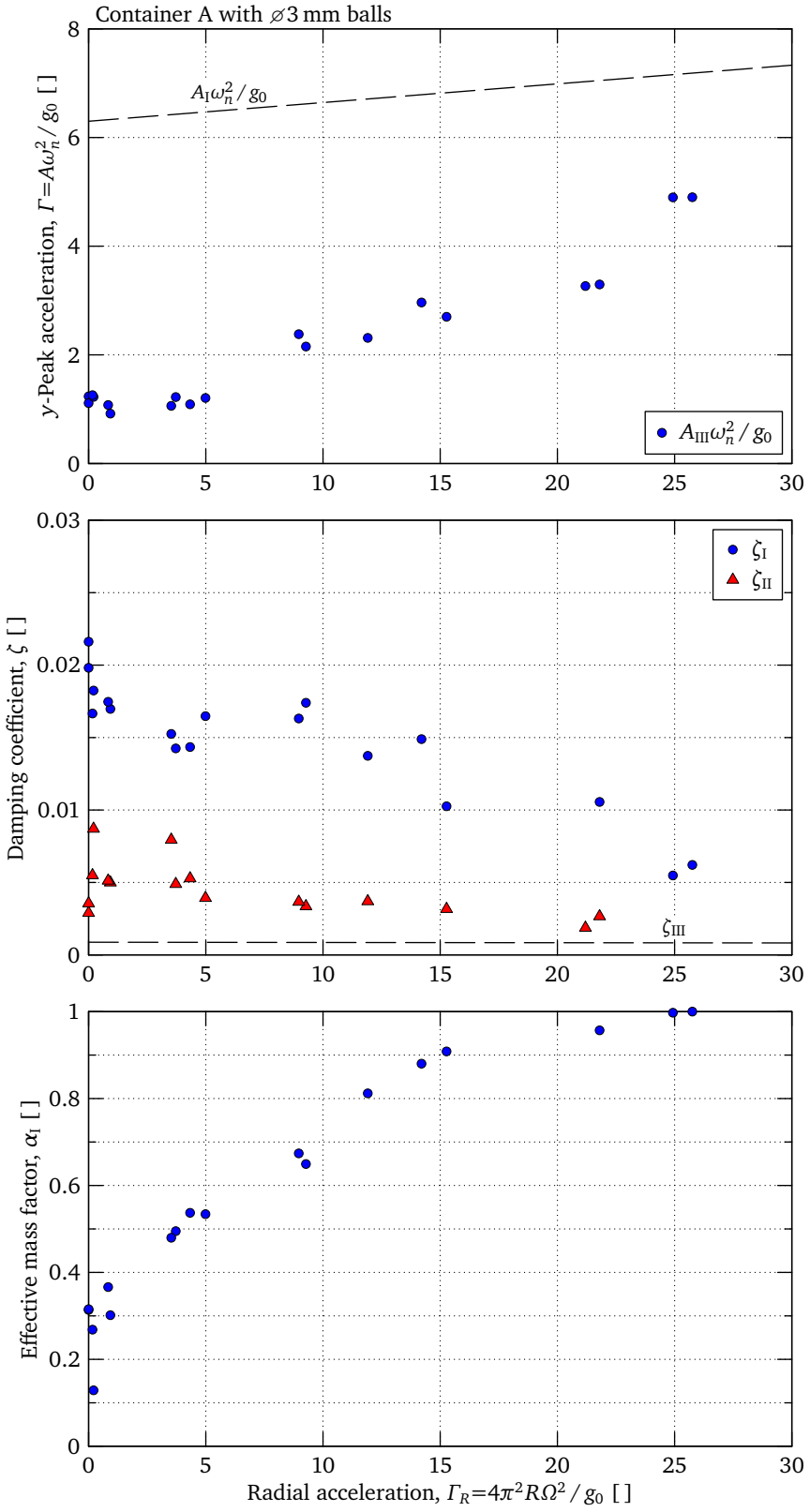

Figure A.2. Test result for container A with ⌀3 mm balls

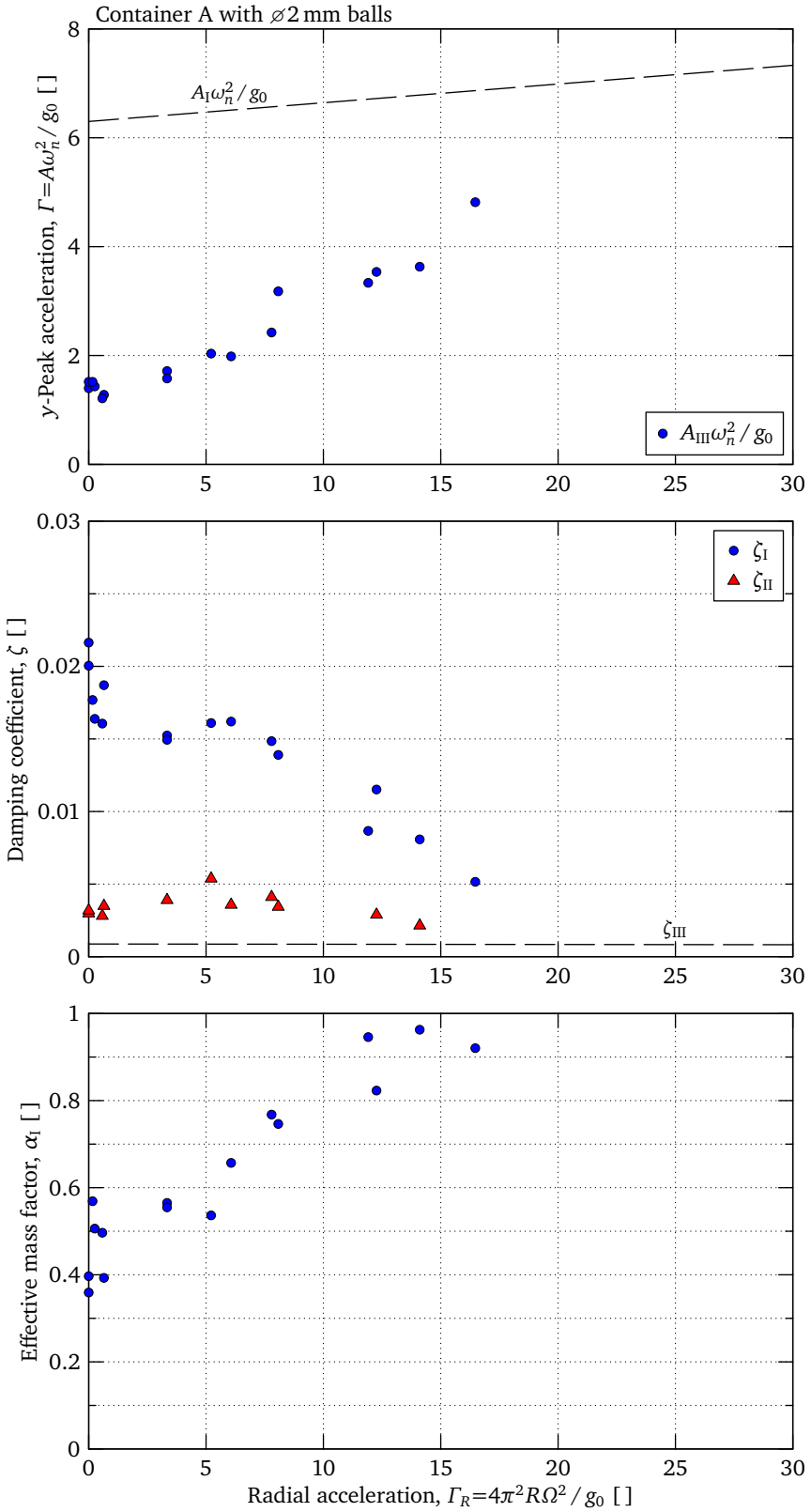

Figure A.3. Test result for container A with ⌀2 mm balls

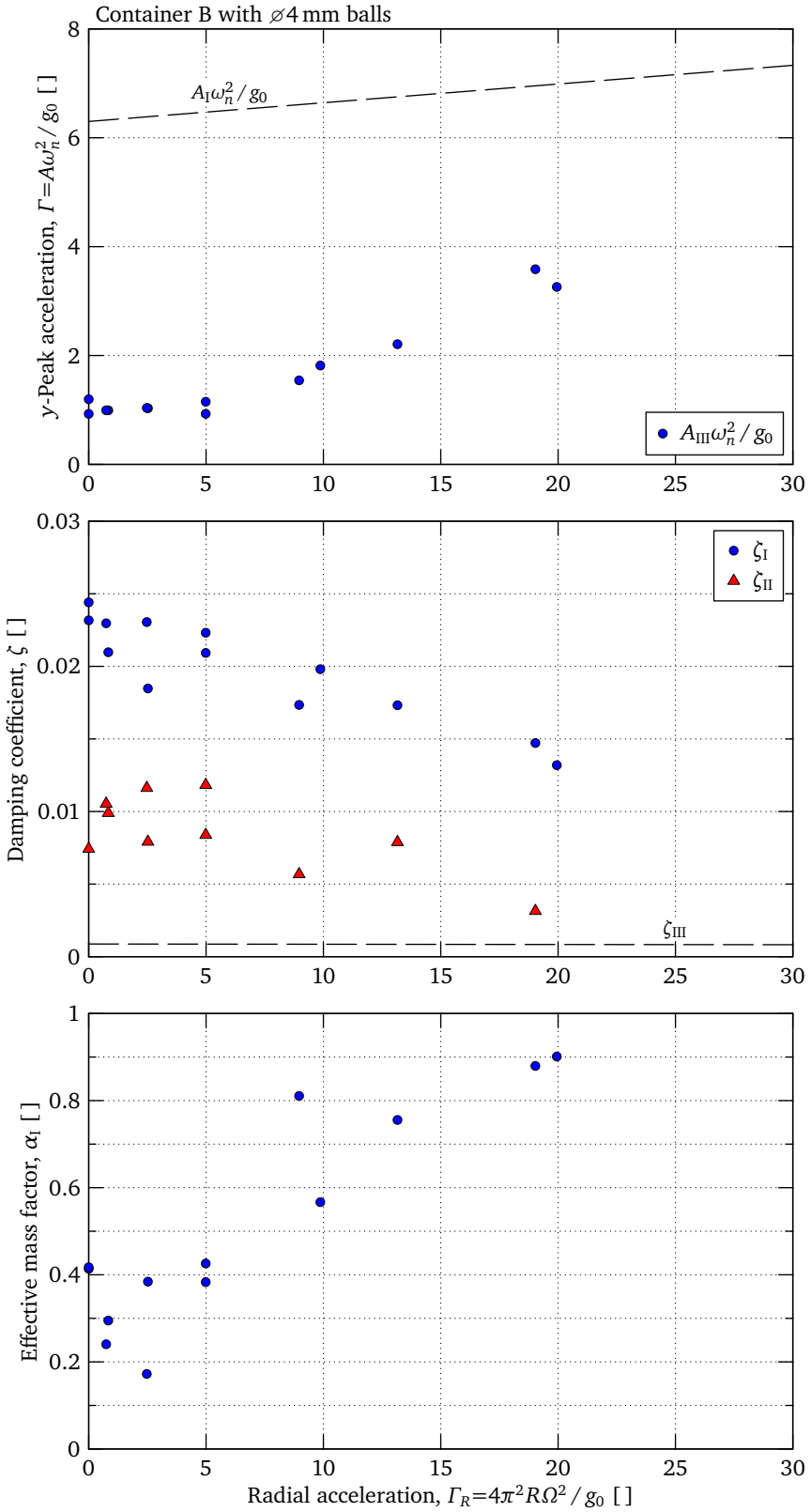

Figure A.4. Test result for container B with ⌀4 mm balls

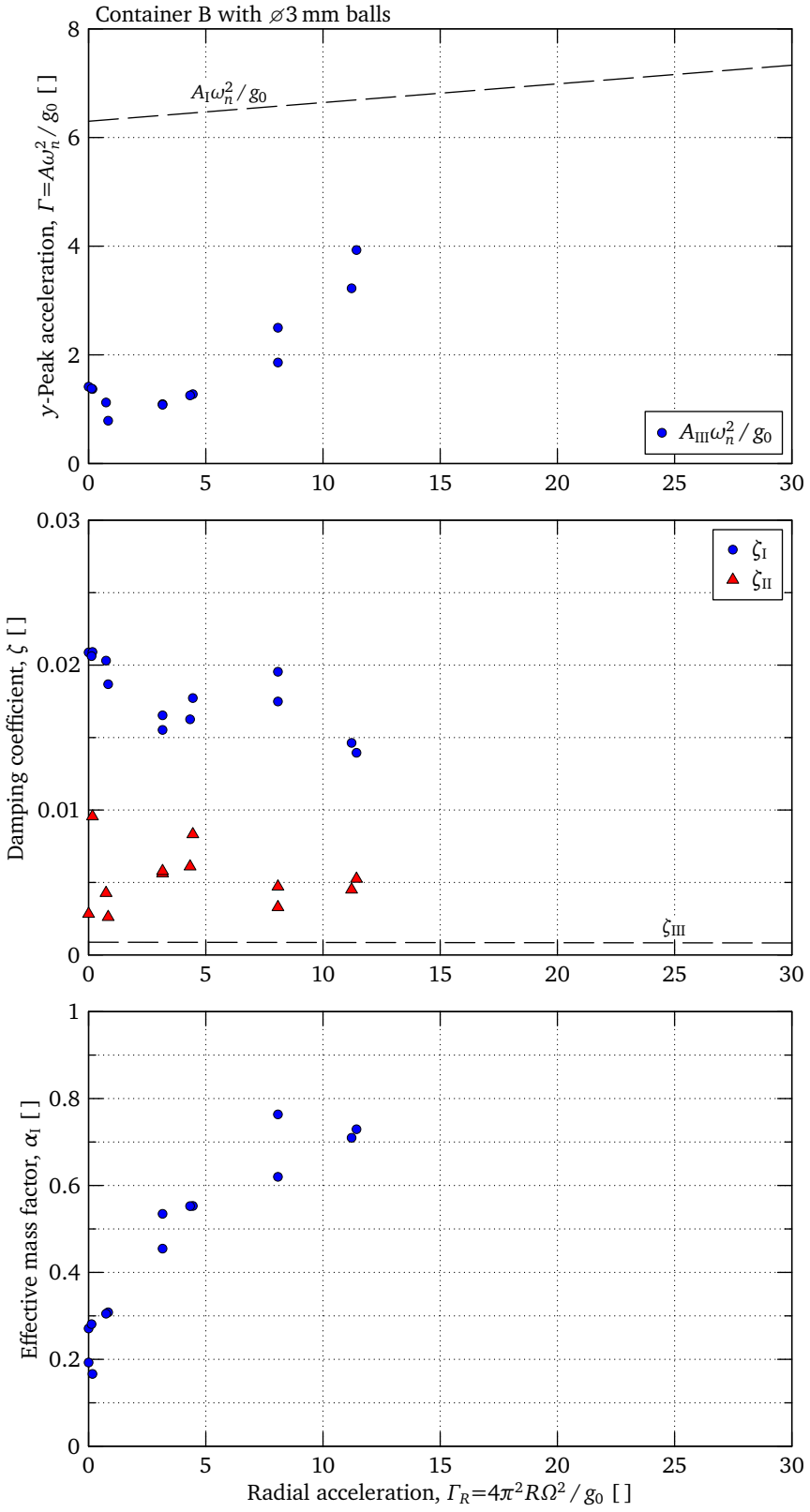

Figure A.5. Test result for container B with ⌀3 mm balls

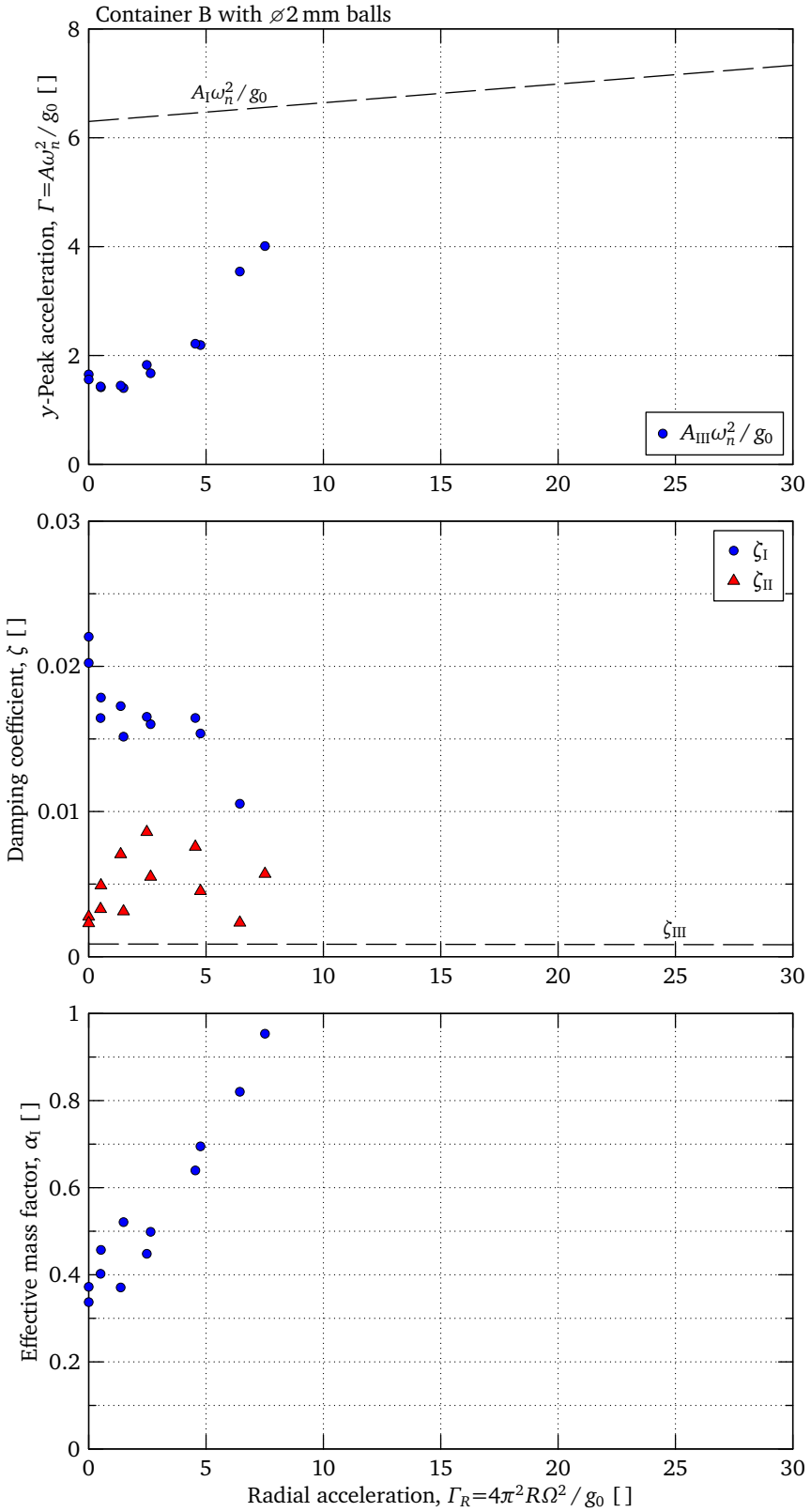

Figure A.6. Test result for container B with ⌀2 mm balls

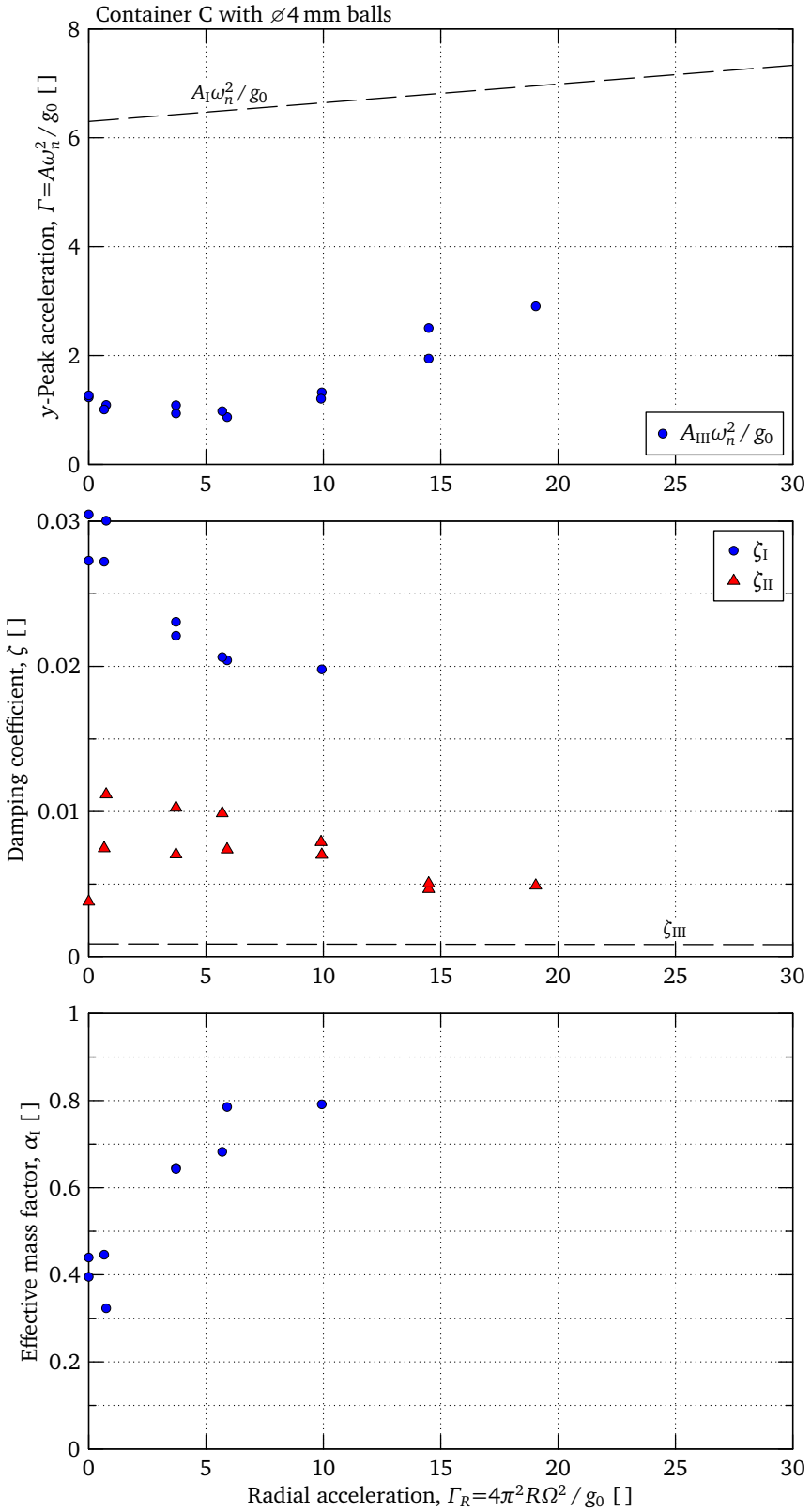

Figure A.7. Test result for container C with ⌀4 mm balls

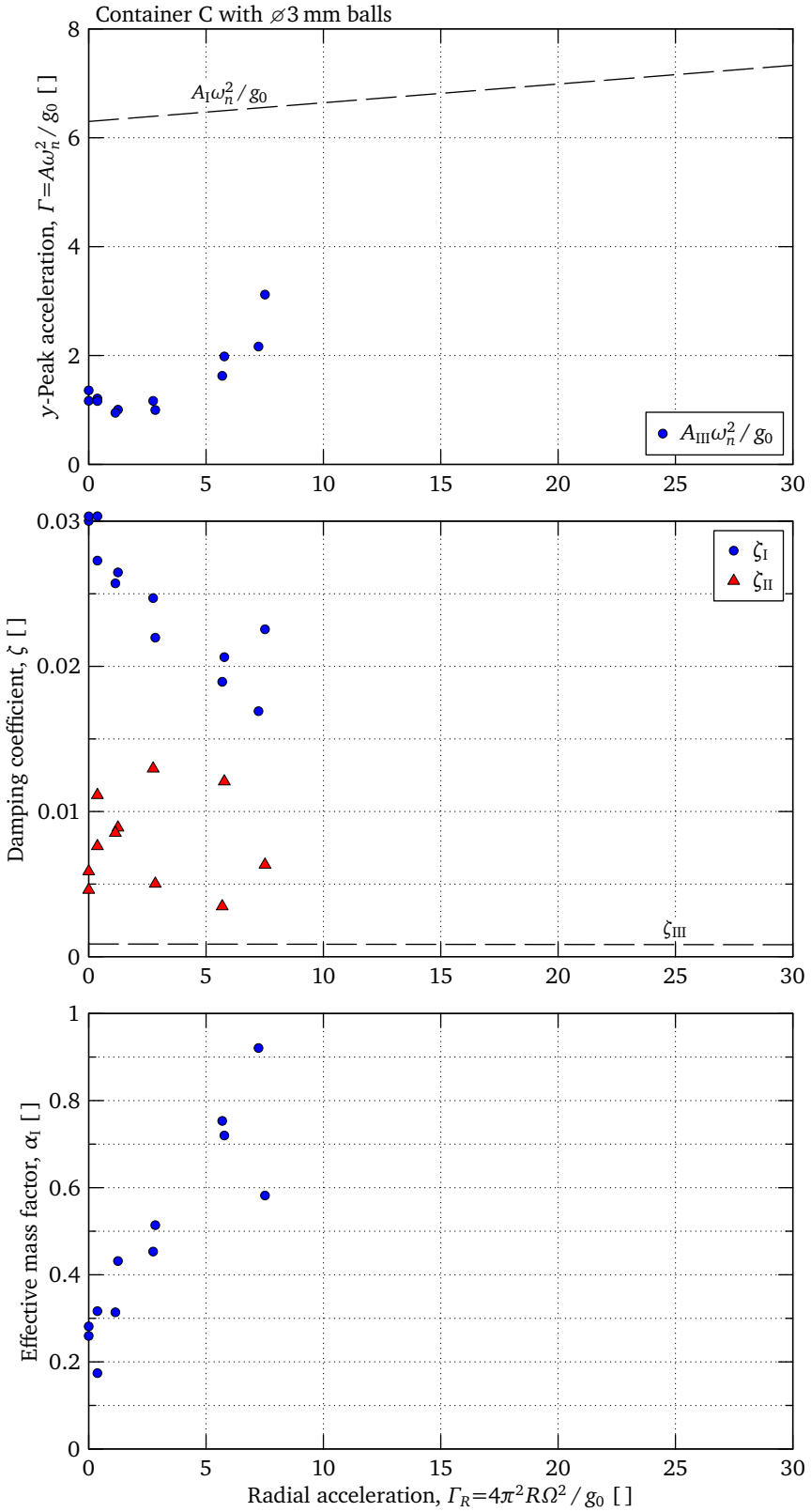

Figure A.8. Test result for container C with ⌀3 mm balls

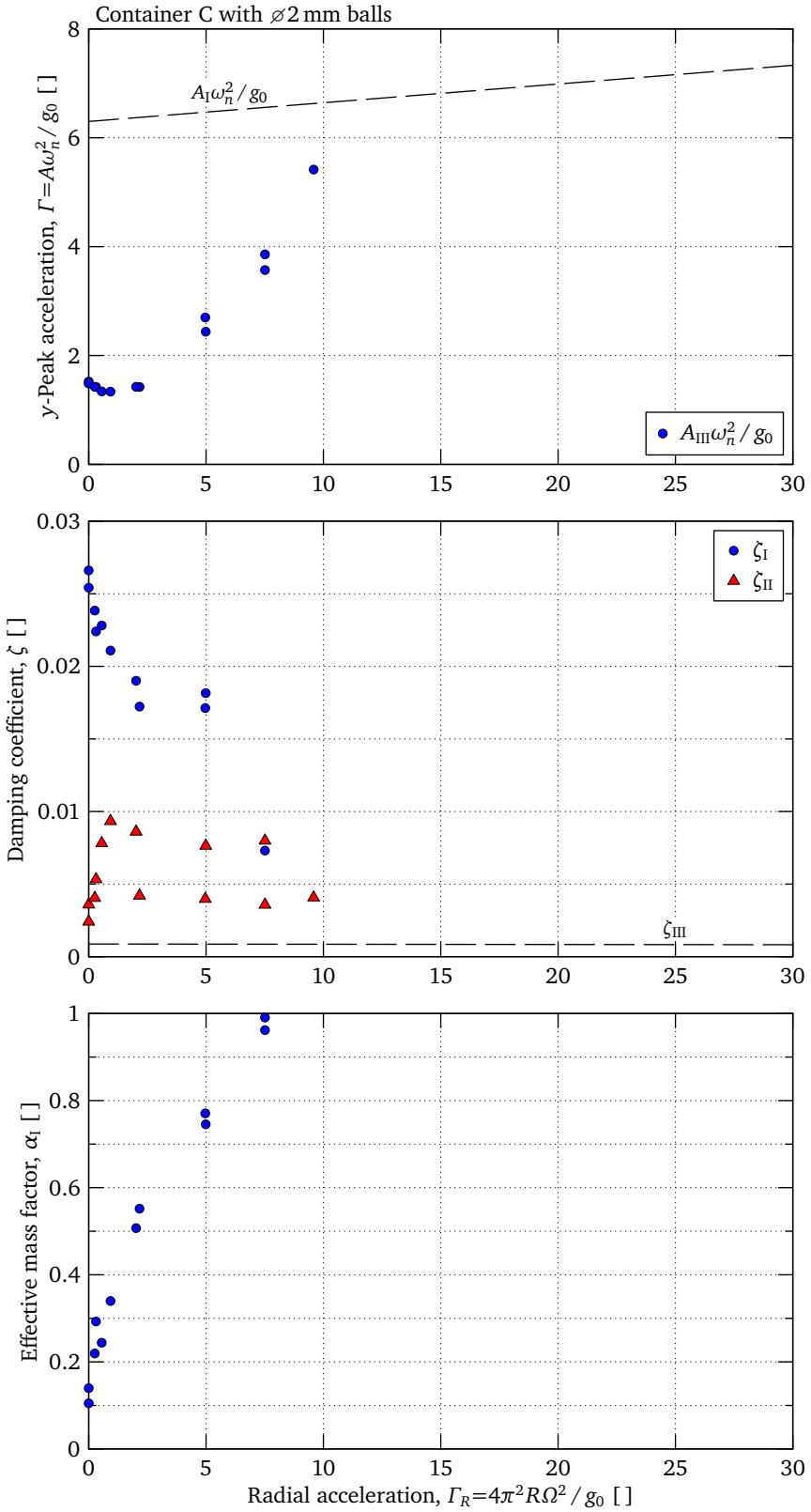

Figure A.9. Test result for container C with ⌀2 mm balls

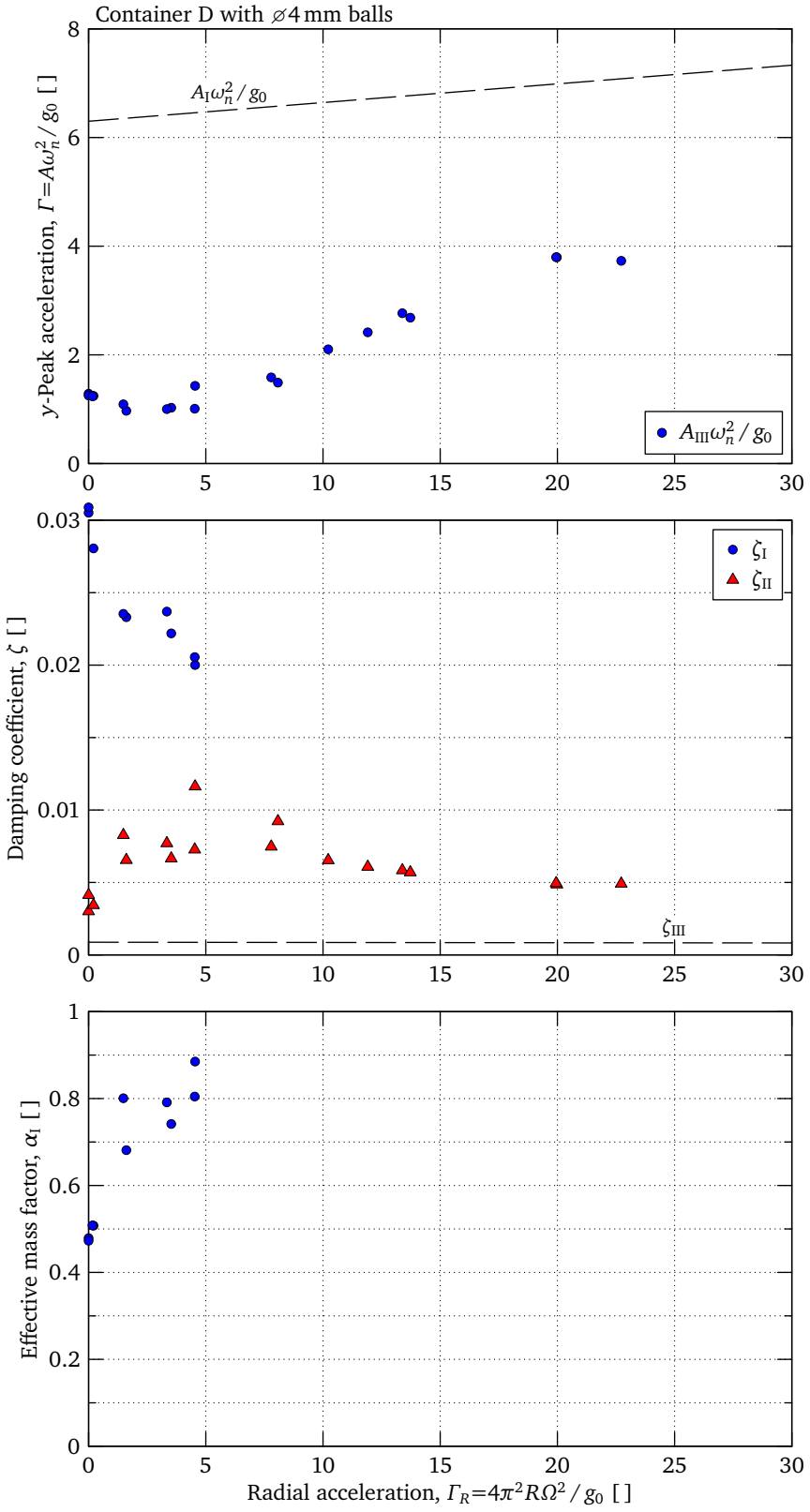

Figure A.10. Test result for container D with ⌀4 mm balls

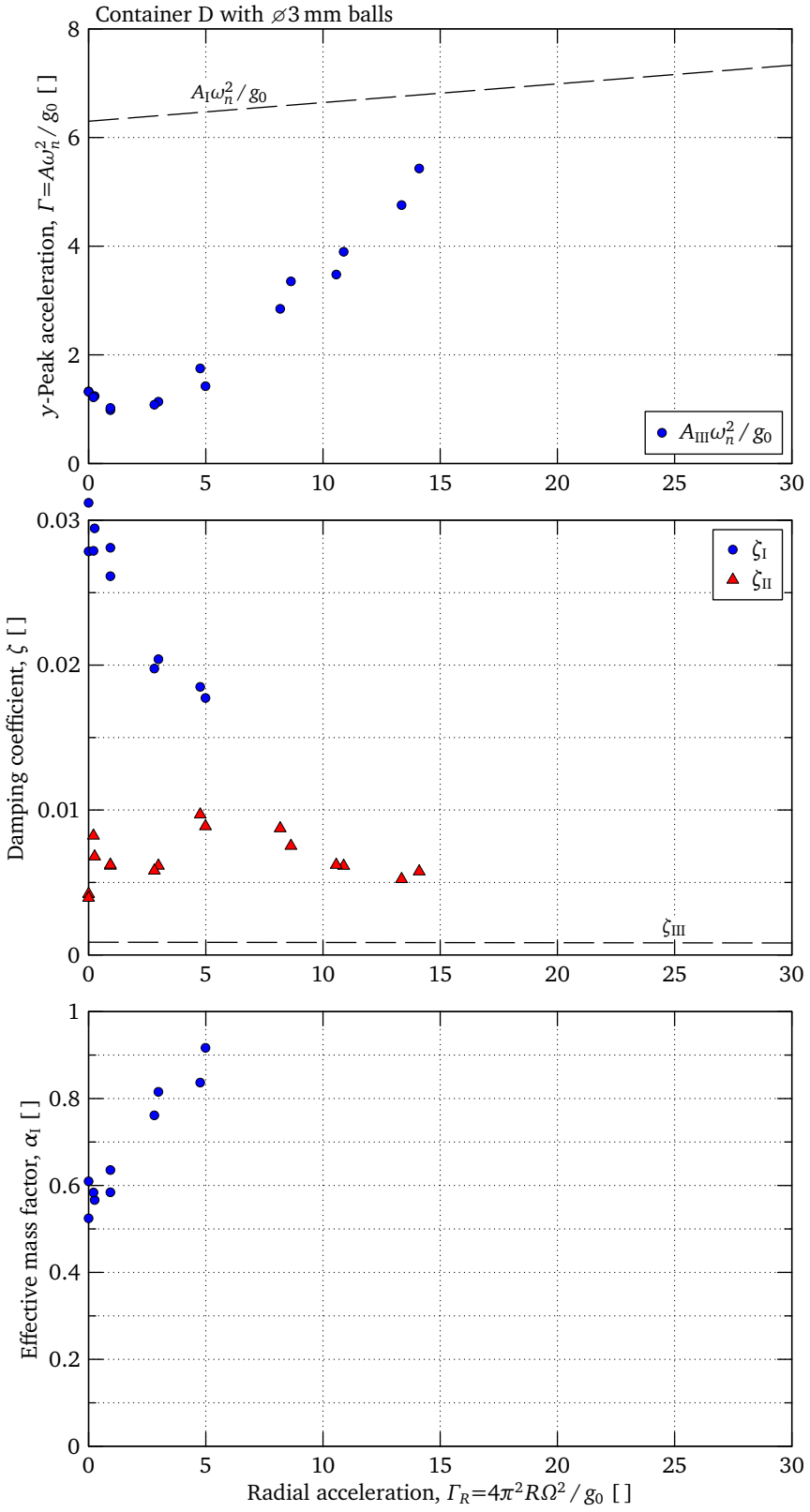

Figure A.11. Test result for container D with ⌀3 mm balls

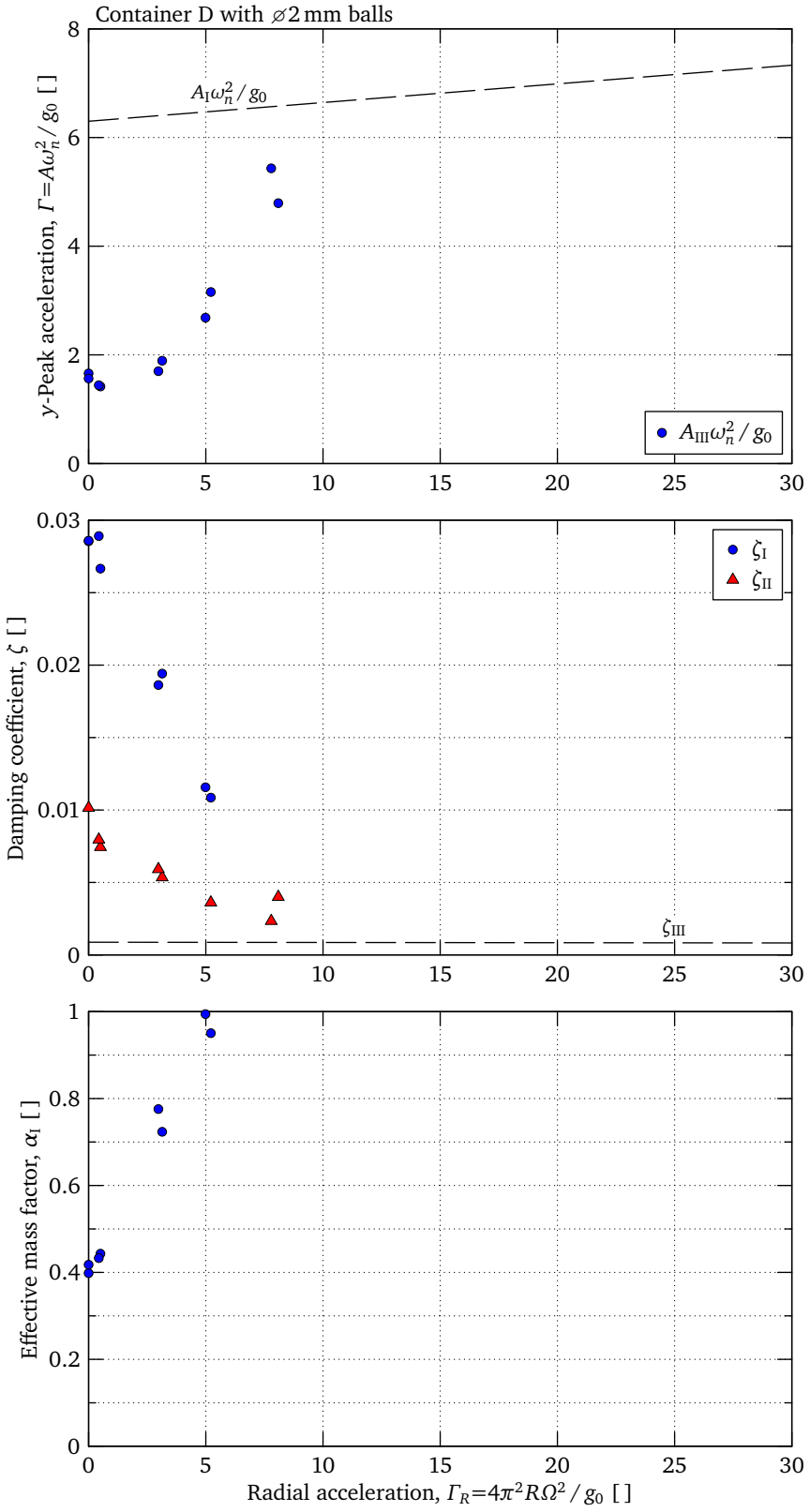

Figure A.12. Test result for container D with ⌀2 mm balls

Appendix

B

DEM Simulation Results

List of symbols for appendix B

Constants

$g_0 = 9.81\,\mathrm{m/s^2}$	standard gravitational acceleration
$R = 0.4\,\mathrm{m}$	rotation radius

Variables

A	amplitude of oscillations	[m]
m_e	equivalent beam mass (eqn. 3.10)	[kg]
m_p	average total particle mass	[kg]
M_e	equivalent tip container mass (eqn. 4.2)	[kg]
r_m	mass ratio, $r_m = m_p / M_e$	[kg]
t	time	[s]
α	fraction of the particle contributing towards the total mass	[−]
Γ	peak acceleration amplitude factor, $\Gamma = A\omega^2 / g_0$	[−]
Γ_R	centrifugal acceleration factor, $\Gamma_R = R(2\pi\Omega)^2 / g_0$	[−]
ω_n	natural frequency, $\omega_n = \sqrt{k/m}$	[rad/s]
Ω	system rotation velocity	[$\mathrm{s^{-1}}$]
ζ	viscous damping factor, $\zeta = c/(2m\omega_n)$	[−]

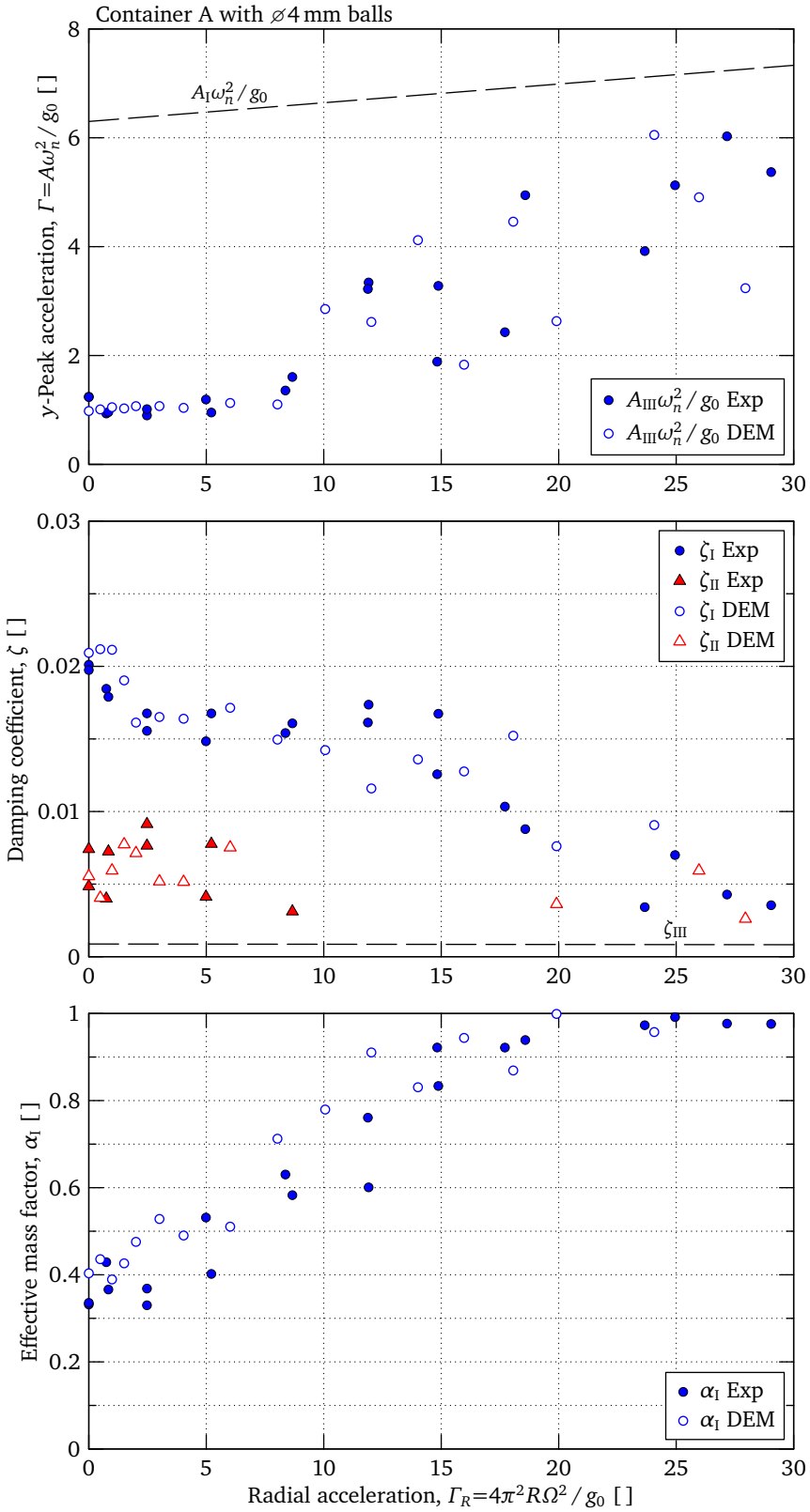

Figure B.1. DEM simulation result for container A with ⌀4 mm balls

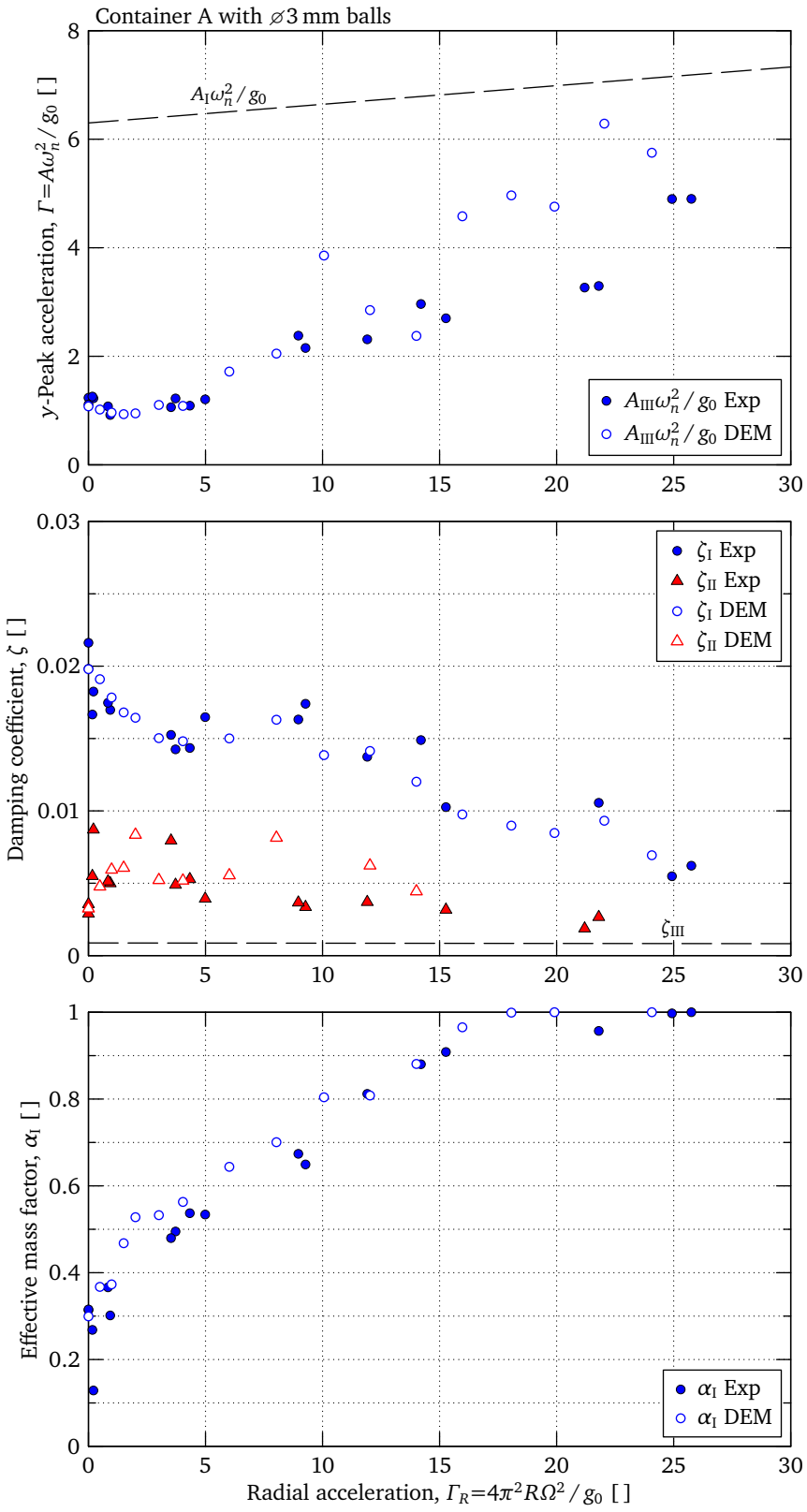

Figure B.2. DEM simulation result for container A with ⌀3 mm balls

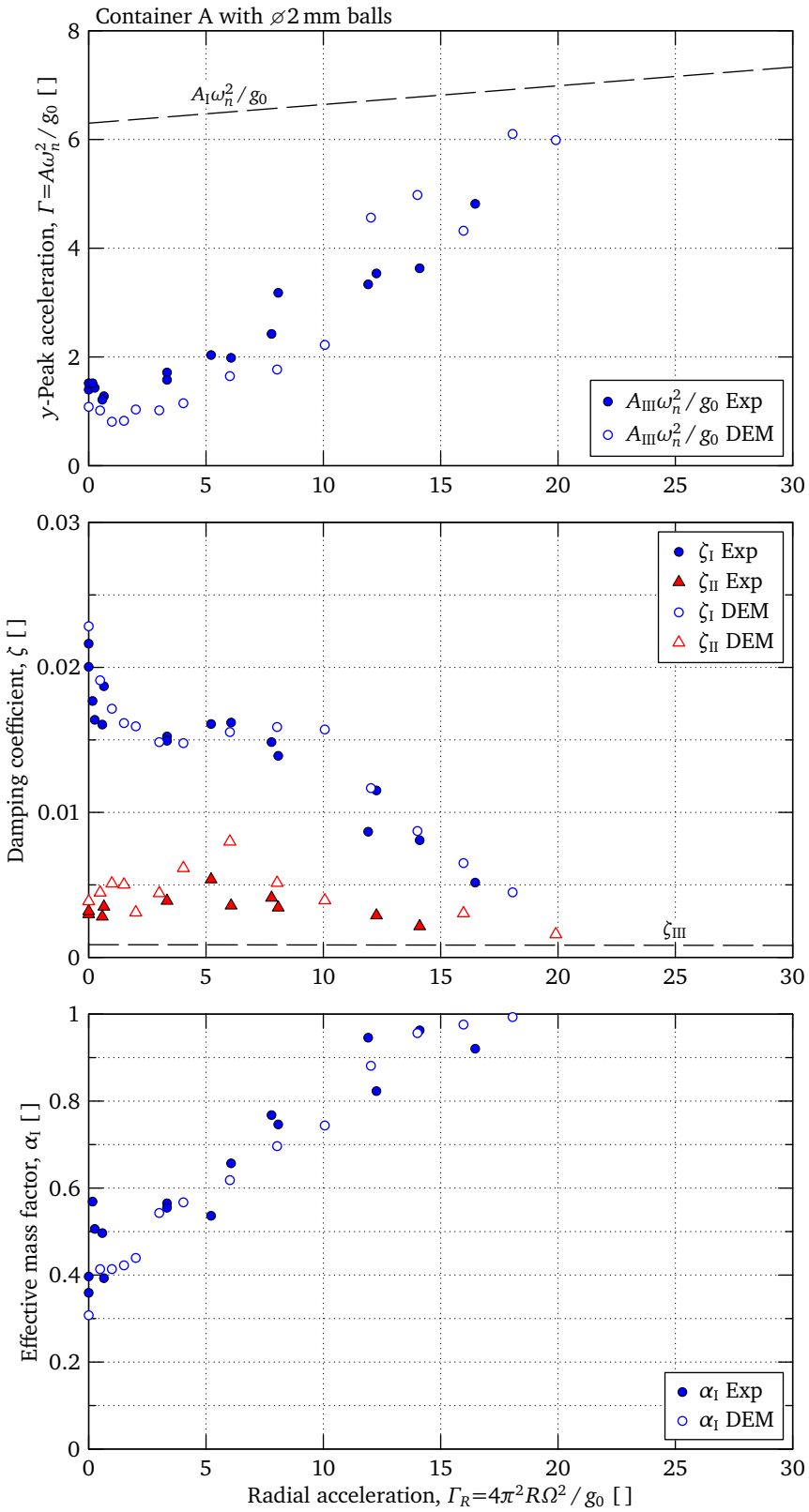

Figure B.3. DEM simulation result for container A with ⌀2 mm balls

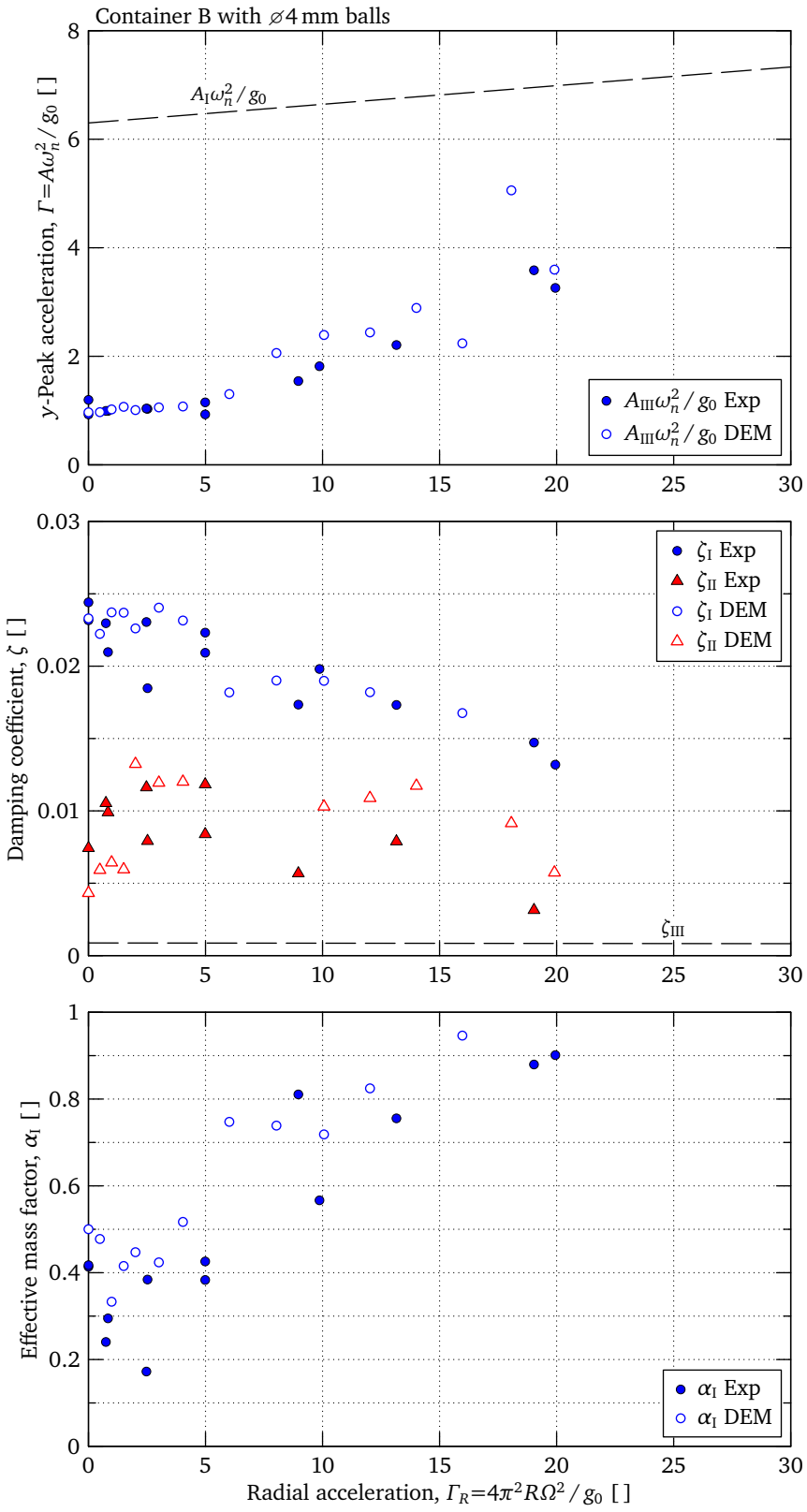

Figure B.4. DEM simulation result for container B with ⌀4 mm balls

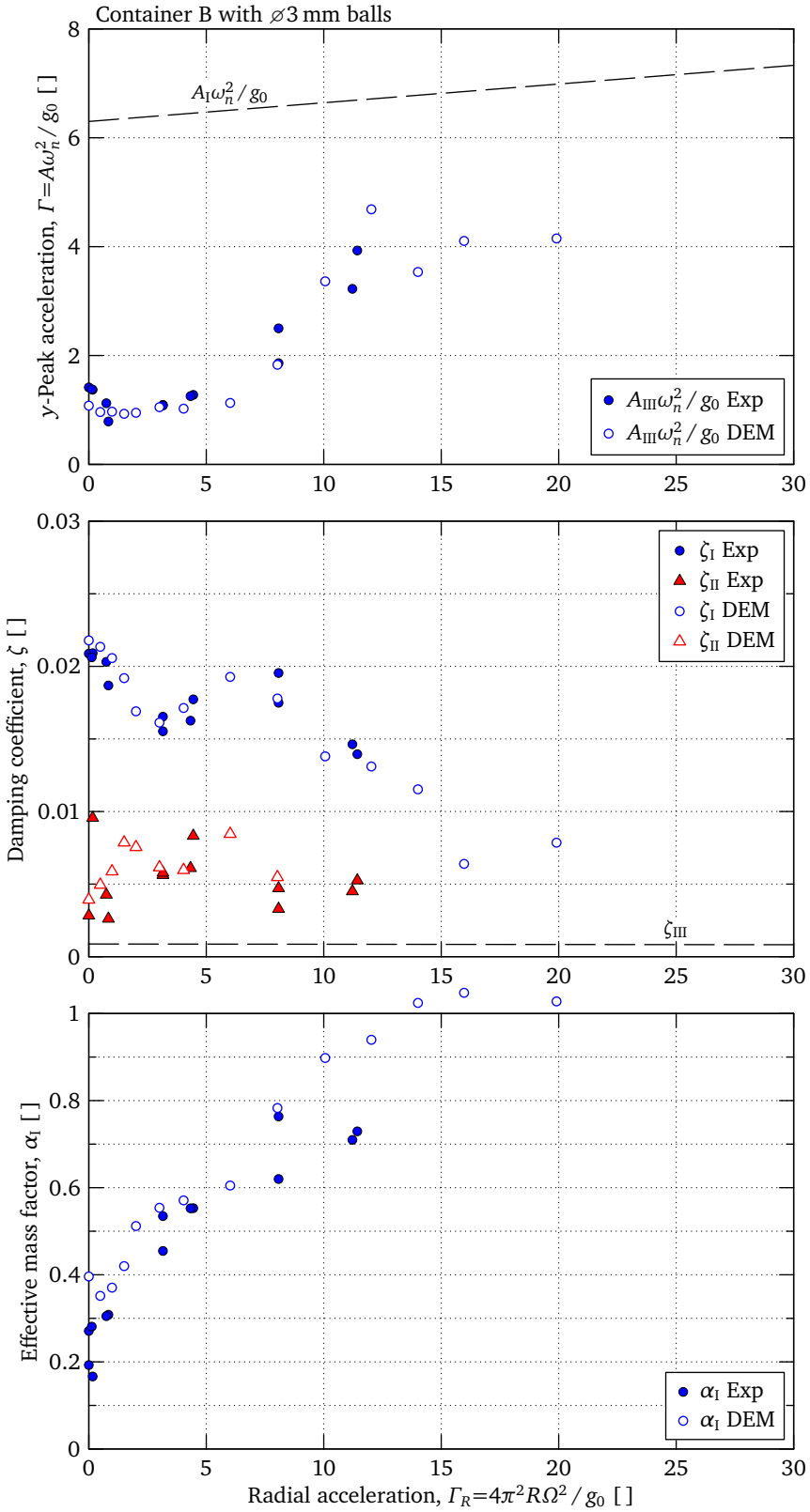

Figure B.5. DEM simulation result for container B with ⌀3 mm balls

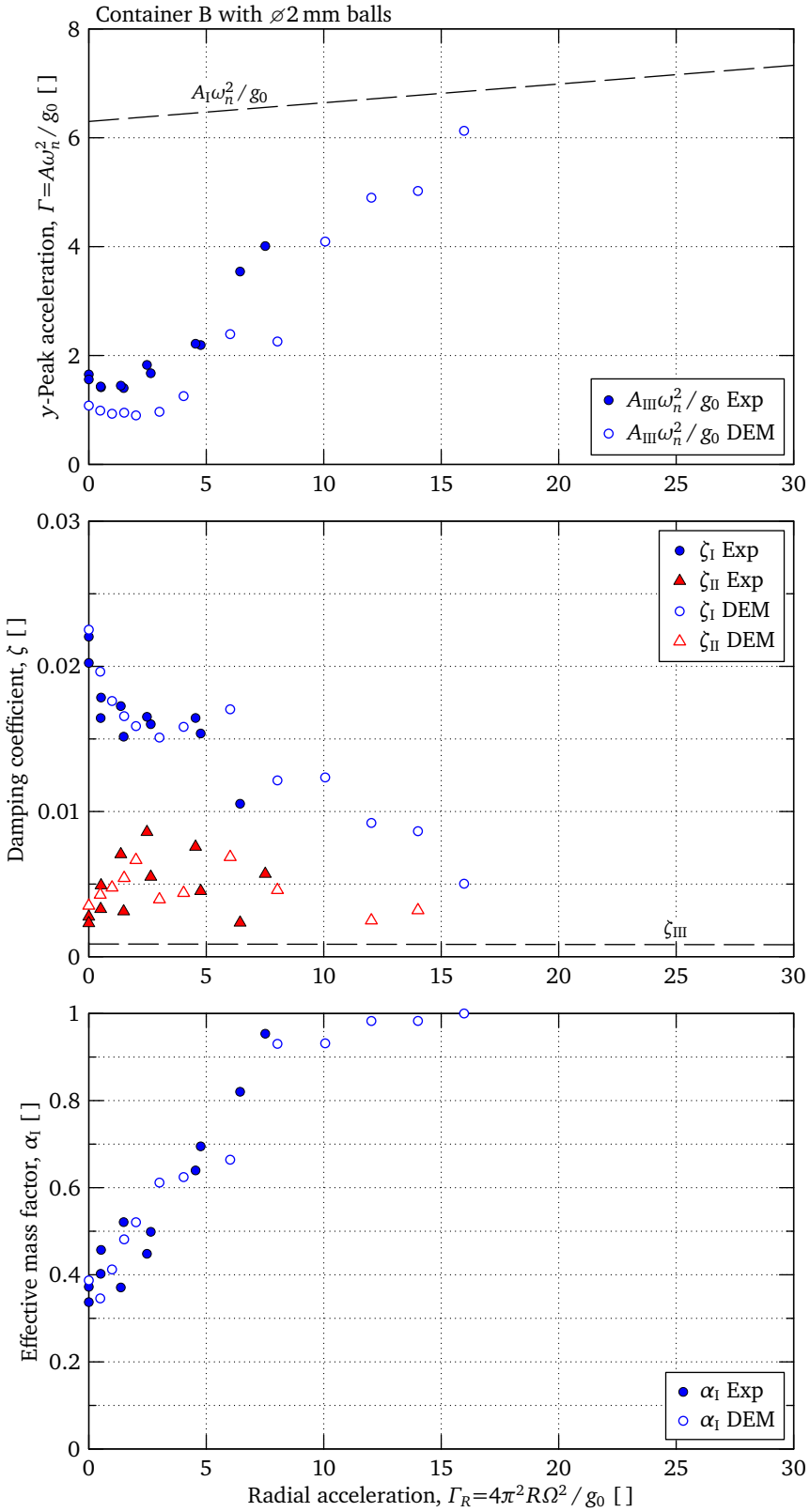

Figure B.6. DEM simulation result for container B with ⌀2 mm balls

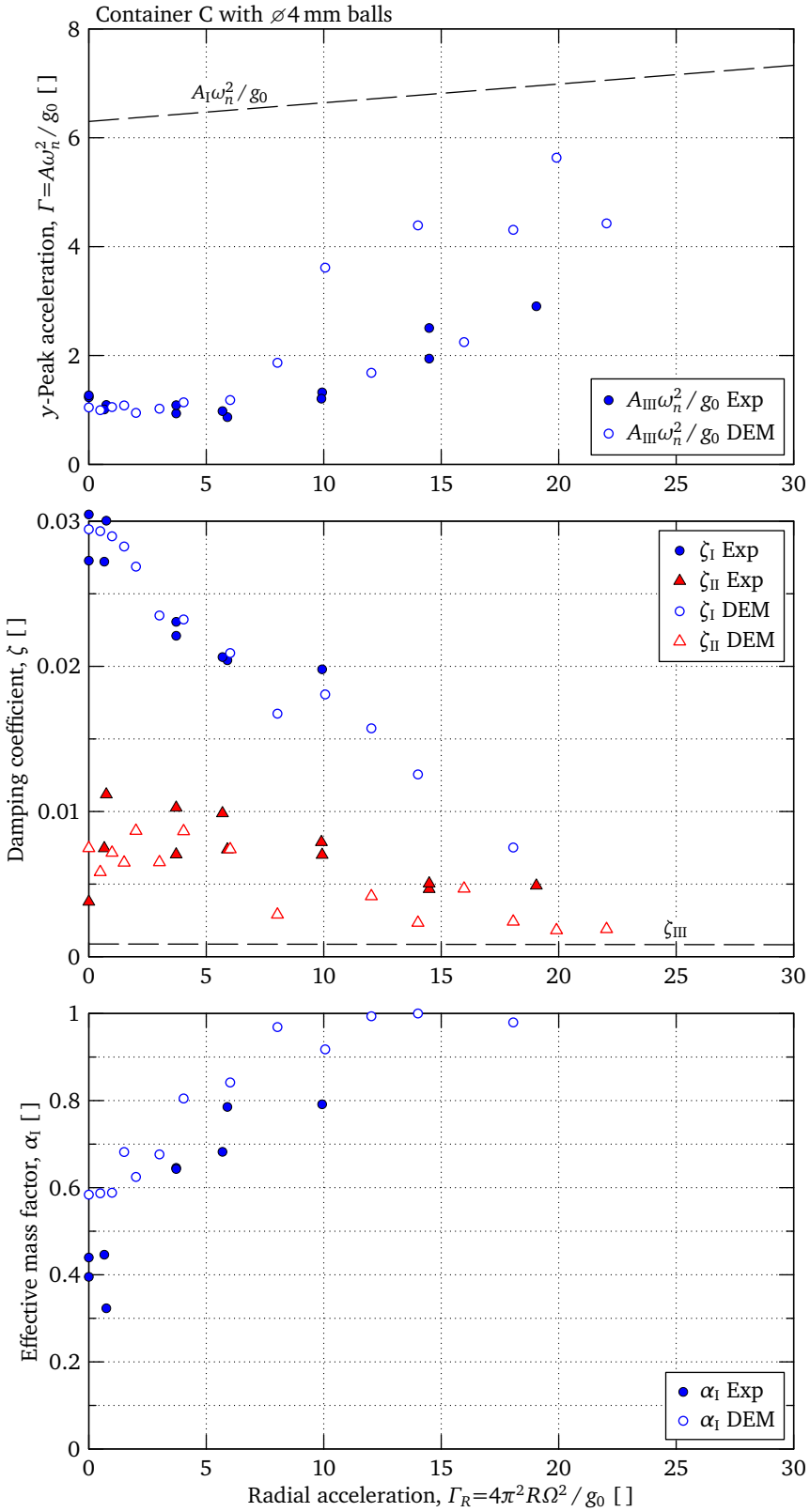

Figure B.7. DEM simulation result for container C with ⌀4 mm balls

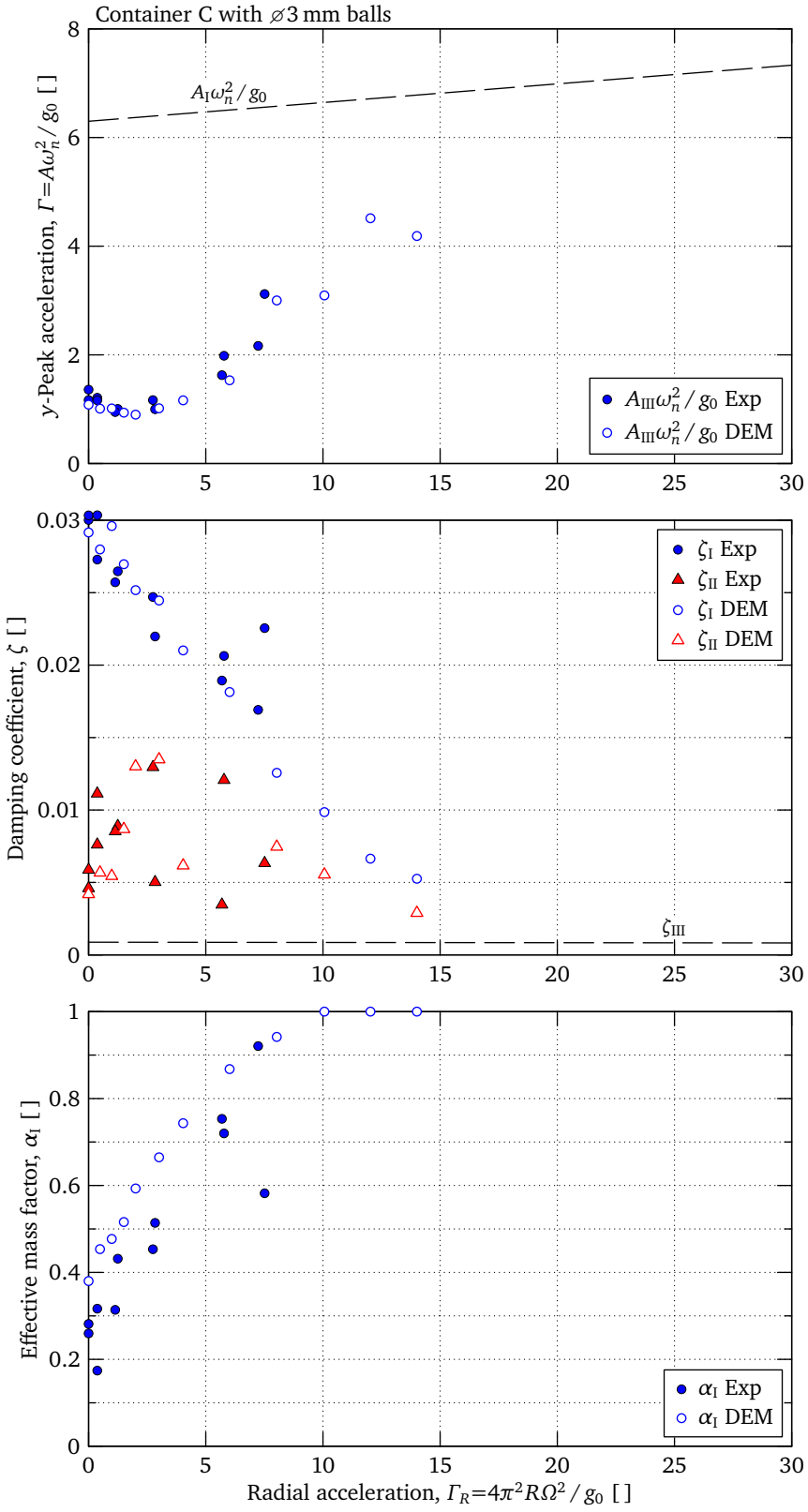

Figure B.8. DEM simulation result for container C with ⌀3 mm balls

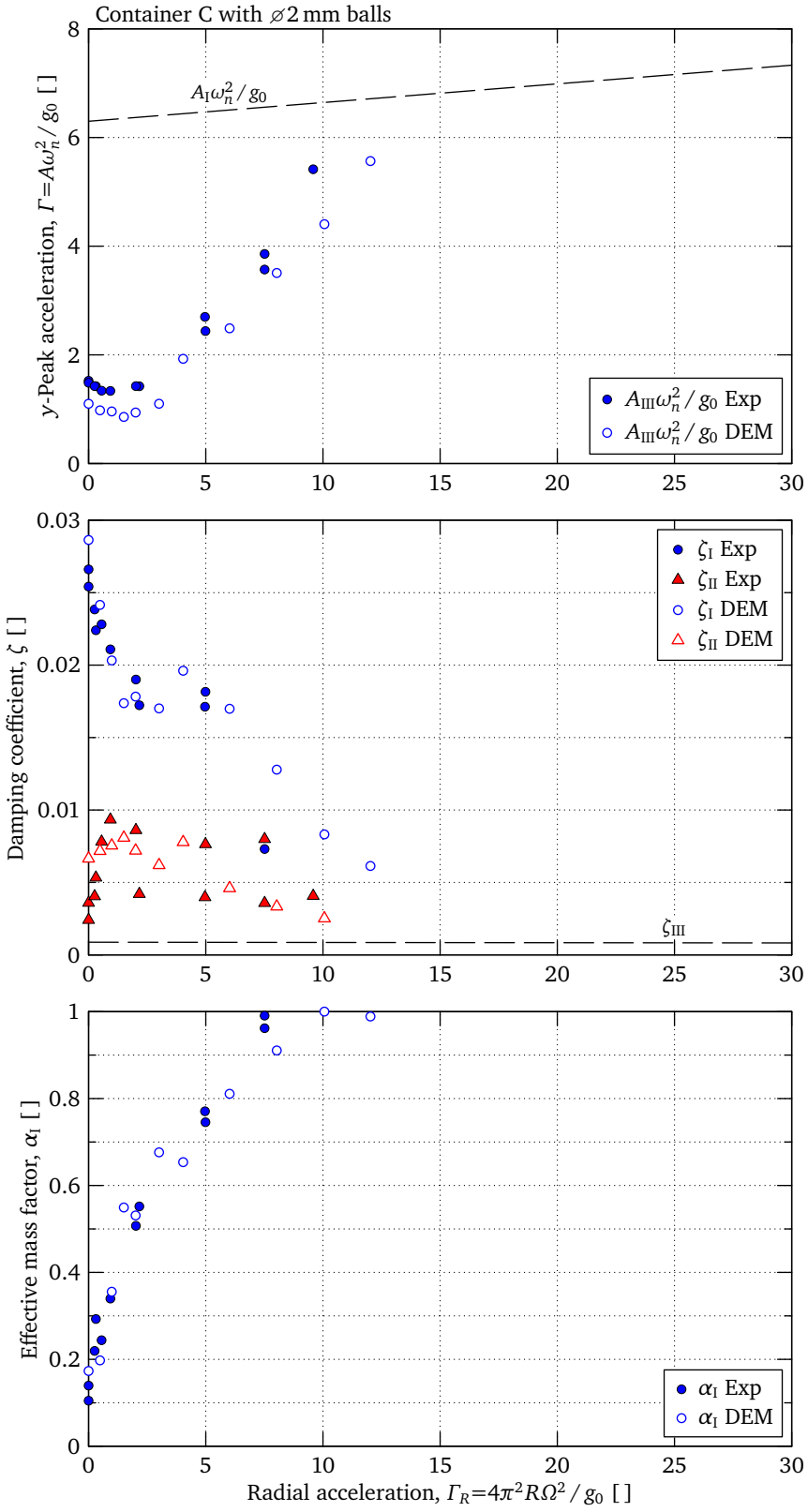

Figure B.9. DEM simulation result for container C with ⌀2 mm balls

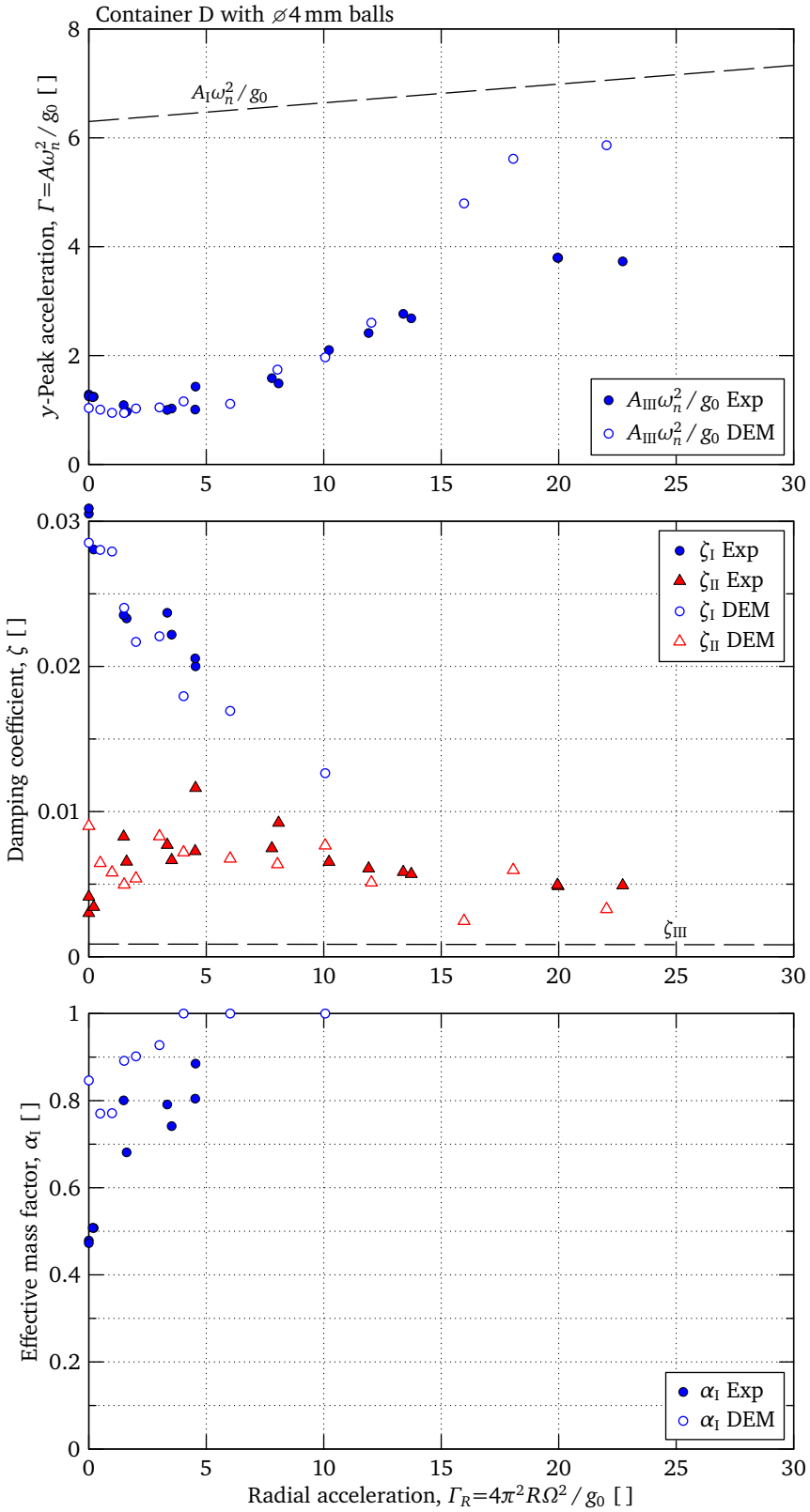

Figure B.10. DEM simulation result for container D with ⌀4 mm balls

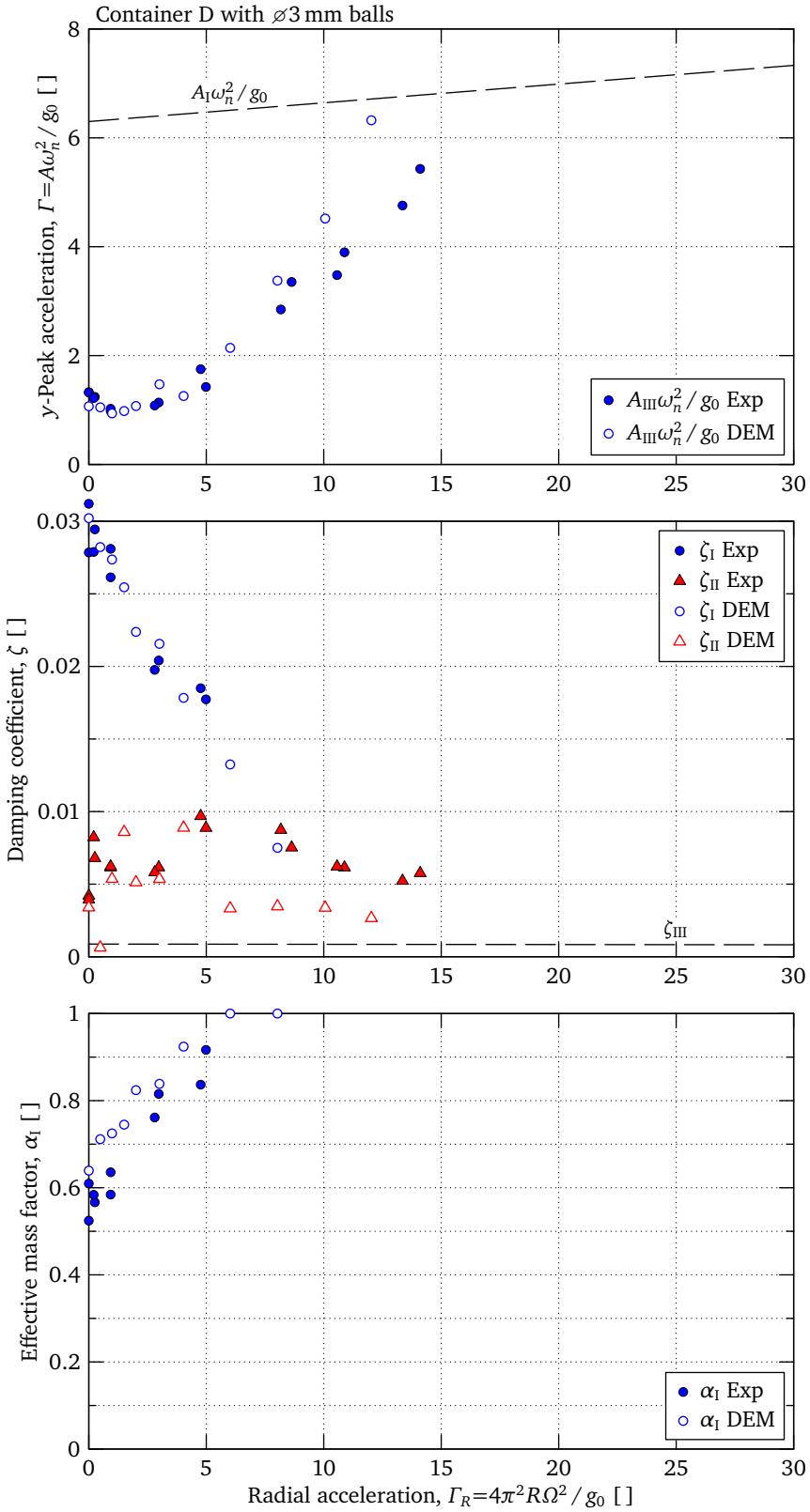

Figure B.11. DEM simulation result for container D with ⌀3 mm balls

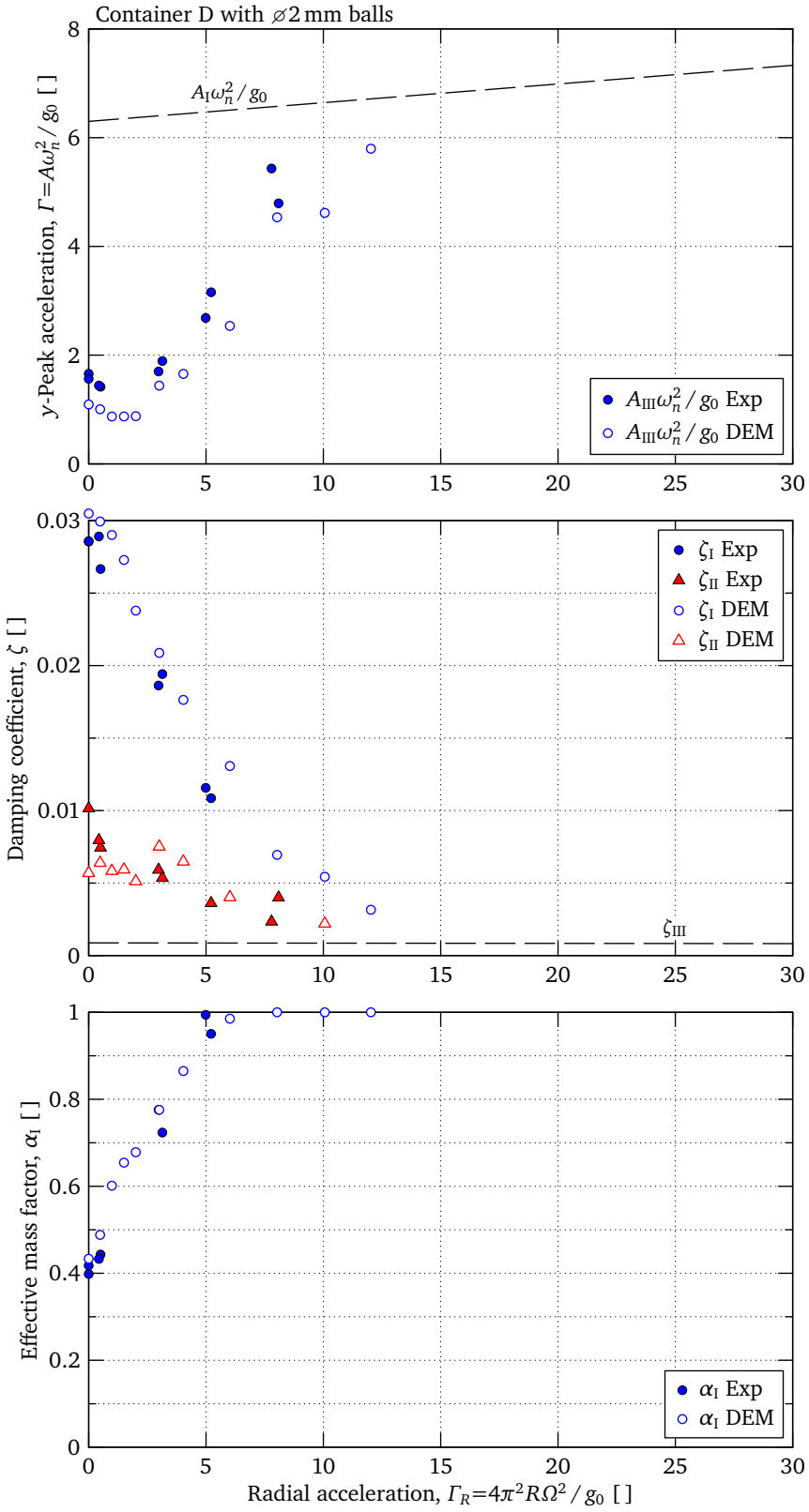

Figure B.12. DEM simulation result for container D with ⌀2 mm balls

Appendix

C

Vibration Response of a Single Degree of Freedom System

List of symbols for appendix C

c	damping coefficient (fig. C.1)	[N·s/m]
C	constant of integration (eqn. C.12)	[m]
k	spring stiffness (fig. C.1)	[N/m]
i, j	indices	
m	mass (fig. C.1)	[kg]
p	number of base oscillation modes	
r_j	base oscillation frequency ratio (eqn. C.8)	[−]
t	time	[s]
u	base oscillation displacement (fig. C.1)	[m]
U_j	base oscillation amplitude (eqn. C.1)	[m]
y	beam tip displacement (fig. C.1)	[m]
y_0	beam tip displacement at $t = 0$	[m]
$\dot{y}_0$	beam tip velocity at $t = 0$	[m/s]
y_h	homogeneous solution (eqn. C.9)	[m]
y_offs	beam tip displacement offset (eqn. C.9)	[m]
y_p	particular solution (eqn. C.9)	[m]
Y_j	base oscillation magnifier (eqn. C.13)	[−]
θ	phase angle (eqn. C.12)	[rad]
ϕ_j	base oscillation phase angle (eqn. C.13)	[rad]
Φ_j	base oscillation offset phase (eqn. C.1)	[rad]
ζ	viscous damping factor (eqn. C.6)	[−]
ω_d	damped natural frequency (eqn. C.11)	[rad/s]
ω_n	natural frequency (eqn. C.5)	[rad/s]
Ω_j	base oscillation frequency (eqn. C.1)	[rad/s]

C.1 Introduction

When the experimental equipment was designed, it was intended to measure the vibrational response of the force-free decay of a beam after it was displaced a certain distance y_0 and the released. Although great care was taken to balance the equipment and pre-tension the bearings, it was found during physical vibration measurements that the rotation of the equipment did induce a forced vibration on the beam.

In the following analysis the response of a system with harmonic base excitation will be considered to take into account the effect of the equipment.

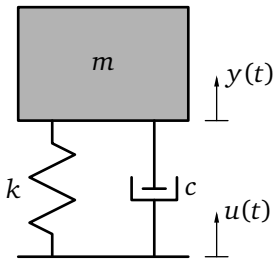

Figure C.1. Schematic of a damped single SDOF system with base excitation.

C.2 Viscously damped single degree of freedom systems

With reference to figure C.1, consider a damped single degree of freedom (SDOF) system acted on by an oscillating base support. The base oscillates with P different modes superimposed on each other. The base displacement u as a function of time is then

$$u(t) = \sum_{j=0}^{P} U_j \sin(\Omega_j t + \Phi_j), \tag{C.1}$$

with Ω_j the frequencies of the base oscillation modes, Φ_j the phase angles and U_j the amplitudes of displacement.

The equation of motion of mass m is then

$$m\ddot{y} + c(\dot{y} - \dot{u}) + k(y - u) = 0, \tag{C.2}$$

with c the coefficient of viscous damping and k the spring constant. Inserting equation (C.1) into (C.2) gives

$$m\ddot{y} + c\dot{y} + ky = c\sum_{j=0}^{P} \Omega_j U_j \cos(\Omega_j t + \Phi_j) + k\sum_{j=0}^{P} U_j \sin(\Omega_j t + \Phi_j) \tag{C.3}$$

It is customary to rewrite equation (C.3) in the following convenient form:

$$\ddot{y} + 2\zeta\omega_n\dot{y} + \omega_n^2 y = \omega_n^2 \sum_{j=0}^{P} U_j \sqrt{1+4\zeta^2 r_j^2}\, \cos(\Omega_j t + \Phi_j - \phi_j') \tag{C.4}$$

with

$$\omega_n = \sqrt{k/m} \qquad \text{natural frequency of the undamped system,} \tag{C.5}$$

$$\zeta = c/(2m\omega_n) \qquad \text{viscous damping factor,} \tag{C.6}$$

$$\phi'_j = \tan^{-1}\left(\frac{1}{2\zeta r_j}\right) \qquad \text{force function phase angle,} \tag{C.7}$$

$$r_j = \Omega_j/\omega_n \qquad \text{frequency ratio.} \tag{C.8}$$

Equation (C.4) can be solved in terms of a homogeneous (transient) response $y_{\mathrm{h}}(t)$ with $\ddot{y}+2\zeta\omega_n\dot{y}+\omega_n^2 y = 0$ and a particular (steady-state) response $y_{\mathrm{p}}(t)$. The total response is then

$$y(t) = y_{\mathrm{offs}} + y_{\mathrm{h}}(t) + y_{\mathrm{p}}(t). \tag{C.9}$$

with y_{offs} a constant offset introduced to fit experimental data.

We are interested in an under-damped system where $0<\zeta<1$. The solution of equation (C.4) for this case (e.g. Meirovitch, 2001, pp. 91 and 128) is

$$y_{\mathrm{h}}(t) = C\,\mathrm{e}^{-\zeta\omega_n t}\cos(\omega_d t - \theta)\,, \tag{C.10a}$$

$$y_{\mathrm{p}}(t) = \sum_{j=0}^{P} U_j Y_j \cos\left(\Omega_j t + \Phi_j - \phi_j\right), \tag{C.10b}$$

with the frequency of damped vibration

$$\omega_d = \sqrt{1-\zeta^2}\,\omega_n \tag{C.11}$$

and the constants C and Y_i and phase angles θ and ψ_i which depend on the initial conditions, y_0 and $\dot{y}_0$, and parameters ω_n, ζ and Ω_i.

$$C = \left[y_0^2 + \left(\frac{\zeta\omega_n y_0 + \dot{y}_0}{\omega_d}\right)^2\right]^{1/2} \qquad \theta = \tan^{-1}\left(\frac{\zeta\omega_n y_0 + \dot{y}_0}{\omega_d y_0}\right) \tag{C.12}$$

$$Y_j = \left[\frac{1+\left(2\zeta r_j\right)^2}{\left(1-r_j^2\right)^2 + \left(2\zeta r_j\right)^2}\right]^{1/2} \qquad \phi_j = \tan^{-1}\left(\frac{1-r_j^2+(2\zeta r_j)^2}{2\zeta r_j^3}\right) \tag{C.13}$$

Appendix

D

Estimation of Vibration Parameters

List of symbols for appendix D

C	constant of integration (eqn. C.12)	[m]
i, j, k	indices	
$\underline{\overline{J}}$	Jacobian (eqn. D.7)	
N	number of data points	
p	number of base oscillation modes	
r_j	base oscillation frequency ratio (eqn. C.8)	[−]
t	time	[s]
U_j	base oscillation amplitude (eqn. C.1)	[m]
y	beam tip displacement (fig. C.1)	[m]
y_h	homogeneous solution (eqn. C.9)	[m]
y_offs	beam tip displacement offset (eqn. C.9)	[m]
y_p	particular solution (eqn. C.9)	[m]
Y_j	base oscillation magnifier (eqn. C.13)	[−]
$\alpha_i, \overline{\boldsymbol{\alpha}}$	variable and vector of variables to optimise	
ϵ	error function (eqn. D.4)	
$\varrho_i, \overline{\boldsymbol{\varrho}}$	residue (eqn. D.3)	
λ	weighing factor for stability, (eqn. D.11)	
θ	phase angle (eqn. C.12)	[rad]
ϕ_j	base oscillation phase angle (eqn. C.13)	[rad]
Φ_j	base oscillation offset phase (eqn. C.1)	[rad]
ζ	viscous damping factor (eqn. C.6)	[−]
ω_d	damped natural frequency (eqn. C.11)	[rad / s]
ω_n	natural frequency (eqn. C.5)	[rad / s]
Ω_j	base oscillation frequency (eqn. C.1)	[rad / s]

D.1 Least squares formulation

From the experimental measurements, a set of N discrete data points of the tip displacement y_i at time step t_i for $i = 0, 1, \ldots, N$, was obtained for every test. The expected theoretical displacement at time t_i is given by the total response, equation (C.9)

$$y(t_i) = y_{\text{offs}} + C\,\mathrm{e}^{-\zeta\omega_n t_i}\cos\left(\sqrt{1-\zeta^2}\,\omega_n t_i - \theta\right) + \sum_{j=0}^{p} U_j Y_j \cos\left(\Omega_j t_i + \Phi_j - \phi_j\right). \quad \text{(D.1)}$$

The objective is to obtain the best fit for equation (D.1) through the set of experimental data points. It is accomplished by finding the parameters y_{offs}, C, ω_n, ζ, θ, $U_0, \ldots, U_p$, and $\Phi_0, \ldots, \Phi_p$ that will minimise the difference between the theoretical response and the discrete data points.

Defining a variable vector $\overline{\boldsymbol{\alpha}}$ of length $(4+2p)$ containing the above mentioned parameters

$$\overline{\boldsymbol{\alpha}} = [y_{\text{offs}},\, C,\, \omega_n,\, \zeta,\, \theta,\, U_0, \ldots, U_p,\, \Phi_0, \ldots, \Phi_p]^{\mathsf{T}}. \quad \text{(D.2)}$$

The difference or residue between equation (D.1) and the discrete data points t_i and y_i, in terms of $\overline{\boldsymbol{\alpha}}$, is

$$\varrho_i(\overline{\boldsymbol{\alpha}}) = y_i - y(t_i, \overline{\boldsymbol{\alpha}}). \quad \text{(D.3)}$$

Define the function of total error in a least squares fashion

$$\epsilon(\overline{\boldsymbol{\alpha}}) = \frac{1}{2}\sum_{i=0}^{N}\left[\varrho_i(\overline{\boldsymbol{\alpha}})\right]^2 \quad \text{(D.4)}$$

Equation (D.4) has a stationary value if

$$\nabla\epsilon(\overline{\boldsymbol{\alpha}}) = \sum_{i=0}^{N}\nabla\varrho_i(\overline{\boldsymbol{\alpha}})\,\varrho_i(\overline{\boldsymbol{\alpha}}) = \left[\underline{\overline{\boldsymbol{J}}}(\overline{\boldsymbol{\alpha}})\right]^{\mathsf{T}}\cdot\overline{\boldsymbol{\varrho}}(\overline{\boldsymbol{\alpha}}) = \overline{\mathbf{0}}. \quad \text{(D.5)}$$

with $\overline{\mathbf{0}}$, the null vector, $\nabla\varrho_i = \partial\varrho_i/\partial\alpha_k$ with $k = 0, 1, \ldots, 4+2p$, and

$$\overline{\boldsymbol{\varrho}}\left(\overline{\boldsymbol{\alpha}}\right) = \begin{bmatrix} y_0 - y\left(t_0, \overline{\boldsymbol{\alpha}}\right) \\ y_1 - y\left(t_1, \overline{\boldsymbol{\alpha}}\right) \\ \vdots \\ y_N - y\left(t_N, \overline{\boldsymbol{\alpha}}\right) \end{bmatrix}. \quad \text{(D.6)}$$

The Jacobian is the $(N \times 4+2p)$ matrix

$$\underline{\overline{\boldsymbol{J}}}\left(\overline{\boldsymbol{\alpha}}\right) = -\begin{bmatrix} \dfrac{\partial y\left(t_0, \overline{\boldsymbol{\alpha}}\right)}{\partial\alpha_0} & \dfrac{\partial y\left(t_0, \overline{\boldsymbol{\alpha}}\right)}{\partial\alpha_1} & \cdots & \dfrac{\partial y\left(t_0, \overline{\boldsymbol{\alpha}}\right)}{\partial\alpha_{4+2p}} \\ \dfrac{\partial y\left(t_1, \overline{\boldsymbol{\alpha}}\right)}{\partial\alpha_0} & \dfrac{\partial y\left(t_1, \overline{\boldsymbol{\alpha}}\right)}{\partial\alpha_1} & \cdots & \dfrac{\partial y\left(t_1, \overline{\boldsymbol{\alpha}}\right)}{\partial\alpha_{4+2p}} \\ \vdots & \vdots & \ddots & \vdots \\ \dfrac{\partial y\left(t_N, \overline{\boldsymbol{\alpha}}\right)}{\partial\alpha_0} & \dfrac{\partial y\left(t_N, \overline{\boldsymbol{\alpha}}\right)}{\partial\alpha_1} & \cdots & \dfrac{\partial y\left(t_N, \overline{\boldsymbol{\alpha}}\right)}{\partial\alpha_{4+2p}} \end{bmatrix}. \quad \text{(D.7)}$$

D.2 Levenberg-Marquardt algorithm

Equation (D.5) can be solved iteratively for $\overline{\boldsymbol{\alpha}}$ with Newton's method for a system of non-linear equations. Expand equation (D.5) for a small perturbation $\delta\overline{\boldsymbol{\alpha}}$ with a Taylor series around the current value $\overline{\boldsymbol{\alpha}}_k$ so that $\overline{\boldsymbol{\alpha}}_{k+1} = \overline{\boldsymbol{\alpha}}_k + \delta\overline{\boldsymbol{\alpha}}$. Then

$$\nabla\epsilon(\overline{\boldsymbol{\alpha}}_{k+1}) = \nabla\epsilon(\overline{\boldsymbol{\alpha}}_k) + \nabla^2\epsilon(\overline{\boldsymbol{\alpha}}_k)\cdot\left[\overline{\boldsymbol{\alpha}}_{k+1} - \overline{\boldsymbol{\alpha}}_k\right] + \cdots \tag{D.8}$$

Ignoring higher order terms (approximate functions as quadratic) and taking the left hand side of the equation as near zero, Newton's update scheme becomes

$$\overline{\boldsymbol{\alpha}}_{k+1} = \overline{\boldsymbol{\alpha}}_k - \left[\nabla^2\epsilon(\overline{\boldsymbol{\alpha}}_k)\right]^{-1}\cdot\nabla\epsilon(\overline{\boldsymbol{\alpha}}_k). \tag{D.9}$$

The Hessian is

$$\begin{aligned}\nabla^2\epsilon(\overline{\boldsymbol{\alpha}}) &= \left[\underline{\overline{\boldsymbol{J}}}(\overline{\boldsymbol{\alpha}})\right]^{\mathsf{T}}\cdot\underline{\overline{\boldsymbol{J}}}(\overline{\boldsymbol{\alpha}}) + \sum_{i=0}^{N}\nabla^2\varrho_i(\overline{\boldsymbol{\alpha}})\,\varrho_i(\overline{\boldsymbol{\alpha}}) \\ &\approx \left[\underline{\overline{\boldsymbol{J}}}(\overline{\boldsymbol{\alpha}})\right]^{\mathsf{T}}\cdot\underline{\overline{\boldsymbol{J}}}(\overline{\boldsymbol{\alpha}})\end{aligned} \tag{D.10}$$

where it was assumed that ϱ_i is near linear and small in the vicinity of the optimum.

The Levenberg-Marquardt algorithm redefines equation (D.10) to be more robust and stable as

$$\nabla^2\epsilon(\overline{\boldsymbol{\alpha}}) = \left[\underline{\overline{\boldsymbol{J}}}(\overline{\boldsymbol{\alpha}})\right]^{\mathsf{T}}\cdot\underline{\overline{\boldsymbol{J}}}(\overline{\boldsymbol{\alpha}}) + \lambda\,\mathrm{diag}\left(\left[\underline{\overline{\boldsymbol{J}}}(\overline{\boldsymbol{\alpha}})\right]^{\mathsf{T}}\cdot\underline{\overline{\boldsymbol{J}}}(\overline{\boldsymbol{\alpha}})\right) \tag{D.11}$$

with λ a weighing factor for stability. The specific implementation used in this dissertation is the `scipy.optimize.leastsq` routine from the `SciPy` toolbox for Python (Jones *et al.*, 2001–) which implement the code of the `MINPACK` library (Moré *et al.*, 1980).

For numerical purposes, the components of the i-th row of the Jacobian in equation (D.7) are

$$\begin{aligned}
\frac{\partial y\left(t_i,\overline{\boldsymbol{\alpha}}\right)}{\partial y_{\text{offs}}} &= 1 \\
\frac{\partial y\left(t_i,\overline{\boldsymbol{\alpha}}\right)}{\partial C} &= \mathrm{e}^{-\zeta\omega_n t_i}\cos\left(\omega_d t_i - \theta\right) \\
\frac{\partial y\left(t_i,\overline{\boldsymbol{\alpha}}\right)}{\partial \omega_n} &= \frac{\partial y_{\text{h}}\left(t_i,\overline{\boldsymbol{\alpha}}\right)}{\partial \omega_n} + \frac{\partial y_{\text{p}}\left(t_i,\overline{\boldsymbol{\alpha}}\right)}{\partial \omega_n} \\
\frac{\partial y\left(t_i,\overline{\boldsymbol{\alpha}}\right)}{\partial \zeta} &= \frac{\partial y_{\text{h}}\left(t_i,\overline{\boldsymbol{\alpha}}\right)}{\partial \zeta} + \frac{\partial y_{\text{p}}\left(t_i,\overline{\boldsymbol{\alpha}}\right)}{\partial \zeta} \\
\frac{\partial y\left(t_i,\overline{\boldsymbol{\alpha}}\right)}{\partial \theta} &= C\,\mathrm{e}^{-\zeta\omega_n t_i}\sin\left(\omega_d t_i - \theta\right) \\
\frac{\partial y\left(t_i,\overline{\boldsymbol{\alpha}}\right)}{\partial U_j} &= Y_j\cos\left(\Omega_j t_i + \Phi_j - \phi_j\right) \qquad j = 0,1,\ldots,p \\
\frac{\partial y\left(t_i,\overline{\boldsymbol{\alpha}}\right)}{\partial \Phi_j} &= -U_j Y_j\sin\left(\Omega_j t_i + \Phi_j - \phi_j\right) \qquad j = 0,1,\ldots,p
\end{aligned}$$

with

$$\frac{\partial y_{\mathrm{h}}\left(t_i, \overline{\boldsymbol{\alpha}}\right)}{\partial \omega_n} = -C\,\zeta\,t_i\,\mathrm{e}^{-\zeta\omega_n t_i}\left(\cos\left(\omega_d t_i - \theta\right) + \frac{\sqrt{1-\zeta^2}}{\zeta}\sin\left(\omega_d t_i - \theta\right)\right)$$

$$\frac{\partial y_{\mathrm{h}}\left(t_i, \overline{\boldsymbol{\alpha}}\right)}{\partial \zeta} = -C\omega_n t_i\,\mathrm{e}^{-\zeta\omega_n t_i}\left(\cos\left(\omega_d t_i - \theta\right) - \frac{\zeta}{\sqrt{1-\zeta^2}}\sin\left(\omega_d t_i - \theta\right)\right)$$

$$\frac{\partial y_{\mathrm{p}}\left(t_i, \overline{\boldsymbol{\alpha}}\right)}{\partial \omega_n} = -\sum_{j=0}^{p}\frac{U_j r_j}{\omega_n}\left(\frac{\partial Y_j}{\partial r_j}\cos\left(\Omega_j t_i + \Phi_j - \phi_j\right) + Y_j\frac{\partial \phi_j}{\partial r_j}\sin\left(\Omega_j t_i + \Phi_j - \phi_j\right)\right)$$

$$\frac{\partial y_{\mathrm{p}}\left(t_i, \overline{\boldsymbol{\alpha}}\right)}{\partial \zeta} = \sum_{j=0}^{p}U_j\left(\frac{\partial Y_j}{\partial \zeta}\cos\left(\Omega_j t_i + \Phi_j - \phi_j\right) + Y_j\frac{\partial \phi_j}{\partial \zeta}\sin\left(\Omega_j t_i + \Phi_j - \phi_j\right)\right)$$

and

$$\frac{\partial Y_j}{\partial r_j} = -\frac{2r_j}{Y_j}\left(\frac{2\zeta^2 r_j^4 + r_j^2 - 1}{\left(4\zeta^2 r_j^2 + r_j^4 - 2r_j^2 + 1\right)^2}\right)$$

$$\frac{\partial Y_j}{\partial \zeta} = \frac{4\zeta r_j^4}{Y_j}\left(\frac{r_j^2 - 2}{\left(4\zeta^2 r_j^2 + r_j^4 - 2r_j^2 + 1\right)^2}\right)$$

$$\frac{\partial \phi_j}{\partial r_j} = -\frac{2r_j^2\zeta\left(4\zeta^2 r_j^2 - r_j^2 + 3\right)}{\left(4\zeta^2 r_j^2 + 1\right)\left(r_j^4 + 4\zeta^2 r_j^2 - 2r_j^2 + 1\right)}$$

$$\frac{\partial \phi_j}{\partial \zeta} = \frac{2r_j^3\left(4\zeta^2 r_j^2 + r_j^2 - 1\right)}{\left(4\zeta^2 r_j^2 + 1\right)\left(r_j^4 + 4\zeta^2 r_j^2 - 2r_j^2 + 1\right)}$$

Appendix

E

Particle contact parameters

List of symbols for appendix E

a, b	the semi-major and semi-minor axes of contact ellipse	[m]
A, B	positive constants	[−]
c_c	cylindrical contact correction factor (eqn. E.23)	[−]
c_e	von Mises stress coefficient	[−]
c_κ	Hertz geometric constant (eqn. E.17)	[−]
d	distance	[m]
E	modulus of elasticity (Young's modulus)	[Pa]
$\tilde{E}$	weighted material property parameter (eqn. E.12)	[Pa]
F_n	normal force, $F_n = \|\overline{\boldsymbol{F}}_n\|$	[N]
$\overline{\boldsymbol{F}}_n$	normal force vector	[N]
i, j	indices	
k_n	linear stiffness (eqn. E.34)	[N/m]
$\tilde{k}_\mathrm{H}$	Hertz contact constant (eqn. E.17)	[$\mathrm{N/m^{1/2}}$]
n	stress calculation factor (eqn. E.26)	[−]
p	pressure distribution in contact area (eqn. E.7)	[Pa]
p_max	maximum contact pressure	[Pa]
r	ball radius	[m]
r', r''	principle radii of curvature of surface at contact point	[m]
R_c	cylinder radius	[m]
$\tilde{R}$	weighted radius (eqn. E.11)	[m]
S_Y	yield strength	[Pa]
x, y, z	Cartesian coordinates	[m]
δ	particle overlap	[m]
δ_Y	particle overlap at yielding	[m]

Δ	combined parameter, $\Delta = \tilde{R}/\tilde{E}$	[m/Pa]
κ	aspect ratio of contact ellipse, $\kappa = b/a$	[−]
ν	Poison's ratio	[−]
ϕ	stress calculation factor (eqn. E.26)	[−]
ψ	angle between major axes of contacting surfaces	[rad]
σ_{ii}	principle stresses (eqn. E.25)	[Pa]
σ_{e}	Von Misses stress (eqn. E.28)	[Pa]
Ω, Ω'	stress calculation factor	[−]

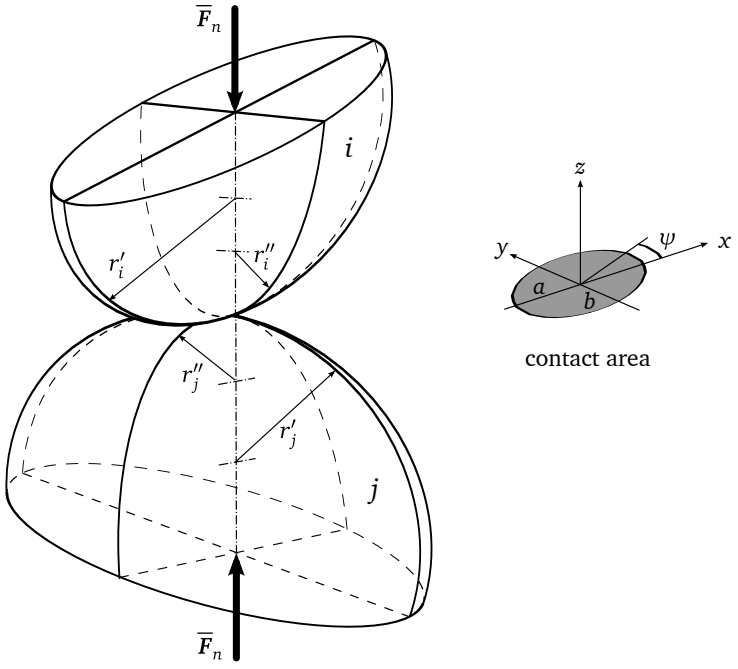

Figure E.1. Two curved surfaces in contact

E.1 Introduction

This appendix gives a short overview of the Hertz contact theory and lists the main equations necessary to solve the contact parameters. It is not the full theoretical deduction of the theory. Most of the content is taken verbatim from Boresi and Schmidt (2003).

E.2 Hertz contacts

When two bodies i and j are in contact under a normal load force $\overline{F}_n$ as depicted in figure E.1, they deform in the vicinity of the contact point so that they touch over a finite contact area. It is assumed that this contact area is small compared to the overall dimensions of the bodies.

The principle radii of curvature of the two surfaces at the contact point are r_i', r_i'' and r_j', r_j'' respectively. The contact area is in the common contact plain to the two surfaces and is denoted as the x-y Cartesian plane. The intersection of the planes in which the radii r_i' and r_j' lie form an angle ψ. The line of action of the load force $\overline{\boldsymbol{F}}_n$ lies along the z-axis and passes through the centre of curvature of bodies and through the contact point.

E.2.1 Contact area

From the Hertz contact theory the contact area is assumed to be elliptical and the boundary is given by

$$\frac{x^2}{a^2} + \frac{y^2}{b^2} = 1 \tag{E.1}$$

with a and b the semi-major and semi-minor axes of the ellipse. The aspect ratio κ of the ellipse is defined as

$$\kappa = \frac{b}{a}, \qquad (\kappa \leq 1). \tag{E.2}$$

For the analysis of the contact stresses, an expression for the distance d between corresponding points on the surfaces near the contact point is needed. From Boresi and Schmidt (2003, p. 595), it is given as $d = Ax^2 + By^2$ with A and B positive constants that depends on the principle radii of curvature of the two surfaces

$$A = \frac{1}{4}\left(\frac{1}{r_i'} + \frac{1}{r_i''} + \frac{1}{r_j'} + \frac{1}{r_j''}\right) - \frac{1}{4}\sqrt{\left(\frac{1}{r_i'} - \frac{1}{r_i''}\right)^2 + \left(\frac{1}{r_j'} - \frac{1}{r_j''}\right)^2 + 2\left(\frac{1}{r_i'} - \frac{1}{r_i''}\right)\left(\frac{1}{r_j'} - \frac{1}{r_j''}\right)\cos 2\alpha}\,, \tag{E.3}$$

$$B = \frac{1}{4}\left(\frac{1}{r_i'} + \frac{1}{r_i''} + \frac{1}{r_j'} + \frac{1}{r_j''}\right) + \frac{1}{4}\sqrt{\left(\frac{1}{r_i'} - \frac{1}{r_i''}\right)^2 + \left(\frac{1}{r_j'} - \frac{1}{r_j''}\right)^2 + 2\left(\frac{1}{r_i'} - \frac{1}{r_i''}\right)\left(\frac{1}{r_j'} - \frac{1}{r_j''}\right)\cos 2\alpha}\,. \tag{E.4}$$

We also define the following elliptic integrals that are needed for solving the contact stresses and shape of the contact ellipse as

$$\begin{aligned}
\mathcal{F}(\phi,\kappa) &= \int_0^{\phi} \frac{\mathrm{d}\vartheta}{\sqrt{1-(1-\kappa^2)\sin^2\vartheta}}, \\
\mathcal{H}(\phi,\kappa) &= \int_0^{\phi} \sqrt{1-(1-\kappa^2)\sin^2\vartheta}\,\mathrm{d}\vartheta\,, \\
\mathcal{K}(\kappa) &= \mathcal{F}\left(\tfrac{\pi}{2},\kappa\right) = \int_0^{\pi/2} \frac{\mathrm{d}\vartheta}{\sqrt{1-(1-\kappa^2)\sin^2\vartheta}}, \\
\mathcal{E}(\kappa) &= \mathcal{H}\left(\tfrac{\pi}{2},\kappa\right) = \int_0^{\pi/2} \sqrt{1-(1-\kappa^2)\sin^2\vartheta}\,\mathrm{d}\vartheta\,.
\end{aligned} \tag{E.5}$$

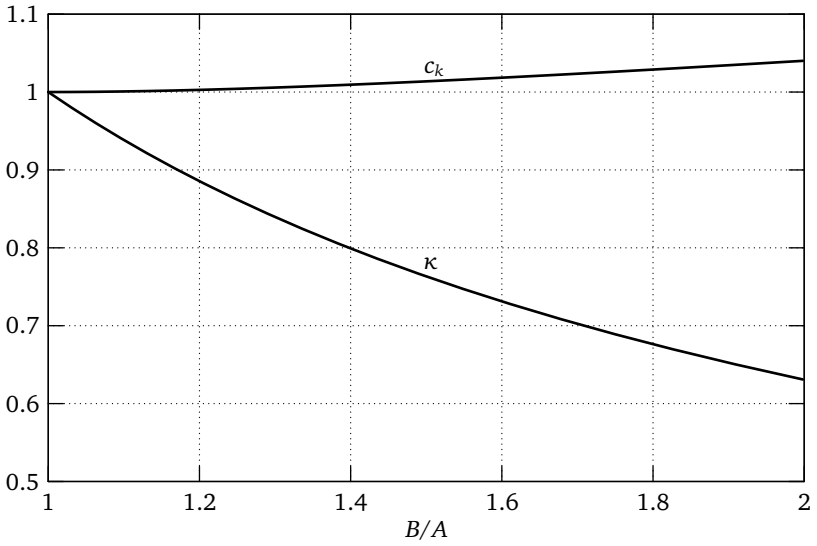

Figure E.2. Geometric coefficients for elliptic Hertz contacts

The aspect ratio of the contact ellipse, κ, depends on the geometry of the contacting surfaces and is assumed constant for any load. The numerical value of κ is determined by solving the following equation with the ratio B/A obtained from equations (E.3) and (E.4). See figure E.2 for numerical values.

$$\frac{B}{A} = \frac{\left(1/\kappa^2\right)\mathcal{E}(\kappa) - \mathcal{K}(\kappa)}{\mathcal{K}(\kappa) - \mathcal{E}(\kappa)}, \qquad (\kappa < 1) \tag{E.6}$$

See figure E.2 for numerical values of κ in terms of B/A.

E.2.2 Contact pressure

The pressure distribution p in the contact area is given by

$$p(x, y) = p_{\max}\left(1 - \frac{x^2}{a^2} - \frac{y^2}{b^2}\right)^{\frac{1}{2}} \tag{E.7}$$

with $p_{\max}$ the maximum contact pressure. Integration of the forces over the total contact area results in

$$\|\overline{\boldsymbol{F}}_n\| = F_n = \tfrac{2}{3}\pi a b p_{\max} = \tfrac{2}{3}\pi a^2 \kappa p_{\max}. \tag{E.8}$$

The magnitude of a and b depends on the magnitude of the contact load F_n (or contact strain) and is given by

$$b = a\,\kappa = \left(\frac{3\kappa\,\mathcal{E}(\kappa)\,\Delta}{2\pi} F_n\right)^{\frac{1}{3}}. \tag{E.9}$$

The parameter Δ containing the geometry an material properties is

$$\Delta = \frac{1}{A+B}\left(\frac{1-\nu_i^2}{E_i} + \frac{1-\nu_j^2}{E_j}\right) = \frac{\tilde{R}}{\tilde{E}}, \tag{E.10}$$

and the weighted radius $\tilde{R}$ and material property parameter are $\tilde{E}$

$$\frac{1}{\tilde{R}} = A + B = \frac{1}{2}\left(\frac{1}{r_i'} + \frac{1}{r_i''} + \frac{1}{r_j'} + \frac{1}{r_j''}\right), \tag{E.11}$$

$$\frac{1}{\tilde{E}} = \frac{1-\nu_i^2}{E_i} + \frac{1-\nu_j^2}{E_j}, \tag{E.12}$$

with E the modulus of elasticity and ν Poison's ratio for the materials in contact.

By inserting equation (E.8) into (E.9), the major and minor axes of the contact ellipse can be calculated in terms of the maximum pressure

$$b = a\,\kappa = p_{\max}\,\mathcal{E}(\kappa)\,\Delta. \tag{E.13}$$

Equating equation (E.9) to (E.13), the maximum pressure in terms of the load force follows as

$$p_{\max} = \left(\frac{3\kappa}{2\pi\,\mathcal{E}^2(\kappa)\,\Delta^2}F_n\right)^{\frac{1}{3}}. \tag{E.14}$$

E.2.3 Force-displacement

The overlap or total deformation between the bodies for a load $\overline{\boldsymbol{F}}_n$ is

$$\delta = \frac{3\kappa\,F_n\,\mathcal{K}(\kappa)}{2\pi}\left(\frac{A+B}{a\kappa/\Delta}\right) = \frac{3\mathcal{K}(\kappa)}{2\pi a\tilde{E}}F_n. \tag{E.15}$$

Inserting equation (E.9) into (E.15) and rewriting it in terms of the magnitude of the contact load F_n gives

$$F_n = \tilde{k}_{\mathrm{H}}\,\delta^{\frac{3}{2}} \tag{E.16}$$

with $\tilde{k}_{\mathrm{H}}$ the Hertz constant depending on the geometry and materials properties of the bodies in contact,

$$\tilde{k}_{\mathrm{H}} = \tfrac{4}{3}c_\kappa\,\tilde{E}\,\sqrt{\tilde{R}}, \qquad c_\kappa = \frac{\pi}{2\kappa}\sqrt{\frac{\mathcal{E}(\kappa)}{\mathcal{K}^3(\kappa)}}. \tag{E.17}$$

Figure E.2 gives numerical values for c_κ against B/A.

We now investigate more specifically the types of contacts encountered in this dissertation, such as ball-ball, ball-wall and ball-cylinder contacts.

Ball-ball: This type of contact has a circular contact area with $\kappa = 1$ and $c_\kappa = 1$. The contact radii are $r_i' = r_i'' = r_i$ and $r_j' = r_j'' = r_j$. Equation (E.17) then reduces to

$$\tilde{k}_{\mathrm{H_b}} = \frac{4}{3}\tilde{E}\,\sqrt{\tilde{R}} \quad \text{with} \quad \tilde{R} = \frac{r_i r_j}{r_i + r_j}. \tag{E.18}$$

For uniform sized particles $\tilde{R} = \frac{1}{2}r$.

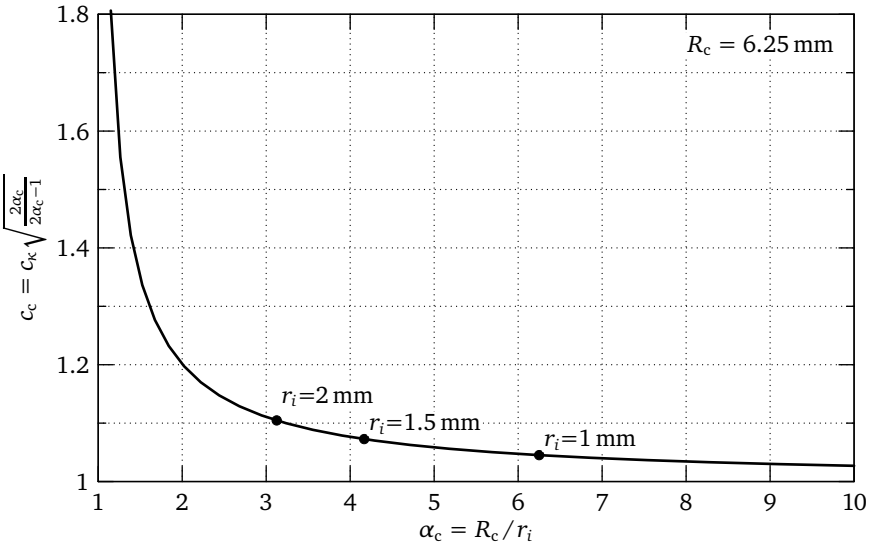

Figure E.3. Correction factor c_c for ball-cylinder contacts

Ball-wall: Here the contact area is still circular with $\kappa = 1$ and $c_\kappa = 1$. The contact radii are $r_i' = r_i'' = r_i$ and $r_j' = r_j'' = \infty$ and $\tilde{R} = r_i$. Equation (E.17) for a ball-wall contact is

$$\tilde{k}_{\mathrm{Hp}} = \frac{4}{3}\tilde{E}\sqrt{r_i} \tag{E.19}$$

Ball-cylinder: Consider a ball inside a cylinder. The contact area is now elliptic and κ must be calculated from equation (E.6). The contact radii are $r_i' = r_i'' = r_i$, $r_j' = -R_c$ and $r_j'' = \infty$ with R_c the cylinder internal radius. The radius ratio is defined as

$$\alpha_c = R_c / r_i, \quad \alpha_c > 1\ . \tag{E.20}$$

The aspect ratio κ can be solved from Equation (E.6) in terms of the radius ratio α_c

$$\frac{B}{A} = \frac{\alpha_c}{\alpha_c - 1} = \frac{\left(1/\kappa^2\right)\mathcal{E}(\kappa) - \mathcal{K}(\kappa)}{\mathcal{K}(\kappa) - \mathcal{E}(\kappa)}. \tag{E.21}$$

The effective radius, equation (E.11), in terms of α_c is

$$\tilde{R} = \frac{1}{A+B} = \frac{2\alpha_c}{2\alpha_c - 1} r_i. \tag{E.22}$$

Equation (E.17) for a ball-cylinder contact is then

$$\tilde{k}_{\mathrm{Hc}} = \frac{4}{3}\, c_c\, \tilde{E}\, \sqrt{r_i} \quad \text{with} \quad c_c = c_\kappa \left(\frac{2\alpha_c}{2\alpha_c - 1}\right)^{1/2}. \tag{E.23}$$

The numerical values for the cylindrical correction factor c_c are given in table E.1.

Table E.1. Correction factor for ball-cylinder contacts (R_c=6.25 mm)

	r_i	α_c	κ	c_c
⌀2 mm Ball	1.0 mm	6.250	0.8903	1.0452
⌀3 mm Ball	1.5 mm	4.167	0.8329	1.0727
⌀4 mm Ball	2.0 mm	3.125	0.7734	1.1046

E.2.4 Principal stresses

The internal principal stresses along the z axis for $\kappa = 1$ are given by

$$\sigma_{xx} = -\left[\left(1 - \frac{z}{a}\arctan\frac{1}{z/a}\right)(1+\nu) - \frac{1}{2\left(1+z^2/a^2\right)}\right] p_{\max}, \tag{E.24a}$$

$$\sigma_{yy} = \sigma_{xx}, \tag{E.24b}$$

$$\sigma_{zz} = -\frac{1}{1+z^2/a^2}\, p_{\max}. \tag{E.24c}$$

For $\kappa < 1$

$$\sigma_{xx} = \frac{2\kappa}{1-\kappa^2}\left(\Omega_x + \nu\Omega_x'\right) p_{\max}, \tag{E.25a}$$

$$\sigma_{yy} = \frac{2\kappa}{1-\kappa^2}\left(\Omega_y + \nu\Omega_y'\right) p_{\max}, \tag{E.25b}$$

$$\sigma_{zz} = -\frac{2\kappa}{1-\kappa^2}\left(\frac{1-n^2}{2n}\right) p_{\max}, \tag{E.25c}$$

with parameters

$$\cot\phi = \kappa(z/a), \qquad n = \sqrt{\frac{\kappa^2 + \kappa^2(z/a)^2}{1+\kappa^2(z/a)^2}} \tag{E.26}$$

and

$$\Omega_x = -\frac{1-n}{2} + \kappa\frac{z}{a}\left[\mathcal{F}(\phi,\kappa) - \mathcal{H}(\phi,\kappa)\right] \tag{E.27a}$$

$$\Omega_x' = -\frac{n}{\kappa^2} + 1 + \kappa\frac{z}{a}\left[\frac{1}{\kappa^2}\mathcal{H}(\phi,\kappa) - \mathcal{F}(\phi,\kappa)\right] \tag{E.27b}$$

$$\Omega_y = \frac{1}{2n} + \frac{1}{2} - \frac{n}{\kappa^2} + \kappa\frac{z}{a}\left[\frac{1}{\kappa^2}\mathcal{H}(\phi,\kappa) - \mathcal{F}(\phi,\kappa)\right] \tag{E.27c}$$

$$\Omega_y' = -1 + n + \kappa\frac{z}{a}\left[\mathcal{F}(\phi,\kappa) - \mathcal{H}(\phi,\kappa)\right] \tag{E.27d}$$

Yielding (plastic deformation) of the material depends on the total stress state. The yield model considered here is the distortion energy density or von Mises criterion (Boresi and Schmidt, 2003, §4.4) for principal stresses

$$\sigma_e = \tfrac{1}{\sqrt{2}}\sqrt{(\sigma_{xx}-\sigma_{yy})^2 + (\sigma_{yy}-\sigma_{zz})^2 + (\sigma_{zz}-\sigma_{xx})^2} = c_e\, p_{\max}. \tag{E.28}$$

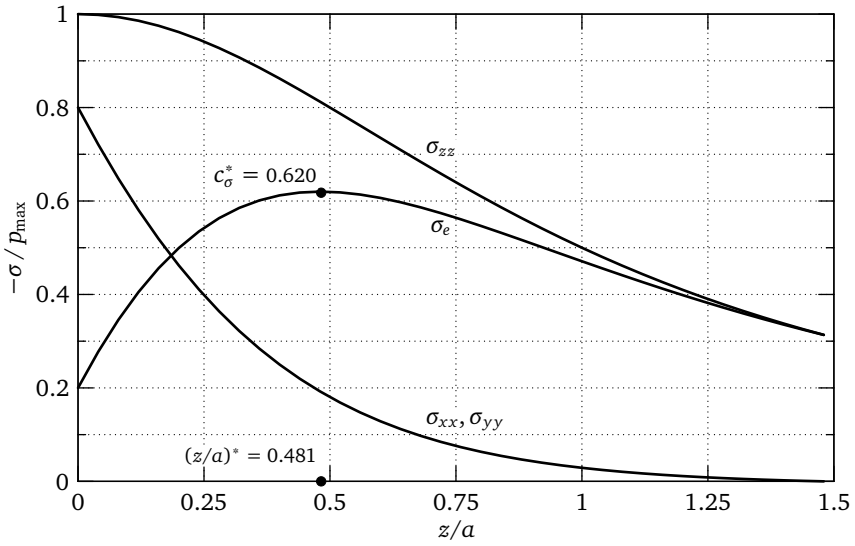

Figure E.4. The von Mises stress coefficient c_e for a circular contact, $\kappa = 1$, and $\nu = 0.3$

The von Mises stress coefficient c_e is a function of $\kappa(z/a)$. It has a maximum value, c_e^*, at a distance $(z/a)^*$ below the surface. An example of a circular contact ($\kappa = 1$) and $\nu = 0.3$ is shown in figure E.4. The maximum value $c_\mathrm{e}^* = 0.620$ is at a depth of $(z/a)^* = 0.481$. If S_Y is the tensile yield strength of the material, then yielding occurs when

$$\sigma_\mathrm{e} = c_\mathrm{e}^* \, p_{\max} \geq S_Y. \tag{E.29}$$

Let $p_{\max} = p_Y$ be the maximum contact pressure at the point where the material starts to yield, then

$$p_Y = S_Y / c_\mathrm{e}^*. \tag{E.30}$$

E.3 Linearisation of Hertz stiffness

Equation (E.15) can also be written in terms of the maximum contact pressure $p_{\max}$ by inserting equations (E.8) and (E.9)

$$\delta = \frac{a\,\kappa}{\tilde{E}} \mathcal{E}(\kappa) \, p_{\max} = \frac{\tilde{R}}{\tilde{E}^2} \mathcal{E}(\kappa) \, \mathcal{K}(\kappa) \, p_{\max}^2. \tag{E.31}$$

Yielding occurs when $p_{\max} = p_Y = S_Y / c_\sigma^*$. If δ_Y is the overlap at that condition, then

$$\delta_Y = \frac{\tilde{R}}{\tilde{E}^2} \mathcal{E}(\kappa) \, \mathcal{K}(\kappa) \left(\frac{S_Y}{c_\sigma^*} \right)^2. \tag{E.32}$$

We can linearise the Hertz contact as a linear spring with stiffness k_n so that it will require the same amount of work to compress to the yielding overlap δ_Y,

$$W = k_n \int_0^{\delta_Y} \delta \, \mathrm{d}\delta = \tilde{k}_\mathrm{H} \int_0^{\delta_Y} \delta^{\frac{3}{2}} \, \mathrm{d}\delta \quad \Rightarrow \quad k_n = \tfrac{4}{5} \tilde{k}_\mathrm{H} \delta_Y^{\frac{1}{2}} \tag{E.33}$$

Inserting equations (E.17) and (E.32) into (E.33) results in

$$k_n = \frac{8\pi}{15\,\kappa}\left(\frac{\mathcal{E}(\kappa)}{\mathcal{K}(\kappa)}\right)\tilde{R}\frac{S_Y}{c_\sigma^*}. \tag{E.34}$$

For circular contacts, $\kappa = 1$, and uniform sized particle with $\tilde{R} = \frac{1}{2}r$, equation (E.34) reduces to

$$k_n = \frac{8\pi}{15\,c_\sigma^*}\tilde{R}\,S_Y \approx 1.35\;r\,S_Y \tag{E.35}$$

Appendix

F

Matrix Tensor Notation

F.1 Basic vector notation

All vectors are in the 3-dimensional Euclidean space $\mathbb{R}^3$ and tensors in $\mathbb{R}^{3\times3}$. Any other vector space will be explicitly stated. The rest of this section lists the basic definitions of the notation of Hassenpflug (1993, 1995)

Physical vector:
$$\overrightarrow{\boldsymbol{v}} \equiv \overrightarrow{\boldsymbol{e}}_1 v_1 + \overrightarrow{\boldsymbol{e}}_2 v_2 + \overrightarrow{\boldsymbol{e}}_3 v_3 \tag{F.1}$$

The physical vector is the general representation of a vector in any coordinate system. The unit vectors $\overrightarrow{\boldsymbol{e}}_i$, $(i = 1, 2, 3)$, define the direction of the axes in a right-handed orthogonal Cartesian system. The components, $\overrightarrow{\boldsymbol{e}}_i v_i$, are the components of the vector and the scalar quantities, v_i, the elements of the vector.

Column vector:
$$\overline{\boldsymbol{v}}^a \equiv \begin{bmatrix} v_{a1} \\ v_{a2} \\ v_{a3} \end{bmatrix} \tag{F.2}$$

The column matrix of the elements of a vector is called a column vector and is the algebraic representation of a vector. The bar above the symbol of the vector indicates a column vector and the superscript (a) the index of the specific coordinate system in which the elements of the vector are expressed.

Row vector:
$$\underline{\boldsymbol{v}}_a \equiv \left[\overline{\boldsymbol{v}}^a\right]^{\mathsf{T}} = \begin{bmatrix} v_{a1} & v_{a2} & v_{a3} \end{bmatrix} \tag{F.3}$$

The row matrix of the elements of a vector is called a row vector. The bar below the symbol of the vector indicates a row vector and the subscript (a) the index of the specific coordinate system in which the elements of the vector are expressed. It is important to note that in general is $\left[\overline{\boldsymbol{v}}^a\right]^{\mathsf{T}} = \underline{\boldsymbol{v}^{\mathsf{T}}}_a$ for skew and curved coordinates (see Hassenpflug, 1995). The format in equation (F.3) without the transpose sign is only valid in Cartesian coordinates.

Norm:
$$\|\overrightarrow{\boldsymbol{v}}\| \equiv v, \tag{F.4a}$$
$$\|\overline{\boldsymbol{v}}\| \equiv v \equiv \sqrt{\underline{\boldsymbol{v}} \cdot \overline{\boldsymbol{v}}} = \sqrt{v_1^2 + v_2^2 + v_3^2} \tag{F.4b}$$

The norm of a vector is the algebraic size or length of the vector. The second equation, (F.4b), in element form, is only valid in Cartesian coordinates or Euclidean space.

Scalar, dot or inner product:

$$\vec{v} \bullet \vec{u} \equiv \underset{\rightarrow}{\underline{v}} \cdot \vec{u} = v\,u\,\cos\varphi, \tag{F.5a}$$

$$\overline{v} \bullet \overline{u} \equiv \underline{v} \cdot \overline{u} = v_1 u_1 + v_2 u_2 + v_3 u_3 \tag{F.5b}$$

The scalar product of two vectors results in a scalar. The angle φ is the angle in space between $\vec{v}$ and $\vec{u}$.

Dyad or outer product:

$$\overline{v} \circ \overline{u} \equiv \overline{v} \cdot \underline{u} = \begin{bmatrix} v_1 u_1 & v_1 u_2 & v_1 u_3 \\ v_2 u_1 & v_2 u_2 & v_2 u_3 \\ v_3 u_1 & v_3 u_2 & v_3 u_3 \end{bmatrix} \tag{F.6}$$

The dyad or outer product of two vectors results in a square matrix. There exists a well defined algebra for dyads. It is sometimes convenient to handle second-rank Cartesian tensors such as inertia tensors as a linear polynomial of dyads, called a dyadic.

Vector or cross product:

$$\begin{aligned} \vec{v} \times \vec{u} \equiv\ & (v_2 u_3 - v_3 u_2)\,\vec{e}_1 \\ & + (v_3 u_1 - v_1 u_3)\,\vec{e}_2 \\ & + (v_1 u_2 - v_2 u_1)\,\vec{e}_3 \end{aligned} \tag{F.7a}$$

$$\| \vec{a} \times \vec{c} \| = v\,u \sin\varphi \tag{F.7b}$$

The cross product of the two vector $\vec{v}$ and $\vec{u}$ results in a vector perpendicular to both $\vec{v}$ and $\vec{u}$. This operation is only defined in 3-dimensional Cartesian space. The angle φ is the angle in space between $\vec{v}$ and $\vec{u}$. The cross product can also be defined in terms of a matrix-vector operation $\overline{v} \times \overline{u} \equiv \underline{\overline{v}} \cdot \overline{u}$

Cross product tensor:

$$\underline{\overline{v}} \equiv \begin{bmatrix} 0 & -v_3 & v_2 \\ v_3 & 0 & -v_1 \\ -v_2 & v_1 & 0 \end{bmatrix} \tag{F.8}$$

Various identities for the cross product tensor can be verified. These identities will be extensively used throughout this dissertation.

$$\begin{array}{lll} \left[\underline{\overline{v}}\right]^{\mathsf{T}} = -\underline{\overline{v}} & \left[\underline{\overline{v}}\right]^{2} = \overline{v} \cdot \underline{v} - v^2 \underline{\overline{I}} & \underline{\widetilde{\overline{v} + \overline{u}}} = \underline{\overline{v}} + \underline{\overline{u}} \\ \underline{\overline{v}} \cdot \overline{u} = -\underline{\overline{u}} \cdot \overline{v} & \left[\underline{\overline{v}}\right]^{3} = -v^2 \underline{\overline{v}} & \underline{\widetilde{\overline{v} \cdot \overline{u}}} = \underline{\overline{v}} \cdot \underline{\overline{u}} - \underline{\overline{u}} \cdot \underline{\overline{v}} \end{array} \tag{F.9}$$

with $\underline{\overline{I}}$ the 3×3 identity matrix.

Identity matrix:

$$\underline{\overline{I}} \equiv \begin{bmatrix} 1 & 0 & 0 \\ 0 & 1 & 0 \\ 0 & 0 & 1 \end{bmatrix} \tag{F.10}$$

F.2 Vector transformations

In this section only a basic overview of vector rotations and transformations is given to establish the basic nomenclature and definitions. For a more in-depth discussion refer to Hassenpflug (1993).

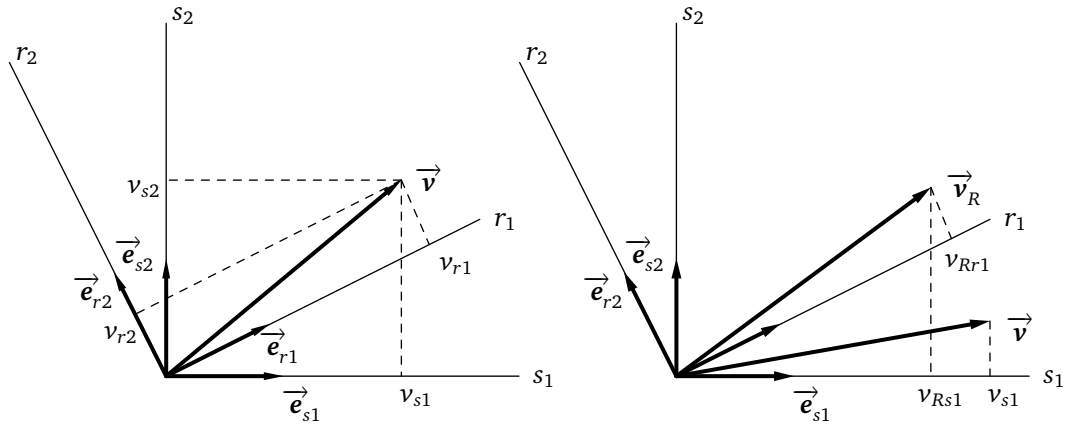

(a) Transformation (b) Rotations

Figure F.1. Vector transformations

Consider two Cartesian axis systems denoted by s and r as shown in figure F.1(a). From the general definition of a vector, equation (F.1), it follows

$$\vec{v} = \left[\vec{e}_{s1} \quad \vec{e}_{s2} \quad \vec{e}_{s3}\right] \cdot \begin{bmatrix} v_{s1} \\ v_{s2} \\ v_{s3} \end{bmatrix} = \underline{\vec{E}}_s \cdot \overline{v}_s \tag{F.11}$$

The quantity, $\underline{\vec{E}}_s = [\vec{e}_{s1}\ \vec{e}_{s2}\ \vec{e}_{s3}]$, is the base of the axis system denoted by s. It consists of the three orthogonal vectors parallel to the axes. From the outer product, equation (F.6), follows for the inverse of base $\underline{\vec{E}}_s$:

$$\left[\underline{\vec{E}}_s\right]^{\mathsf{T}} \cdot \underline{\vec{E}}_s = \underline{\overrightarrow{E}}^s \cdot \underline{\vec{E}}_s = \underline{I} \quad \Rightarrow \quad \left[\underline{\vec{E}}_s\right]^{\mathsf{T}} = \left[\underline{\vec{E}}_s\right]^{-1} = \underline{\overrightarrow{E}}^s \tag{F.12}$$

We can repeat the procedure of equation (F.11) for the vector $\vec{v}$ in terms of base $\underline{\vec{E}}_r$. The relationship of the elements of vector $\vec{v}$ in terms of base $\underline{\vec{E}}_s$ and base $\underline{\vec{E}}_r$ is then

$$\vec{v} = \underline{\vec{E}}_r \cdot \overline{v}^r = \underline{\vec{E}}_s \cdot \overline{v}^s \quad \Rightarrow \quad \begin{cases} \overline{v}^s & = \underline{\overrightarrow{E}}^s \cdot \underline{\vec{E}}_r = \underline{\overline{E}}^s_r \cdot \overline{v}^r \\ \overline{v}^r & = \underline{\overrightarrow{E}}^r \cdot \underline{\vec{E}}_s = \underline{\overline{E}}^r_s \cdot \overline{v}^s \end{cases} \tag{F.13}$$

The matrix quantities $\underline{\overline{E}}^s_r$ and $\underline{\overline{E}}^r_s$ are then the transformation matrices of the components of a vector between the two bases $\underline{\vec{E}}_s$ and $\underline{\vec{E}}_r$. The columns of the transformation matrix $\underline{\overline{E}}^s_r$ are the elements of the unit vector $\vec{e}_{s_i}$ expressed in base $\underline{\overrightarrow{E}}_s$ and

the rows are the unit vectors $\underrightarrow{\underline{e}}^{sj}$ expressed in base $\overrightarrow{\underline{E}}_r$.

$$\overline{\underline{E}}_r^s = \begin{bmatrix} \overline{e}_{r1}^s & \overline{e}_{r2}^s & \overline{e}_{r3}^s \end{bmatrix} = \begin{bmatrix} \underline{e}_r^{s1} \\ \underline{e}_r^{s2} \\ \underline{e}_r^{s3} \end{bmatrix} \tag{F.14}$$

The properties of the transformation matrix are well known, for example

$$\left[\overline{\underline{E}}_r^s\right]^{\mathsf{T}} = \left[\overline{\underline{E}}_r^s\right]^{-1} = \overline{\underline{E}}_s^r \tag{F.15}$$

F.3 Vector rotations

Consider the case of a vector in space with initial position $\overrightarrow{v}$. The vector is rotated to a new position in space, $\overrightarrow{v}_R$. Define the rotation tensor operation then as

$$\overrightarrow{v}_R = \underrightarrow{\underline{R}} \cdot \overrightarrow{v} \tag{F.16}$$

If the operation is applied to the rotation of all the direction vectors of a base $\overrightarrow{\underline{E}}_s$ to a new rotated base $\overrightarrow{\underline{E}}_r$, then

$$\overrightarrow{\underline{E}}_r = \underrightarrow{\underline{R}} \cdot \overrightarrow{\underline{E}}_s \tag{F.17}$$

or

$$\overline{\underline{E}}_r^s = \underrightarrow{\overline{\underline{E}}}^s \cdot \underrightarrow{\underline{R}} \cdot \overrightarrow{\underline{E}}_s = \overline{\underline{R}}_s^s \tag{F.18}$$

With reference to figure F.1(b), consider the case of a vector fixed in a rotating base $\overrightarrow{\underline{E}}_r$ with initial position $\overrightarrow{v}$ and final position after a rotation of $\overrightarrow{v}_R$. If the initial orientation of $\overrightarrow{\underline{E}}_r$ corresponds with that of $\overrightarrow{\underline{E}}_s$ then the numerical values of the components of $\overline{v}^s$ and $\overline{v}_R^r$ are equal. From the transformation of $\overrightarrow{v}_R$ it then follows that

$$\overline{v}_R^s = \overline{\underline{E}}_r^s \cdot \overline{v}_R^r = \overline{\underline{R}}_s^s \cdot \overline{v}^s \tag{F.19}$$

If the rotation matrix is transformed between bases, then

$$\overline{\underline{R}}_r^r = \overline{\underline{E}}_s^r \cdot \overline{\underline{R}}_s^s \cdot \overline{\underline{E}}_r^s = \overline{\underline{R}}_s^s \tag{F.20}$$

The rotation matrix is therefore identical in terms of both bases and we can thus denote it without the base indices, except when there is more than one rotation. The rotation matrix between bases $\overrightarrow{\underline{E}}_s$ and $\overrightarrow{\underline{E}}_r$ in terms of the transformation matrix is given by

$$\overline{\underline{R}} = \overline{\underline{E}}_r^s \tag{F.21}$$

$$\left[\overline{\underline{R}}\right]^{-1} = \left[\overline{\underline{R}}\right]^{\mathsf{T}} = \overline{\underline{E}}_s^r \tag{F.22}$$

List of References

Andrews, K.T. and Shillor, M. (2002). Vibrations of a beam with a damping tip body. *Mathematical and Computer Modelling*, vol. 35, pp. 1033–1042. (Cited on page 27.)

Aubert, A.C., Green, E.R. and Chen, G.Z. (2003 May). A comparison of the effectiveness of elastomeric tuned mass dampers and particle dampers. In: *SAE 2003 Noise & Vibration Conference and Exhibition*, SAE 2003-01-1419. SAE, Grand Traverse, MI, USA. (Cited on page 5.)

Avallone, E.A. and Baumeister, III, T. (eds.) (1996). *Marks' Standard Handbook for Mechanical Engineers*. 10th edn. McGraw-Hill, New York. (Cited on page 54.)

Bagi, K. and Kuhn, M.R. (2004). A definition of particle rolling in a granular assembly in terms of particle translations and rotations. *ASME Journal of Applied Mechanics*, vol. 71, pp. 493–501. (Cited on page 21.)

Boresi, A.P. and Schmidt, R.J. (2003). *Advanced Mechanics of Materials*. 6th edn. John Wiley & Sons, Inc, New York. (Cited on pages 110, 111, and 115.)

Brennen, C.E., Ghosh, S. and Wassgren, C.R. (1996). Vertical oscillation of a bed of granular material. *ASME Journal of Applied Mechanics*, vol. 63, pp. 156–161. (Cited on page 11.)

Brilliantov, N.V. and Pöschel, T. (1998). Rolling friction of a viscous sphere on a hard plane. *Europhysics Letters*, vol. 42, no. 5, pp. 511–516. (Cited on page 21.)

Brilliantov, N.V. and Pöschel, T. (1999). Rolling as a "continuing collision". *The European Physical Journal E*, vol. 12, pp. 299–301. (Cited on page 21.)

Brilliantov, N.V., Spahn, F., Hertzsch, J.-M. and Pöschel, T. (1996). Model for collisions in granular gases. *Physical Review E*, vol. 53, no. 5, pp. 5382–5392. (Cited on pages 20 and 51.)

Budynas, R.G. and Nisbett, J.K. (2008). *Shigley's Mechanical Engineering Design*. 8th edn. McGraw-Hill, Boston. (Cited on pages 25, 45, and 49.)

Cempel, C. and Lotz, G. (1993). Efficiency of vibrational energy dissipation by moving shot. *Journal of Structural Engineering*, vol. 119, no. 9, pp. 2642–2652. (Cited on pages 2 and 3.)

Chen, T., Mao, K., Huang, X. and Wang, M.Y. (2001 Mar 4–8). Dissipation mechanisms of non-obstructive particle damping using discrete element method. In: Inman, D.J. (ed.), *Proceedings of SPIE International Symposium on Smart Structures and Materials: Damping and Isolation*. Newport beach, CA. (Cited on page 22.)

Cundall, P.A. and Strack, O.D.L. (1979). A discrete numerical model for granular assemblies. *Géotechnique*, vol. 29, no. 1, pp. 47–65. (Cited on pages 5, 18, 21, and 50.)

De Souza, S.L.T., Caldas, I.L., Viana, R.L., Balthazar, J.M. and Brasil, R.M.L.F. (2005). Impact dampers for controlling chaos in systems with limited power supply. *Journal of Sound and Vibration*, vol. 279, pp. 955–967. (Cited on page 3.)

Dintwa, E., Van Zeebroeck, M., Tijskens, E. and Ramon, H. (2005). Torsion of viscoelastic spheres in contact. *Granular Matter*, vol. 7, pp. 169–179. (Cited on page 21.)

Duffy, K.P. (2004 Mar 18). Durability of the self-tuning impact damper in rotating turbine blades. In: *Proceedings of the 9th National Turbine Engine High Cycle Fatigue Conference*. (Cited on pages 4 and 5.)

Duncan, M.R., Wassgren, C.R. and Krousgrill, C.M. (2005). The damping performance of a single particle impact damper. *Journal of Sound and Vibration*, vol. 286, pp. 123–144. (Cited on page 3.)

Ema, S. and Marui, E. (2000). Suppression of chatter vibration of boring tools using impact dampers. *International Journal of Machine Tools & Manufacture*, vol. 40, no. 8, pp. 1141–1156. (Cited on page 4.)

Emam, S. (2008). Behavior of Hertz contact model + viscous dashpot in PFC3D. Personal communication. Itasca Tecnical Memorandum, Ref: SE-S14. (Cited on page 47.)

Evesque, P. (1992). Shaking dry powders and grains. *Contemporary Physics*, vol. 33, no. 4, pp. 245–261. (Cited on page 12.)

Falcon, E. (1997). *Comportements dynamiques associés au contact de Hertz : processus collectifs de collision et propagation d'ondes solitaires dans les milieux granulaires*. Ph.D. thesis, Université Claude Bernard Lyon I. (Cited on page 50.)

Falcon, E., Laroche, C., Fauve, S. and Coste, C. (1998*a*). Behavior of one inelastic ball bouncing repeatedly off the ground. *The European Physical Journal E*, vol. 3, pp. 45–57. (Cited on page 20.)

Falcon, E., Laroche, C., Fauve, S. and Coste, C. (1998*b*). Collision of a 1-D column of beads with a wall. *The European Physical Journal E*, vol. 5, pp. 111–131. (Cited on page 20.)

Fang, X., Luo, H. and Tang, J. (2008). Investigation of granular damping in transient vibrations using Hilbert transform based technique. *ASME Journal of Vibration and Acoustics*, vol. 130, no. 3, p. 031006. (Cited on page 18.)

Favier, J.F., Abbaspour-Fard, M.H., Kremmer, M. and Raji, A.O. (1999). Shape representation of axisymmetrical, non-spherical particles in discrete element simulation using multi-element model particles. *Engineering Computations*, vol. 16, no. 4, pp. 467–480. (Cited on page 19.)

Feldman, M. (2006). Time-varying vibration decomposition and analysis based on the Hilbert transform. *Journal of Sound and Vibration*, vol. 295, no. 3-5, pp. 518–530. (Cited on pages xii, 17, 18, 39, 40, and 75.)

Feldman, M. (2008). Theoretical analysis and comparison of the Hilbert transform decomposition methods. *Mechanical Systems and Signal Processing*, vol. 22, no. 3, pp. 509–519. (Cited on page 17.)

Flint, E.M. (1999 Feb 9–11). Experimental measurements of particle damping effectiveness under centrifugal loads. In: *Proceedings of the 4th National Turbine Engine High Cycle Fatigue Conference*. Monterey, CA. (Cited on page 15.)

Flint, E.M., Ruhl, E. and Olson, S.E. (2000 Mar 6–9). Experimental centrifuge testing and analytical studies of particle damping behavior. In: *Proceedings of the 5th National Turbine Engine High Cycle Fatigue Conference*. Chandler, AZ. (Cited on pages 15 and 16.)

Fowler, B.L., Flint, E.M. and Olson, S.E. (2000 Mar 5–9). Effectiveness and predictability of particle damping. In: Hyde, T.T. (ed.), *Proceedings of SPIE Conference on Smart Structures and Materials: Damping and Isolation*, vol. 3989, pp. 356–367. Newport Beach, CA. (Cited on pages 14 and 17.)

Fowler, B.L., Flint, E.M. and Olson, S.E. (2001 Mar 4–8). Design methodology for particle damping. In: Inman, D.J. (ed.), *Proceedings of SPIE International Symposium on Smart Structures and Materials: Damping and Isolation*, vol. 4331, pp. 186–197. Newport Beach, CA. (Cited on page 14.)

František, P. (2003). More detail view on the dynamics of the impact damper. *Facta Universitatis: Mechanics, Automatic Control and Robotics*, vol. 3, no. 14, pp. 907–920. (Cited on page 4.)

Friend, R.D. and Kinra, V.K. (1999 Mar). Measurement and analysis of particle impact damping. In: Hyde, T.T. (ed.), *Proceedings of SPIE Conference on Smart Structures and Materials: Passive Damping and Isolation*, vol. 3672, pp. 20–31. Newport Beach, CA, USA. (Cited on page 14.)

Friend, R.D. and Kinra, V.K. (2000). Particle impact damping. *Journal of Sound and Vibration*, vol. 233, no. 1, pp. 93–118. (Cited on pages 3, 5, and 14.)

Ghaboussi, J. and Barbosa, R. (1990). Three-dimensional discrete element method for granular materials. *International Journal for Numerical and Analytical Methods in Geomechanics*, vol. 14, no. 7, pp. 451–472. (Cited on page 19.)

Goddard, J.D. (1990). Nonlinear elasticity and pressure-dependent wave speeds in granular media. *Proceedings of the Royal Society: Mathematical and Physical Sciences*, vol. 430, no. 1878, pp. 105–131. (Cited on page 10.)

Hassenpflug, W.C. (1993). Matrix tensor totation part I. Rectilinear orthogonal coordinates. *Computers & Mathematics with Applications*, vol. 26, no. 3, pp. 55–93. (Cited on pages xii, 118, and 120.)

Hassenpflug, W.C. (1995). Matrix tensor notation part II. Skew and curved coordinates. *Computers & Mathematics with Applications*, vol. 29, no. 11, pp. 1–103. (Cited on pages xii and 118.)

Hertz, H. (1882). Über die Berührung fester elastischer Korper,. *Journal für die reine und angewandte Mathematik*, vol. 92, p. 136. (Cited on page 20.)

Hollkamp, J.J. and Gordon, R.W. (1998 Jun). Experiments with particle damping. In: Davis, L.P. (ed.), *Proceedings of SPIE Conference on Smart Structures: Passive Damping and Isolation*, vol. 3327, pp. 2–12. (Cited on pages 2 and 14.)

Hostler, S.R. (2005). *Wave Propagation in Granular Materials*. PhD, California Institute of Technology, Pasadena, California. (Cited on page 11.)

Hostler, S.R. and Brennen, C.E. (2005). Pressure wave propagation in a granular bed. *Physical Review E*, vol. 72, no. DEM, virbrations, waves, pp. 031303/1 – 031303/13. (Cited on page 11.)

Hsiau, S.-S., Ou, M.-Y. and Tai, C.-H. (2002). The flow behavior of granular material due to horizontal shaking. *Advanced Powder Technology*, vol. 13, no. 2, pp. 167–180. (Cited on page 13.)

Huang, N.E., Shen, Z., Long, S.R., Wu, M.C., Shih, H.H., Zeng, Q., Yen, N.-C., Tung, C.C. and Liu, H.H. (1998). The empirical mode decomposition and the Hilbert spectrum for nonlinear and non-stationary time series analysis. *Proceedings of the Royal Society of London A – Mathematical, Physical and Engineering Sciences*, vol. 454, no. 1971, pp. 903–995. (Cited on pages xii and 17.)

Iwashita, K. and Oda, M. (1998). Rolling resistance at contacts in the simulation of shear band development by DEM. *Journal of Engineering Mechanics*, vol. 124, no. 3, pp. 285–292. (Cited on page 21.)

Iwashita, K. and Oda, M. (2000). Micro-deformation mechanism of shear banding process based on modified distinct element method. *Powder Technology*, vol. 109, pp. 192–205. (Cited on page 21.)

Johnson, K.L. (1987). *Contact Mechanics*. Cambridge University Press, Cambridge. ISBN 0-521-34796-3. (Reprint with corrections). (Cited on page 20.)

Jones, E., Oliphant, T., Peterson, P. *et al.* (2001–). SciPy: Open source scientific tools for Python.
Available at: `http://www.scipy.org/` (Cited on page 107.)

Kerschen, G., McFarland, D.M., Kowtko, J.J., Lee, Y.S., Bergman, L.A. and Vakakis, A.F. (2007). Experimental demonstration of transient resonance capture in a system of two coupled oscillators with essential stiffness nonlinearity. *Journal of Sound and Vibration*, vol. 229, no. 4-5, pp. 822–838. (Cited on page 18.)

King, P.J., Swift, M.R., Benedict, K.A. and Routledge, A. (2000). Surface stability of granular systems under horizontal and vertical vibration: The applicability of a coefficient of friction. *Physical Review E*, vol. 62, no. 5, pp. 6982–6988. (Cited on page 13.)

Knight, J.B., Fandrich, C.G., Lau, C.N., Jaeger, H.M. and Nagel, S.R. (1995). Density relaxation in a vibrated granular material. *Physical Review E*, vol. 51, no. 5, pp. 3957–3963. (Cited on page 11.)

Kruggel-Emden, H., Simsek, E., Rickelt, S., Wirtz, S. and Scherer, V. (2007). Review and extension of normal force models for the Discrete Element Method. *Powder Technology*, vol. 171, pp. 157–173. (Cited on page 20.)

Kruggel-Emden, H., Wirtz, S. and Scherer, V. (2008). A study on tangential force laws applicable to the discrete element method (DEM) for materials with viscoelastic or plastic behavior. *Chemical Engineering Science*, vol. 63, pp. 1523–1541. (Cited on page 20.)

Kuhn, M.R. and Bagi, K. (2004). Alternative definition of particle rolling in a granular assembly. *Journal of Engineering Mechanics*, vol. 130, no. 7, pp. 826–835. (Cited on page 21.)

Kuwabara, G. and Kono, K. (1987). Restitution coefficient in a collision between two spheres. *Japanese Journal of Applied Physics, Part 1*, vol. 26, no. 8, pp. 1230–1233. (Cited on pages 20 and 51.)

Lieber, P. and Jensen, D.P. (1945). An acceleration damper: Development, design and some applications. *Transactions of ASME*, vol. 67, pp. 523–530. (Cited on page 3.)

Liffman, K., Metcalfe, G. and Cleary, P.W. (1997). Granular convection and transport due to horizontal shaking. *Physical Review Letters*, vol. 79, no. 23, pp. 4574–4576. (Cited on page 12.)

Liu, W., Tomlinson, G.R. and Rongong, J.A. (2005). The dynamic characterisation of disk geometry particle dampers. *Journal of Sound and Vibration*, vol. 280, pp. 849–861. (Cited on pages 14, 16, 17, and 62.)

Liu, W., Tomlinson, G.R. and Worden, K. (2002 Sep 16–18). Nonlinearity study of particle dampers. In: *The International Conference on Noise and Vibration Engineering (ISMA 2002)*, vol. I, pp. 495–499. Leuven, Belgium. (Cited on page 14.)

Luding, S. (1994). *Models and Simulations of Granular Materials*. PhD, Universität Freiburg. (Cited on page 5.)

Luding, S. (2004). Molecular dynamics simulations of granular materials. In: Hinrichsen, H. and Wolf, D. (eds.), *The Physics of Granular Media*, pp. 299–324. Wiley-VCH, Weinheim. ISBN 3-527-40373-6. (Cited on page 5.)

Luo, H., Fang, X., Hallman, D. and Tang, J. (2007 Apr 23–26). Characterization of granular damper using Hilbert transform and free vibration response. In: *Proceedings of the 48th AIAA/ASME/ASCE/AHS/ASC Structures, Structural Dynamics, and Materials Conference*, AIAA 2007-2048. Honolulu, Hawaii. (Cited on page 18.)

Mao, K., Wang, M.Y., Xu, Z. and Chen, T. (2004*a*). Simulation and characterization of particle damping in transient vibrations. *ASME Journal of Vibration and Acoustics*, vol. 126, pp. 202–211. (Cited on page 6.)

Mao, K., Wang, M.Y., Xu, Z. and Chen, Z. (2004*b*). DEM simulation of particle damping. *Powder Technology*, vol. 142, pp. 154–165. (Cited on page 6.)

Marhadi, K.S. (2003). *Particle Impact Damping: Influence of Material and Size*. Master's thesis, Texas A&M University. (Cited on page 14.)

Marhadi, K.S. and Kinra, V.K. (2005). Particle impact damping: effect of mass ratio, material, and shape. *Journal of Sound and Vibration*, vol. 283, pp. 433–448. (Cited on pages 4 and 14.)

Matchett, A.J., Yanagida, T., Okudaira, Y. and Kobayashi, S. (2000). Vibrating powder beds: a comparison of experimental and Distinct Element Method simulated data. *Powder Technology*, vol. 107, no. 1-2, pp. 13–30. (Cited on page 22.)

McNamara, S. and Falcon, E. (2005). Simulations of vibrated granular medium with impact-velocity-dependent restitution coefficient. *Physical Review E*, vol. 71, pp. 031302/1–031302/6. (Cited on page 20.)

Medved, M., Dawson, D., Jaeger, H.M. and Nagel, S.R. (1999). Convection in horizontally vibrated granular material. *Chaos*, vol. 9, no. 3, pp. 691–696. (Cited on page 13.)

Meirovitch, L. (2001). *Fundamentals of Vibrations*. McGraw-Hill, New York. (Cited on page 104.)

Metcalfe, G., Tennakoon, S.G.K., Kondic, L., Schaeffer, D.G. and Behringer, R.P. (2002). Granular friction, Coulomb failure, and the fluid-solid transition for horizontally shaken granular materials. *Physical Review E*, vol. 65, no. 3, pp. 031302/1 – 031302/15. (Cited on page 13.)

Mindlin, R.D. (1949). Compliance of elastic bodies in contact. *ASME Journal of Applied Mechanics*, vol. 16, p. 259. (Cited on page 20.)

Mindlin, R.D. and Deresiewicz, H. (1953). Elastic spheres in contact under varying oblique forces. *ASME Journal of Applied Mechanics*, vol. 20, p. 327. (Cited on pages 20 and 50.)

Moré, J.J., Garbow, B.S. and Hillstrom, K.E. (1980). User guide for MINPACK-1. Tech. Rep. ANL-80-74, Argonne National Laboratory, Argonne, Ill. (Cited on page 107.)

Mouraille, O., Mulder, W.A. and Luding, S. (2006). Sound wave acceleration in granular materials. *Journal of Statistical Mechanics: Theory and Experiment*, vol. P07023, p. 15. (Cited on page 11.)

Munjiza, A. and Andrews, K.R.F. (1998). NBS contact detection algorithm for bodies of similar size. *International Journal for Numerical Methods in Engineering*, vol. 43, no. 1, pp. 131–149. (Cited on page 19.)

Mustoe, G.G.W. and Miyata, M. (2001). Material flow analyses of noncircular-shaped granular media using discrete element methods. *Journal of Engineering Mechanics*, vol. 127, no. 10, pp. 1017–1026. (Cited on page 19.)

Nayfeh, S.A., Verdirame, J.M. and Varanasi, K.K. (2002 Mar). Damping of flexural vibration by coupling to low-density granular materials. In: Agnes, G.S. (ed.), *Proceedings of SPIE Conference on Smart Structures and Materials: Passive Damping and Isolation*, vol. 4697, pp. 158–167. San Diego, CA, USA. (Cited on page 5.)

Nowak, E.R., Knight, J.B., Ben-Naim, E., Jaeger, H.M. and Nagel, S.R. (1998). Density fluctuations in vibrated granular materials. *Physical Review E*, vol. 57, no. 2, pp. 1971–1982. (Cited on page 11.)

Olson, S.E., Drake, M.L., Flint, E.M. and Fowler, B.L. (1999 Feb 9–11). Development of analytical methods for particle damping. In: *Proceedings of the 4th National Turbine Engine High Cycle Fatigue Conference*. Monterey, CA. (Cited on page 14.)

O'Sullivan, C. and Bray, J.D. (2004). Selecting a suitable time step for discrete element simulations that use the central difference time integration scheme. *Engineering Computations: Int J for Computer-Aided Engineering*, vol. 21, no. 2–4, pp. 278–303. (Cited on page 22.)

Painter, B. and Behringer, R.P. (2000). Dynamics of two-particle granular collisions on a surface. *Physical Review E*, vol. 62, no. 2, pp. 2380–2387. (Cited on page 21.)

Panossian, H.V. (1991). Nonobstructive particle damping (NOPD) performance under compaction forces. In: *Machinery Dynamics and Element Vibrations*, ASME DE-Vol. 36, pp. 17–20. (Cited on pages 5 and 15.)

Panossian, H.V. (1992). Structural damping enhancement via non-obstructive particle damping technique. *ASME Journal of Vibration and Acoustics*, vol. 114, pp. 101–105. (Cited on page 4.)

Panossian, H.V. (2002 Feb). Non-obstructive particle damping experience and capabilities. In: *Proceedings of the 20th International Modal Analysis Conference (IMAC XX)*, vol. 4753, pp. 936–941. SPIE, Los Angeles. (Cited on page 4.)

Papalou, A. and Masri, S.F. (1996). Response of impact dampers with granular materials under random excitation. *Earthquake Engineering & Structural Dynamics*, vol. 25, pp. 253–267. (Cited on page 13.)

Papalou, A. and Masri, S.F. (1998). An experimental investigation of particle dampers under harmonic excitation. *Journal of Vibration and Control*, vol. 4, pp. 361–379. (Cited on pages 3, 5, and 13.)

Pendleton, S.C., Basile, J.P., Guerra, J.E., Tran, B., Ogomori, H. and Lee, S.H. (2008 Apr 7–10). Particle damping for launch vibration mitigation: Design and test validation. In: *Proceedings of the 49th AIAA/ASME/ASCE/AHS/ASC Structures, Structural Dynamics, and Materials Conference*, AIAA-2008-2027. Schaumburg, IL. (Cited on page 3.)

Perkins, E. and Williams, J.R. (2001). A fast contact detection algorithm insensitive to object sizes. *Engineering Computations*, vol. 18, no. 1/2, pp. 48–61. (Cited on page 19.)

PFC3D (2003). PFC3D 3.0: User's Guide, Itasca Consulting Group. (Cited on pages 45 and 47.)

Pöschel, T., Schwager, T. and Brilliantov, N.V. (1999). Rolling friction of a hard cylinder on a viscous plane. *The European Physical Journal E*, vol. 10, pp. 169–174. (Cited on page 21.)

Pöschel, T., Schwager, T. and Salueña, C. (2000). Onset of fluidization in vertically shaken granular material. *Physical Review E*, vol. 62, no. 1, pp. 1361–1367. (Cited on page 12.)

Ramachandran, S. and Lesieutre, G. (2008). Dynamics and performance of a harmonically excited vertical impact damper. *ASME Journal of Vibration and Acoustics*, vol. 130, no. 2, pp. 021008/1–021008/11. (Cited on page 3.)

Renard, S., Schwager, T., Pöschel, T. and Salueña, C. (2001). Vertically shaken column of spheres. Onset of fluidization. *The European Physical Journal E*, vol. 4, no. 2, pp. 233–239. (Cited on page 12.)

Ristow, G.H. (1997). Phase diagram and scaling of granular materials under horizontal vibrations. *Physical Review Letters*, vol. 79, no. 5, pp. 833–836. (Cited on page 12.)

Rongong, J.A. and Tomlinson, G.R. (2005 Apr 18–21). Amplitude dependent behaviour in the application of particle dampers to vibrating structures. In: *Proceedings of the 46th AIAA/ASME/ASCE/AHS/ASC Structures, Structural Dynamics, and Materials Conference*, AIAA-2005-2327. Austin, Texas. (Cited on page 15.)

Rougier, E., Munjiza, A. and John, N.W.M. (2004). Numerical comparison of some explicit time integration schemes used in DEM, FEM/DEM and molecular dynamics. *International Journal for Numerical Methods in Engineering*, vol. 61, pp. 856–879. (Cited on page 22.)

SABS M33a:1992 (1992). *The International Metric System (SI). Guide to the use of the SI in South Africa*. SABS, Pretoria, South Africa. (Cited on page xii.)

Saeki, M. (2001 Nov 11–16). Impact damping with granular materials. In: *Proceedings of IMECE2001: Adaptive Structures and Material Systems Symposium*. New York, USA. (Cited on page 14.)

Saeki, M. (2002). Impact damping with granular materials in a horizontally vibrating system. *Journal of Sound and Vibration*, vol. 251, no. 1, pp. 153–161. (Cited on page 22.)

Salueña, C., Esipov, S.E., Pöschel, T. and Simonian, S. (1998). Dissipative properties of granular ensembles. In: *Proceedings of The SPIE's Conference on Smart Structures and Materials, Passive Damping and Isolation*, vol. 3327, pp. 19–26. (Cited on page 22.)

Schäfer, J., Dippel, S. and Wolf, D.E. (1996). Force schemes in simulations of granular materials. *Journal de Physique I*, vol. 6, no. 5, pp. 5–20. (Cited on pages 20 and 50.)

Simonian, S.S. (1995 May). Particle beam dampers. In: Johnson, C.D. (ed.), *Proceedings of SPIE Conference on Smart Structures and Materials: Passive Damping*, vol. 2445, pp. 149–160. (Cited on page 4.)

Simonian, S.S. (2004 Apr 19–22). Particle damping applications. In: *Proceedings of the 45th AIAA/ASME/ASCE/AHS/ASC Structures, Structural Dynamics & Materials Conference*, AIAA 2004-1906. Palm Springs, California. (Cited on page 5.)

Slavič, J., Simonovski, I. and Boltžar, M. (2003). Damping identification using a continuous wavelet transform: application to real data. *Journal of Sound and Vibration*, vol. 262, pp. 291–307. (Cited on page 17.)

Stevens, A.B. and Hrenya, C.M. (2005). Comparison of soft-sphere models to measurements of collision properties during normal impacts. *Powder Technology*, vol. 154, pp. 99–109. (Cited on pages 20 and 50.)

Tan, X., Modafe, A. and Ghodssi, R. (2006). Measurement and modeling of dynamic rolling friction in linear microball bearings. *Journal of Dynamic Systems, Measurement and Control*, vol. 128, pp. 891–898. (Cited on page 21.)

Tennakoon, S.G.K. and Behringer, R.P. (1998). Vertical and horizontal vibration of granular materials: Coulomb friction and a novel switching state. *Physical Review Letters*, vol. 81, no. 4, pp. 794–797. (Cited on page 13.)

Tennakoon, S.G.K., Kondic, L. and Behringer, R.P. (1999). Onset of flow in a horizontally vibrated granular bed: Convection by horizontal shearing. *Europhysics Letters*, vol. 45, no. 4, pp. 470–475. (Cited on page 12.)

Thompson, A. and Taylor, B.N. (2008). *Guide for the Use of the International System of Units (SI)*. NIST Special Publication 811, National Institute of Standards and Technology, Gaithersburg, MD. (Cited on page xii.)

Tokoro, C., Okaya, K. and Sadaki, J. (2005). A fast algorithm for the discrete element method by contact force prediction. *Kona*, vol. 23, pp. 182–193. (Cited on page 22.)

Tomlinson, D.R., Pritchard, D. and Wareing, R. (2001). Damping characteristics of particle dampers – some preliminary results. *Proc Instn Mech Engrs Part C: J Mechanical Engineering Science*, vol. 215, pp. 253–257. (Cited on page 2.)

Velichkovich, A.S. and Velichkovich, S.V. (2001). Vibration-impact damper for controlling the dynamic drillstring conditions. *Chemical and Petroleum Engineering*, vol. 37, no. 3–4, pp. 213–215. (Cited on page 5.)

Vu-Quoc, L. and Zhang, X. (1999*a*). An accurate and efficient tangential force-displacement model for elastic frictional contact in particle-flow simulations. *Mechanics of Materials*, vol. 31, pp. 235–269. Erratum (1999): vol. 31, pp. 761–762. (Cited on page 20.)

Vu-Quoc, L. and Zhang, X. (1999*b*). An elastoplastic contact force-displacement model in the normal direction: displacement-driven version. *Proceedings of the Royal Society A*, vol. 455, pp. 4013–4044. (Cited on page 20.)

Vu-Quoc, L. and Zhang, X. (1999*c*). Erratum to: An accurate and efficient tangential force-displacement model for elastic frictional contact in particle-flow simulations (Mechanics of Materials, vol. 31, 1999, pp. 235–269). *Mechanics of Materials*, vol. 31, pp. 761–762. (Cited on page 20.)

Vu-Quoc, L., Zhang, X. and Walton, O.R. (2000). A 3-D discrete-element method for dry granular flows of ellipsoidal particles. *Computer Methods in Applied Mechanics and Engineering*, vol. 187, pp. 483–528. (Cited on page 19.)

Walton, O.R. and Braun, R.L. (1986). Viscosity, granular-temperature, and stress calculations for shearing assemblies of inelastic, frictions discs. *Journal of Reology*, vol. 30, no. 5, pp. 949–980. (Cited on page 20.)

Wassgren, C.R., Brennen, C.E. and Hunt, M.L. (1996). Vertical vibration of a deep bed of granular material in a container. *ASME Journal of Applied Mechanics*, vol. 63, pp. 712–719. (Cited on page 11.)

Wassgren, Jr, C.R. (1997). *Vibration of Granular Materials*. PhD, California Insitute of Technology, Pasadena, California. (Cited on page 11.)

Williams, J.R. and O'Connor, R. (1995). A linear complexity intersection algorithm for discrete element simulation of arbitrary geometries. *Engineering Computations*, vol. 12, no. 2. (Cited on page 19.)

Williams, J.R. and Pentland, A. (1992). Super-quadrics and modal dynamics for discrete elements in interactive design. *Engineering Computations*, vol. 9, no. 2, pp. 115–127. (Cited on page 19.)

Witt, B.L. and Kinra, V.K. (2006 May 1–4). Particle impact damping in the horizontal plane. In: *47th AIAA/ASME/ASCE/AHS/ASC Structures, Structural Dynamics, and Materials Conference*, AIAA 2006-2209, pp. 7345–7352. Newport, Rhode Island. (Cited on page 15.)

Wong, C.X., Daniel, M.C. and Rongong, J.A. (2007 Apr 23 –26). Prediction of the amplitude dependent behaviour of particle dampers. In: *Proceedings of the 48th AIAA/ASME/ASCE/AHS/ASC Structures, Structural Dynamics, and Materials Conference*, AIAA 2007-2043. Honolulu, Hawaii. (Cited on pages 16 and 17.)

Wong, C.X., Daniel, M.C. and Rongong, J.A. (2009). Energy dissipation prediction of particle dampers. *Journal of Sound and Vibration*, vol. 319, no. 1-2, pp. 91–118. (Cited on pages 18 and 54.)

Yang, M.Y. (2003). *Development of Master Design Curves for Particle Impact Dampers*. PhD, The Pennsylvania State University. Dampers. (Cited on pages 14 and 18.)

Yang, X. and Candela, D. (2000). Potential energy in a three-dimensional vibrated granular medium measured by NMR imaging. *Physical Review Letters*, vol. 85, pp. 298–301. (Cited on page 11.)

Yung, K.L. and Xu, Y. (2003). Non-linear expressions for rolling friction of a soft ball on a hard plane. *Nonlinear Dynamics*, vol. 33, pp. 33–41. (Cited on page 21.)

Zhang, N. and Rosato, A.D. (2006). Experiments and simulations on vibration induced densification of bulk solids. *Kona*, vol. 24, pp. 93–103. (Cited on pages 11 and 22.)

Zhou, Y.C., Wright, B.D., Yang, R.Y., Xu, B.H. and Yu, A.B. (1999). Rolling friction in the dynamic simulation of sandpile formation. *Physica A*, vol. 269, pp. 536–553. (Cited on page 21.)

Zhou, Y.C., Xu, B.H., Yu, A.B. and Zulli, P. (2002). An experimental and numerical study of the angle of repose of coarse spheres. *Powder Technology*, vol. 125, pp. 45–54. (Cited on page 21.)